University of Stavanger

FACULTY OF SCIENCE AND TECHNOLOGY

MASTER'S THESIS

Study programme/specialization : Engineering Structures and Materials with Specialization in Mechanical Engineering	Spring semester, 2021. Open/Confidential
Author : Shusil Bista	 **(Signature of author)**
Faculty Supervisor: Prof. Vidar Folke Hansen **External Supervisor:** Mette Lokna Nedreberg (Kongsberg Maritime R&T Propulsion)	
Title of master's thesis : Mechanical and microstructural analysis of 3D-Printed 316L stainless steel	
Credits (ECTS) : 30	
Keywords : Additive manufacturing, Powder bed laser fusion, Selective laser melting, Computer aided design, 316L Stainless Steel.	Number of pages: 81 + supplemental material/other: Stavanger, 15/06/2021 dd/mm/year

ABSTRACT

The project aims to analyze the mechanical properties and microstructure study of 316L stainless steel, which is as-printed using the selective laser melting (SLM) technique. Metal components produced by the SLM process offer superior mechanical properties to those of bulk materials. Selection of the appropriate process parameters, building direction, and building height plays an essential role in determining the microstructure and properties of the final product. For this reason, mechanical properties, microstructure, hardness, and porosity of 316L specimens are investigated according to their building directions. Recommended standard methods followed for the sample preparation and experimental procedures. Light optical microscope (LOM) and scanning electron microscope (SEM) are used to study microstructure and porosity. Variation in the microstructure within the Sample; Cellular and columnar dendritic structures were found depending on the solidification rate. The mechanical properties varied concerning the building direction and significantly affected by the build angle orientation. The tensile and impact test all specimens failed by ductile fracture predominantly. However, few locations were brittle in nature, suspected to be caused by delamination. Additionally, hardness values varied in parallel- and normal to build directions and differ in building height. Furthermore, the investigation has also revealed defects such as entrapped gas during metallic powder manufacturing, which has predominantly created spherical pores and inter-track porosity during the SLM process, which was irregular in shape minority. The experimental analysis discovered that the standard process parameter used in sample manufacturing produced the fully dense parts. And, presented results demonstrate a correlation between the build direction, building height, and the resulting mechanical properties of SLM 316L specimens.

ACKNOWLEDGMENTS

I want to express my gratitude to Professor Vidar Folke Hansen, who has been my faculty supervisor during this thesis. He has significantly contributed with knowledge and encouragement during the completing work. Appreciation is also to my external supervisor, chief engineer Mette Lokna Nedreberg (Kongsberg Maritime R&T Propulsion), to make this work possible and supply the material. Moreover, a genuine acknowledgment is given to Wakshum Mekonnen Tucho for his preliminary instructions and advice on the use of electron microscope, sample preparation. Thanks to lab engineers who guided me on using machines in the workshop to remove the extra metal. Lastly, appreciation is to the University of Stavanger for allowing me to use the lab at my favorable time.

LIST OF FIGURES

LIST OF TABLES

ABBREVIATIONS

AM: Additive Manufacturing

BCC: Boyd Centered Cubic

BSD: Electron Backscattered Diffraction

BSE: Backscattered Electron

CAD: Computer-Aided Design

CNC: Computerized Numerical Control.

DLD: Direct Laser Deposition

EBM: Electron Beam Melting

EBSD: Electron Backscattered Diffraction

FCC: Face-Centered Cubic

LOM: Light Optical Microscope

LPBF: Laser Powder Bed Fusion

PBF: Powder Bed Fusion

SE: Secondary Electron

SEM: Scanning Electron Microscope

SLM: Selective Laser Melting

SLS: Selective Laser Sintering

UTS: Ultimate Tensile Strength

WD: Working Distance

Table of Contents

CHAPTER 1: INTRODUCTION

Technology is growing faster every day; people are always seeking to have a new and unique product in their hands with the latest technology. The product with good performance and luxurious design with low cost only can survive due to high competition. That is why companies are investing considerable budgets in research and development in various sectors. Every product is produced with good design, high performance, low cost, and should be on time. Therefore, a company needs to launch a new product in the market with a greater frequency and, consequently, the demand for new projects and the development of new products grows. For any product, the material is one major factor that changes the appearance, design, performance of a product. That is why for the last few decades, companies are looking for advanced technology to provide the above requirements. One among them, 3D printing, plays a vital role, which is also known as additive manufacturing (AM)[1]. A complete product can be manufactured within a few minutes or an hour using an Additive manufacturing process with minimum human work. AM technology produces components or products by rapid melting and solidifying the selected areas in deposited thin layers of raw material. This process can be said the reverse process of the traditional manufacturing method; it is due to the three-dimensional object is produced by adding successive thin layers, one on top of the other, until the formation of the desired product [1, 2].

Today AM is the one most important technology in the development phase of the new product. Which has Its various benefits [1], such as: consumes less time in the product development phase, minimizes the costs, it has a higher possibility of performing several tests, development of prototypes for study purpose, complex design is feasible to produced and decrease in project delivery time. Though AM technology was to produce only prototypes in preliminary days, over a few decades, their application is deployed to fabricate complex designs of functional and structural parts for service in different sectors such as aerospace, automobile, medicine, and art and fashion. In addition, components or parts can be built on demand, reducing spare parts inventory and quickly transferring to the market to replace damaged and old elements.

In this thesis, we will focus on the selective laser melting process specifically. The SLM is one of the laser powder bed fusion (LPBF) techniques. It uses a high-energy laser beam to melt a powder bed selectively. For SLM metals, the raw material should be within the sort of

fine powder. The powder is generated from an ingot using gas atomization or plasma atomization techniques. The fine powder is lying on a substrate employing a roller or scraper to start the SLM process. Then a beam melts the specified 2D cross-section of the primary layer (selective melting), supported by the sliced CAD file, leading to melting and fusing these areas. The substrate moves downward by the height of each deposit, and this process continues until the part is manufactured entirely. Laser power, scanning speed, hatch spacing, and powder bed layer thickness are some of the most critical parameters involved in the SLM process. Several parts can be built together so that the build chamber can be fully utilized [3, 4].

They are using the most diverse raw materials; different metals and alloys are used to produce complex shapes using the SLM technique [5]; among them is austenitic AISI 316L stainless steel. 316L stainless steel is durable and resistant to chemical contaminants and acidic solutions such as bromides, sulfuric acid, and chlorides. Carbon content lower than 0.03 wt% confers good weldability to the material and makes the AISI 316L an optimal grade for SLM [6].

For the mechanical and microstructure analysis, the stainless steel 316L is printed by Aidro Hydraulics and 3D printing using the SLM process. Different experiments are conducted, such as mechanical properties, Hardness evaluation, Impact Energy, and microstructure study. The procedure for preparing the Sample and analysis is according to the recommended standards, which are presented in later chapters.

CHAPTER 2: LITERATURE STUDY

2.1 Additive Manufacturing

Due to the complex structures and design required, the traditional manufacturing technology takes a long time, most material wastage, and expensive. In the early 1980s, Additive manufacturing was considered only for the manufacturing of prototypes. But, over the previous couple of decades, Additive manufacturing (AM) technology has experienced a significant increase in attention from the industry and researchers worldwide. Resulting in an exciting evolution from initially enabling only poor prototyping to now producing fully functional parts for everything from medical [7] to the aerospace, automotive industry, oil, and gas industry [8]. Today there exist several varieties of AM, as shown in figure 1, which may be a novel method of producing parts directly from a digital model using a layer-by-layer material buildup approach. This new manufacturing method can manufacture fully dense metallic parts in a short duration of time with high precision.

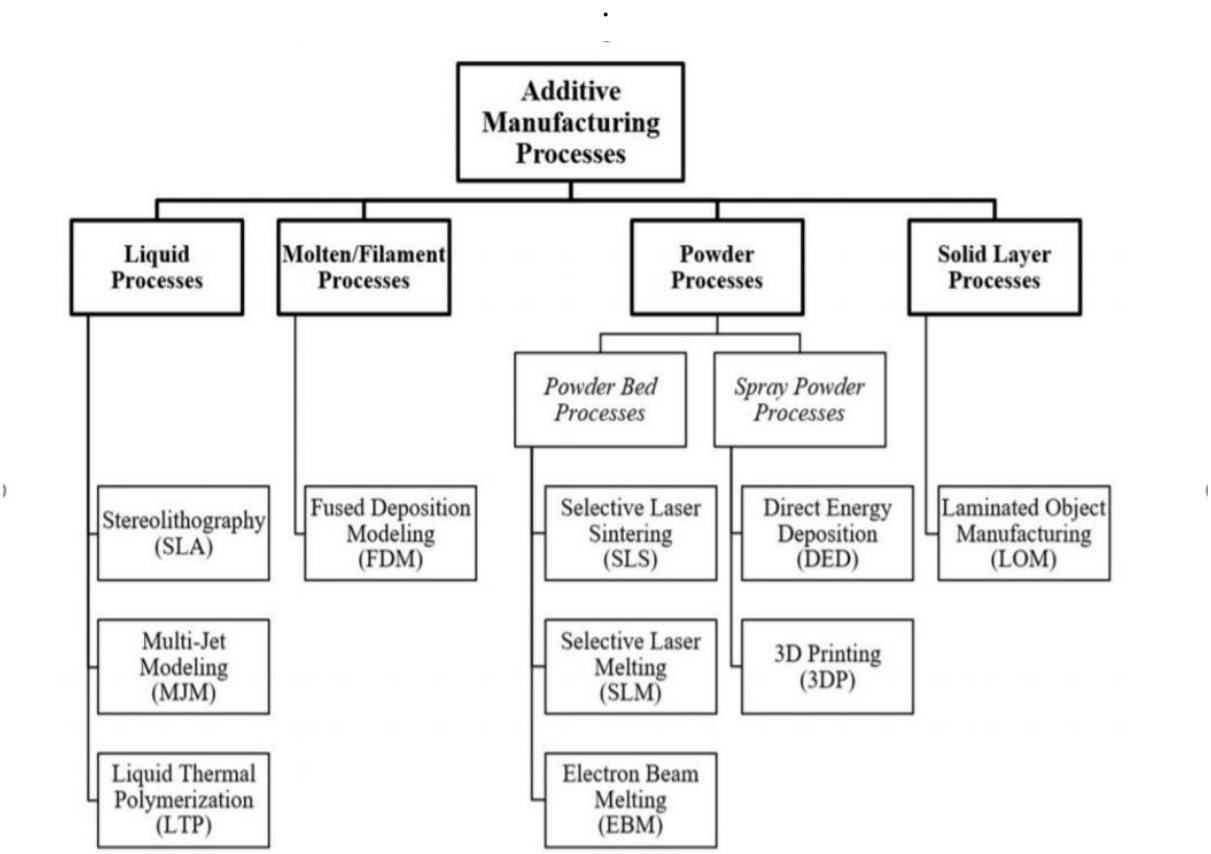

Figure 1: Various additive manufacturing processes techniques [10]

According to ASTM International [9], Additive Manufacturing (AM) is defined as joining materials to form objects from 3D model data, usually layer upon layer, as opposed to subtractive manufacturing methodologies. Compared to traditional manufacturing, additive manufacturing with SLM is advantageous in applied technology and is competitive in economics. In addition, SLM allows for designing components with specifically refined microstructures to achieve desired properties that are impossible with conventional manufacturing [10].

2.1.1 Powder Bed Fusion

The powder bed fusion (PBF) process has been grown widely within a few years due to its low cost and high product quality; that's why PBF is the commonest interest of researchers. In the powder bed fusion process, there's no or minimum support is required because the powder acts as a support structure. The powder bed fusion process can be used for different materials, including plastics, glass, metals, and alloys. The powder used in the process can be recycled to produce more parts. A cross-sectional schematic view of the layer-by-layer powder bed fusion (PBF) is represented in figure 2. In PBF, a heat source is required to fuse the powder to manufacture a 3D (three-dimensional) product. [11]. There are different heat sources available for the PBF process are, thermal, electron, or laser. The Powder bed fusion technique includes selective laser melting (SLM), selective laser sintering (SLS), and electron beam melting (EBM) technology. [12,13].

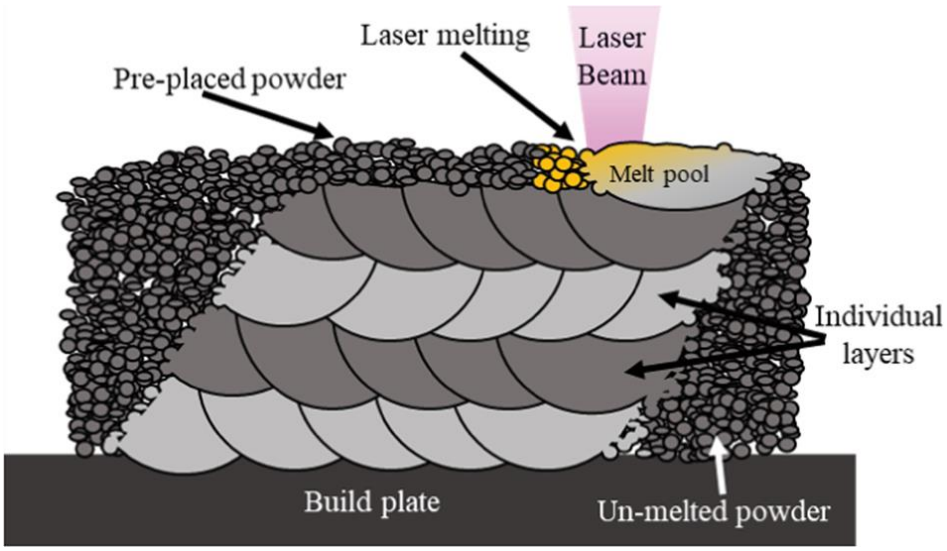

Figure 2: layer-by-layer powder bed fusion (PBF) process [14]

The PBF process involves melting metallic powder in selected areas from a powder bed using laser or beam energy, where the melt pool is then consolidated by rapid solidification. The SLM process can provide a gas-protective building environment, where the building chamber is with argon to avoid oxidation and contamination. Similarly, the EBM process operates under an enclosure, which can prevent oxidation and enhance beam quality. But the upper beam energy in EBM would cause a bigger melt pool, therefore, a rougher surface of the produced component [15]. Federal Aviation Administration has certified some AM-produced components for aerospace, like the housing of inlet temperature sensor for GE commercial aviation turbine engine, SLM-produced GE LEAP (General Electric Leading Edge Aviation Propulsion) engine (Co-Cr) fuel nozzle, SLM-built bracket[16].

2.1.2 Selective Laser Melting Process

Selective laser melting (SLM) is a 3D printing technique with a specific process to manufacture structural and functional components from metal and alloy metal powders to get desired mechanical and physical properties. Near net-shape parts with a density of up to 99.9% relative density can be printed using a high power-density laser. SLM is a layer-by-layer process, and fine powder is spread and melted locally to build a product. The powder is distributed and spread evenly with a coater arm to create a level, uniform surface that completely covers the build area. A focused laser beam is then precisely directed at the powder layer, scans over the part's cross-section, and fuses the powder. After the fusion of a layer build platform is lowered by thickness, the process is repeated until the complete part has been printed [17, 18].

The schematic representation of the selective laser melting process is shown in Figure 3. The process begins with a 3D model from computer-aided design software. Then the 3D model is optimized and mathematically sliced into many 2D thin layers using AM specialized software (Figure. 3(a)). The data of the 2D sliced model are transferred into the control computer of SLM, which may assign scanning parameters that are defined already and scanning strategies. Before the printing starts, the building chamber must be pressurized with inert gas (argon or nitrogen) to prevent contamination and oxidation during manufacturing. After completing a scan of one layer, the retractable building platform would lower by a particular distance adequate to the predefined layer thickness, followed by a replacement powder layer pavement. The exact process repeats until the whole component or part is printed (Fig. 3(b)). The unmelted powder is often collected and sieved for future use. The scanning and

processing parameters (Fig. 3(c)) play an essential role in the melting and solidification after the fusion of powder material.

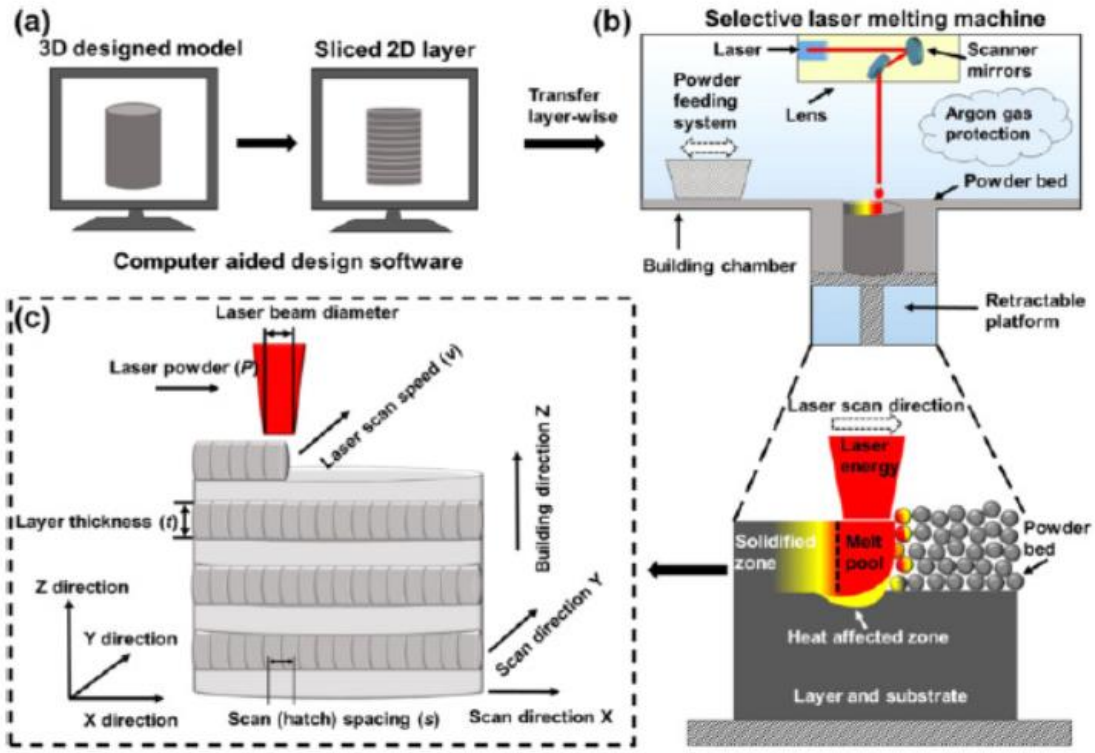

Figure 3: Schematic representation of the selective melting process [19]

SLM technique melts metal powder layers selectively, ensures a complete melting along the scan track, and allows fusion between channels and consecutive layers, leading to a far better mechanical performance and highly dense part [20].

2.1.3 Powder Morphology

Metallic powder raw material plays a vital role in the SLM process for the resulting product. In the SLM process, metal powder is used as the initial material. Mainly two methods are applied to manufacture metallic powder gas atomization and water atomization. Both gas and water atomized powder [21] are represented in Figure 4. It was found that particles from gas atomization are more uniform in size and shape than those atomized by water.

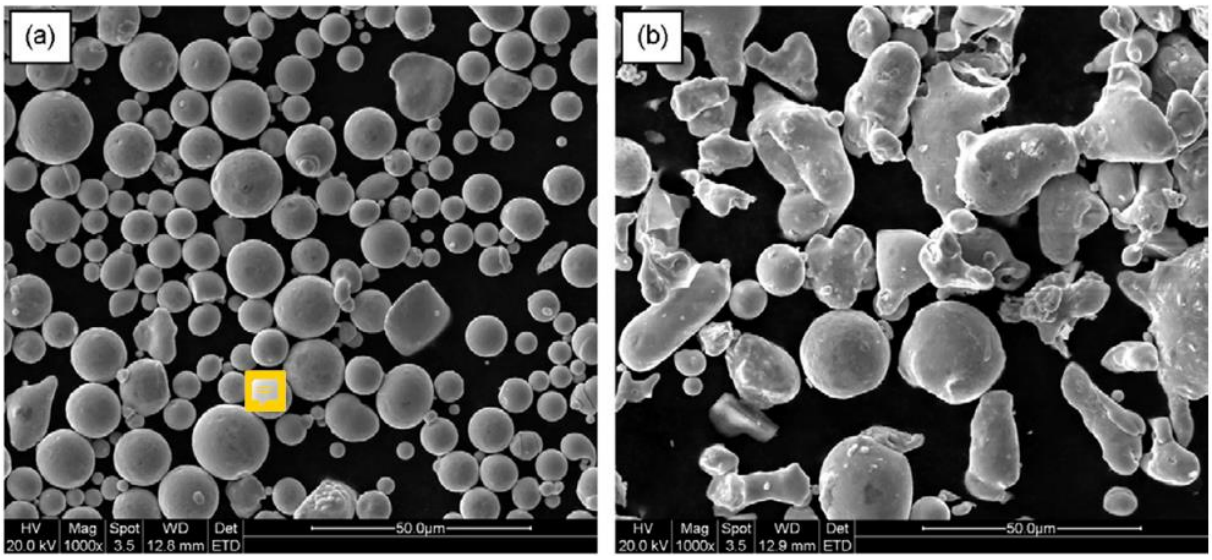

Figure 4: SEM images of Powder Morphologies (a) gas atomized powder (b) water atomized powder[21].

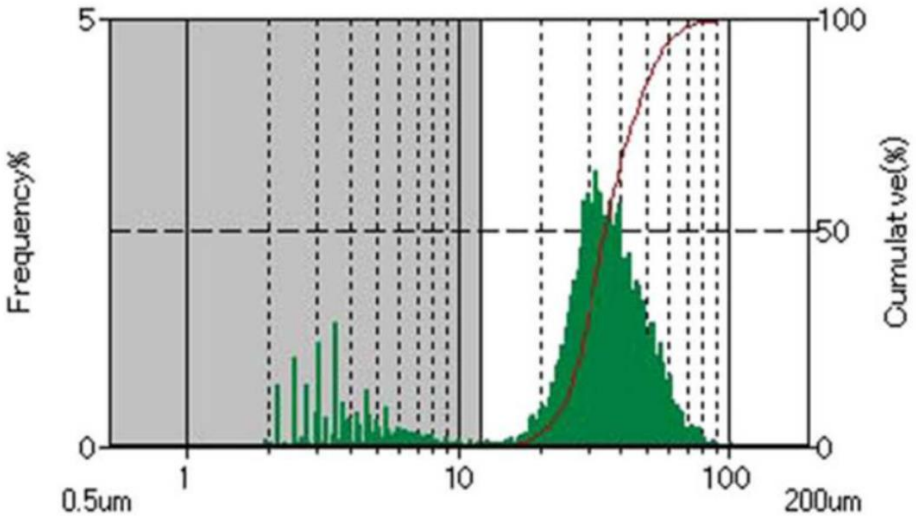

Figure 5: Powder Measurement, Distribution based diameter of 316L [22]

Kamath performed a powder morphology study for the material used in their research, which happened to incorporate 316L Powder from LPW [22]. Their characterization is illustrated in Figure 5. The distributions are centered about 30-40μm and 50μm when measuring distribution by diameter and volume, respectively. This discrepancy would suggest that the powder isn't uniformly spherical.

2.1.4 Process parameters

The number of various lasers and scan parameters is often specified, the foremost common being laser power, scan speed, and scan spacing (or hatch distance). The swift laser-powder interaction creates a melt pool with heat and sophisticated hydrodynamic flows [19]. The melt pools' thermal and physical behavior might be balanced by optimizing manufacturing parameters and scan strategies[23]. The processing parameters play an essential role in the melting and solidification process of powder in the SLM process. Improper melting and solidification would primarily affect the geometry and microstructural features of the built parts. Therefore, it's key to accumulate a stable melt pool in the SLM process to reinforce layer bonding and improve the density of produced components. Practically, the energy density may be a well-known simplified guide index obtained from the predefined scanning parameters to direct to get highly dense parts [24]. The quantity laser energy density (Ev, J mm−3) is often computed using Equation 1.

$$E = \frac{\mathrm{P}}{\mathrm{v}*\mathrm{t}*\mathrm{s}} \quad \text{equation 1}$$

Where P is the laser power in watt (W), t is the layer thickness (mm), v is the laser scan speed (mm s−1), and s is that the hatching space (mm). Thus, the laser power, powder layer thickness, hatching space, and scan speed are often manipulated during the SLM process. According to Eq. (1), a high scan speed and low laser power will lower energy density, which would result in insufficient melting of powder and high porosity. In contrast, excessive energy density (i.e., high laser power and low scan speed) can induce pore defects [23].

2.1.5 Influence of Process Parameters

The quality of the 316L produced using AM technology depends upon the process parameters. Different processing parameters such as; spot size, focus, layer thickness, hatch distance, and laser power must be optimized to get a better product. They result in thermal histories by affecting the incident energy and the shape and size of the melt pools [25,26]. Thermal gradients and high cooling rates are affected by high local power and scan rates, resulting in complex and strong hydrodynamic fluid flows. These phenomena play a vital role in crystal growth, orientation, material spattering, and microstructural defect (e.g., pores and inclusions) [27]. Flaws, pores, and microstructural result from the process parameters during production and play an essential role in mechanical and functional behavior. Mechanical properties depend on the microstructure of materials, which largely depends on the thermal history experienced during processing.

In SLM of stainless steel 316L, some studies showed that point distance, exposure time, scan speed, layer thickness, and building direction strongly influence the parts' quality. These parameters should be controlled during the fabrication process to get a good surface finish and mechanical properties [28-30]. The investigation found that the process parameters significantly influence the quality of products using AM technology.

2.1.6 SLM Materials

Today the metal parts are under thorough investigation as the technique of SLM manufacturing generates specific macro- and microstructures, defects, and phrases that are different from conventional manufacturing of the same materials. Most of the SLM research revolves around three types of metals: Iron, titanium, and nickel. SLM powders can be divided into two categories, single material powders, and alloyed powders. Single material powders consist of strictly one type of metal, such as pure titanium. In this case, tests show an almost 100%part density; however, high thermal stresses can cause cracks [31]. Alloyed powders contain alloyed materials like Ti-6Al-4V and steel powders. The mechanical properties of these materials are comparable to bulk material apart from ductility, which is significantly reduced [32].

Stainless steel 316L is the most used material in powder-based AM processes. The powder grain size affects the density and the produced part's mechanical properties [33, 34]. In SLM of stainless steel 316L, some studies showed that point distance, exposure time, scan speed, layer thickness, and building direction strongly influence the parts' quality. These parameters should be controlled during the fabrication process to get a good surface finish and mechanical properties [28-30].

2.2 Stainless Steel

Stainless steel is recyclable and can be used in a wide range of applications. Ordinary citizens interact with products made from stainless steel day-to-day. Different types of steel are present globally, such as Carbon Steel, Alloy Steels, Stainless steel, and Tool Steels based on carbon content level and various alloying elements. Stainless steels generally consist of chromium from10 to 18 percent as the primary alloying element and are appreciated for high corrosion resistance. With over 11% chromium, steel is almost 200 times additional resistant to corrosion than mild steel. The specialty of this sort of steel is that it's not entirely stain-proof in low-oxygen, high-salinity, or poor air-circulation environments.

Stainless steel is widely used as a structural material in chemical, petrochemical, and power engineering and, increasingly often, in-vehicle and aviation industries shipbuilding industry. This is due to the material's good resistance to high-temperature creep and corrosion. Broad applications of austenitic steel for the construction of equipment working in conditions of elevated temperatures and aggressive corrosion environments require methods for evaluating the mechanical properties of welded joints, which frequently determine the structure's service life.

2.2.1 316 and 316L

Type 316 and 316L are Austenitic stainless steel; both type 316 and 316L exhibit better corrosion resistance and are more potent at elevated temperatures. 316L is almost like 316 in nearly every way. Both are durable, corrosion-resistant, and a natural choice for high-stress situations. 316L stainless steel contains more molybdenum than 316 stainless steel, and 316L stainless steel is an extra-low carbon version of the 316-steel alloy. The lower carbon content reduces harmful carbide precipitation as a result of welding. It is highly durable and resistant to chemical contaminants and acidic solutions such as bromides, sulfuric acid, and chlorides. Properties of molybdenum and nickel help prevent pitting and crevice corrosion.

2.2.2 Chemical composition of 316L

Stainless steel is used in different environments because its properties can be changed by adding various alloying elements in different percentages. Cr, Ni, Mo, Cu, Si, Ni, N, Nb, C, Ti, Al, S, and Mn, are some of the alloying elements used. The alloys are usually added to stabilize the microstructure, improve strength or corrosion properties. The alloying elements' content level is shown in Table 1, and how they affect properties is discussed briefly in a later chapter.

Element	**Cr**	**Mn**	**C**	**S**	**Ni**	**N**	**P**	**Si**	**Mo**	**Fe**
%weight min	16.5	-	-	-	10	-	-	-	2	balance
%weight max	18.5	2	0.03	0.02	13	0.11	0.045	0.75	2.5	balance

Table 1: Chemical composition of 316L Stainless Steel

2.2.3 Microstructure

Microstructure determines the properties of a material how it reacts to the subjected load on it in a different environment. Families of stainless-steel alloys with different properties may be obtained by the addition of various alloying elements to the different content levels. Each element offers different attributes with respect to strength and ability to resist corrosive environments. The family of stainless steel is classified based on metallurgical microstructure, which are austenitic stainless steels, ferritic stainless steels, martensitic stainless steels, duplex stainless steels, precipitation hardening stainless steels, and Mn-N substituted austenitic stainless steels [35].

Austenitic stainless have a face-centered cubic lattice structure. They are the most common type of stainless steel used because they are formable, weldable, and have very high corrosion resistance, making them suitable for a wide-ranging application from high temperature to cryogenic temperature.

The main alloying elements of stainless steels are Cr and Ni. The Cr is added to improve corrosion resistance, although it stabilizes the ferrite phase (ferrite stabilizers). The Ni is added to improve ductility and toughness as well as to stabilize the austenite phase. Thus Ni is also known as an austenite stabilizer. Other elements such as Mo, Cu, Si, N, Nb, C, Ti, Al, S,

and Mn can also be added. These elements can be classified as an austenite or ferrite stabilizer depending on the effect on the crystallographic structure [36]. Generally, austenite stabilizers have an FCC phase structure and are more soluble in the austenite phase. Therefore they restrict the formation of the ferrite phase because they are thermodynamically more stable in the austenite phase. Similarly, Ferrite stabilizers have a body-centered cubic structure; therefore, they are more soluble in the ferrite phase and restrict the formation of the austenite phase because this reduces the free energy. Therefore the crystal structure of stainless steels depends on the composition of alloying elements that are added.

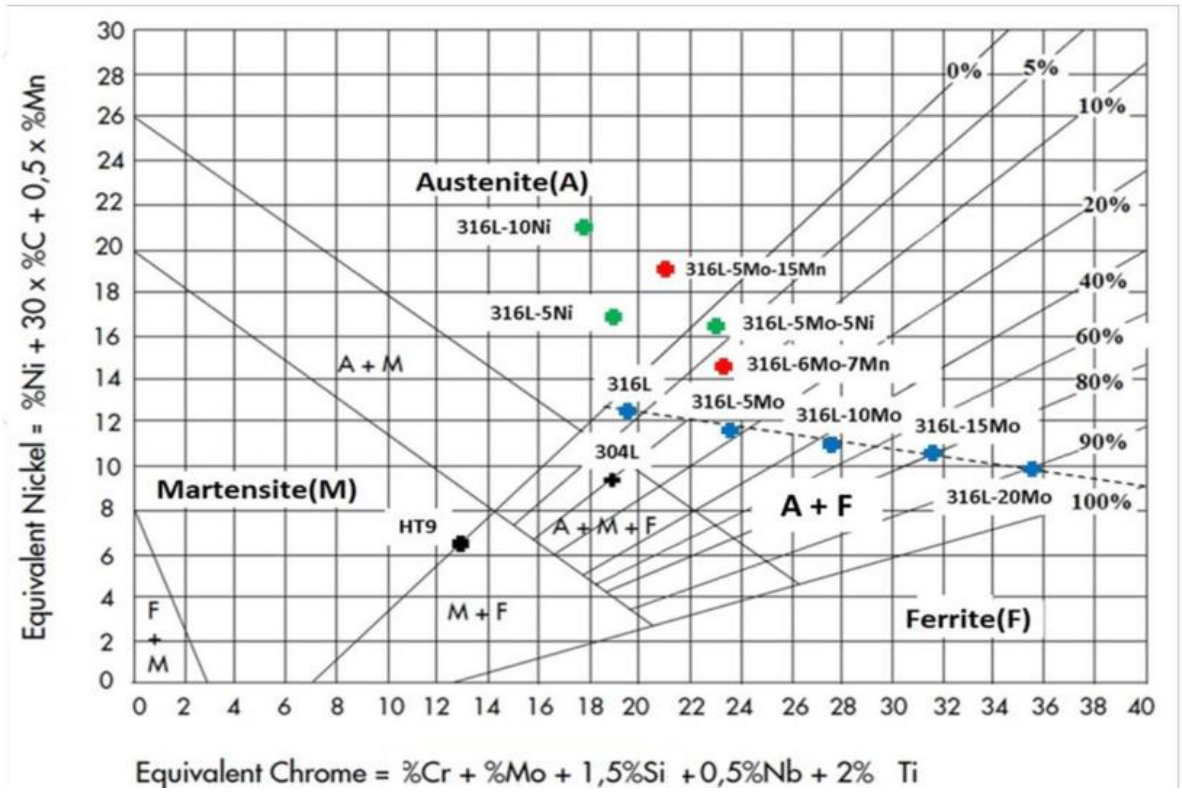

Figure 6: Schaeffler-Delong constitutional diagram [37]

Schaeffler-Delong constitutional diagram with the locations of the 316L SS alloys made with different Mo, Ni, and Mn additions based on their Ni and Cr equivalent values[37] is shown in figure 6. The constitution diagram is used to predict the levels of ferrite present in stainless steel depending on the alloying elements used. One diagram that is used to do this is the Schaeffler and Delong diagram (Figure 6), which was designed to show phases present in the solidified conditions of welds and castings after cooling from a high temperature. The diagram makes it possible to calculate the total ferrite and austenite in the cast based on the stabilizing effect of alloying elements by determining the chromium equivalent and nickel equivalent. The nickel equivalent is an empirically derived formula that takes into account all

of the stabilizing effects of all ferrite alloying elements, and the chromium equivalent is an empirically determined formula that takes into account the stabilizing effect of all ferrite forming elements [33, 35].

2.2.4 Equilibrium Diagram

2.2.4.1 Iron carbon Equilibrium diagram

The diagram describes the suitable conditions for two or more phases to exist in equilibrium, for example. The iron-carbon chart gives information about the microstructural evolution before, during, and after the solidification of an iron-carbon alloy. The diagram's basic features can understand the behavior of the 316L stainless steel after the SLM process during solidification.

Phases in Fe–Fe3C Phase Diagram: We can see the different phases at different temperatures at carbon composition.

α-ferrite - solid solution of C in body-centered cubic (BCC) Fe

- Transforms to FCC g-austenite at 912 °C
- γ-austenite - Solid solution of C in FCC Fe
- Changes to BCC δ-ferrite at 1395 °C
- It is not stable below the eutectic temperature (727 ° C) unless cooled rapidly.

δ-ferrite- solid solution of C in BCC Fe

- It is stable only at a temperature >1394 °C. It melts at 1538 °C ¾ Fe3C (iron carbide or cementite)
- This intermetallic compound is metastable at room T. It decomposes (very slowly, within several years) into α-Fe and C (graphite) at 650 - 700 °C

In the diagram, we can see several critical points at which different reactions occur.

Three main Reactions;

Peritectic reaction, L + δ = γ at T=1493oC and 0.18wt%C At 1493°C

The solution undergoes another transformation to δ-ferrite + austenite before an amount of the austenite transforms to ferrite

Eutectic reaction, L = γ + Fe3C at T=1147oC and 4.3wt%C

Eutectoid reaction, γ = α + Fe3C at T=727oC and 0.77wt%C

Eutectoid reaction occurs at a temperature of 723°C is the upper limit of the ferrite-cementite phase field

Carbon is an interstitial impurity in iron that forms a solid solution with α, γ, δ phases of Maximum iron solubility in BCC α-ferrite is 0.022 wt% at 727 °C. BCC: relatively small interstitial positions Maximum solubility in face-centered cubic (FCC) austenite is 2.14 wt% at 1147 °C - FCC has more significant interstitial. Mechanical properties: Cementite (Fe3C) is hard and brittle: strengthens steel. The mix between ferrite and cementite and microstructure determines the mechanical properties. Magnetic properties: α -ferrite is magnetic below 768 °C, austenite is non-magnetic called Curie point [37].

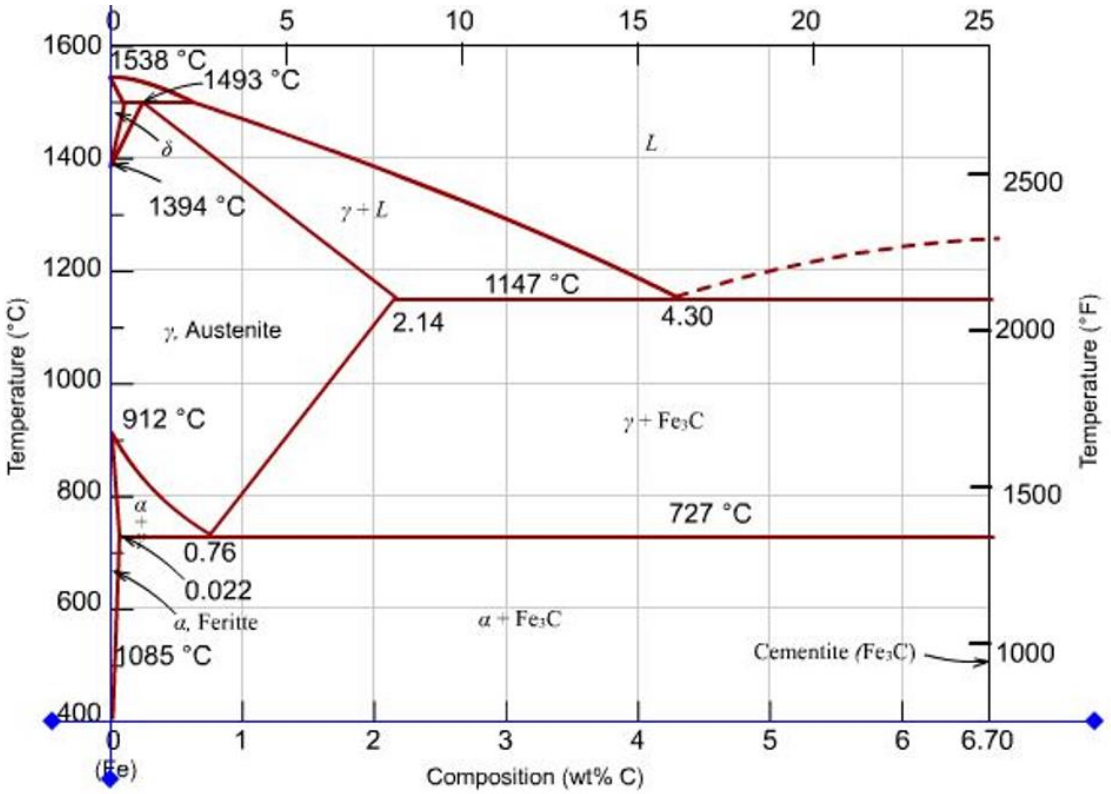

Figure 7: Iron carbon equilibrium diagram

2.2.4.2 Iron Chromium Equiblrium Diagram

The iron-chromium equilibrium diagram is given in Figure 8, with a solid red line indicating the chromium content in 316L. The figure shows how a chromium content over 13wt% provides a microstructure containing the only ferrite over the whole temperature range. The ferrite here is the previously described δ-ferrite since the chromium allows the phase to continue from occurring and down to room temperature. Stainless steels are alloys containing

a minimum of 12-13 wt % Cr and more than 50% Fe content with low carbon content levels. The minimum Cr content must make the alloys resistant to corrosion under conditions that regular steel undergoes decay. This is because at 12-13 wt% Cr content and above, stainless steels form an adherent self-healing chromium oxide layer on the surface that stabilizes the corrosion rate to a constant value [38].

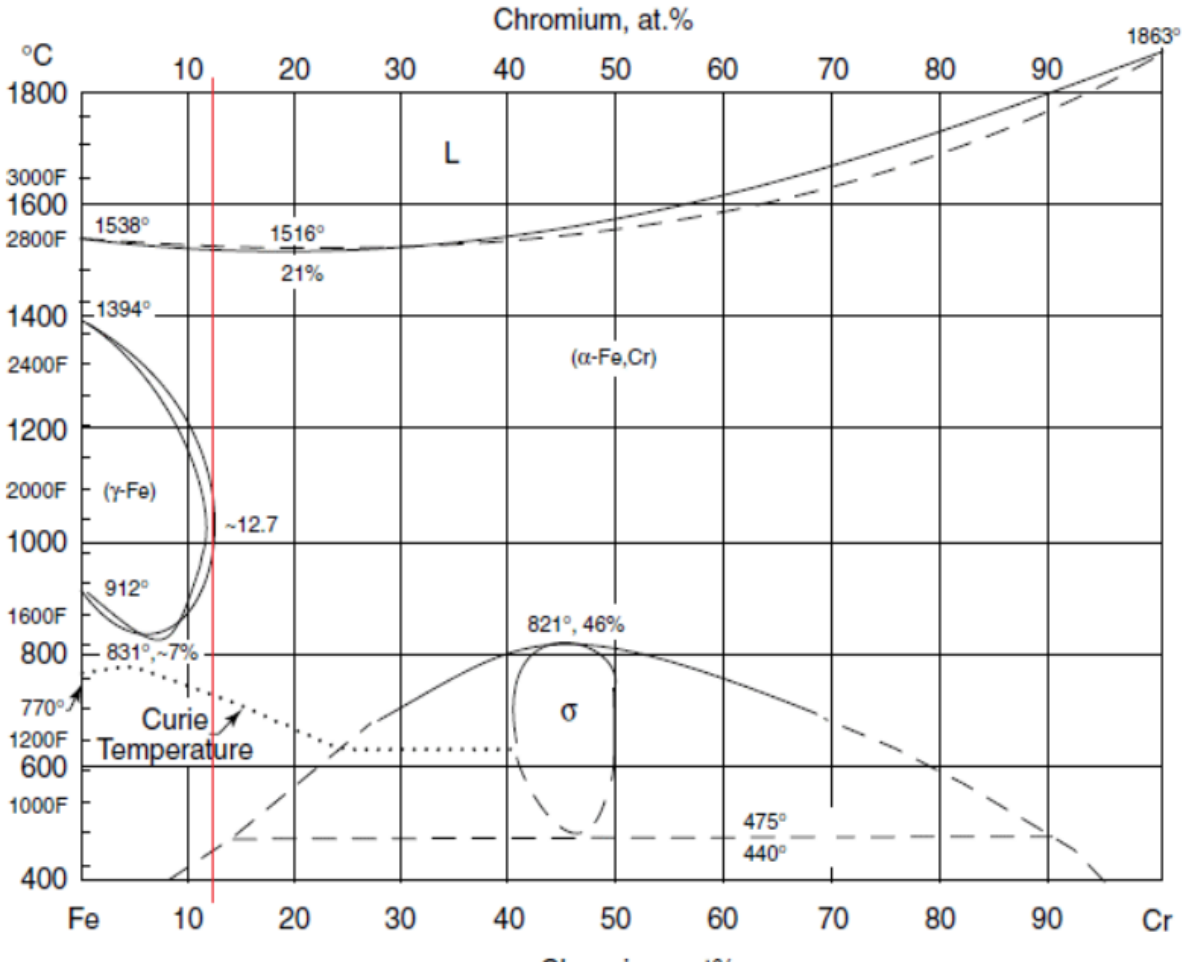

Fig 8: Iron-Chromium equilibrium Diagram[35]

The binary Fe-Cr equilibrium diagram is shown in Figure 9. As shown in the diagram, three crystal structures may be formed on solidification, depending on the temperature and composition. The phases formed are austenite (γ), ferrite (α /δ) and sigma (σ). Austenite has a face-centered cubic crystal structure. Both α and δ phases have a BCC and are typically referred to as alpha ferrite and delta ferrite, respectively. The σ phase is an intermetallic Fe-Cr compound with a tetragonal crystal structure. As can be seen on the Fe-Cr equilibrium diagram, σ precipitation starts at temperatures close to 820 o C, and the precipitation range

expands with decreasing temperature [33]. The Fe-Cr equilibrium diagram shows that the Cr restricts the γ loop to a composition around 12 wt % Cr and promotes the formation of the α loop due to Cr has a BCC crystal structure; therefore, it favors the formation of α-ferrite. A continuous matrix of the ferrite phase can be formed from the solidification temperature up to room temperature at high Cr content. There is also a narrow temperature range between 12 and 13 Cr wt% over which the α and γ phases co-exist [33]. Both the γ and γ+α loops can be expanded by adding austenite stabilizers such as Mo, Ni, C, and N.

2.2.5 Influence of alloying Elements

Chromium (Cr): Chromium is an essential alloying element for stainless steel with 12-13 wt % content. Increasing Cr content improves the corrosion resistance and stabilizes the ferrite phase in steel.

Nickel (Ni): Nickel gives stainless steel strength, ductility, and toughness at high and low temperatures. It also improves the corrosion resistance of stainless steel in acidic environments.

Carbon (c): Carbon improves mechanical strength and hardness by substitutional and interstitial replacement of iron elements in a lattice structure. In some cases, carbon content is an undesirable element in stainless steel because it has a high thermodynamic longing to Cr. Carbon causes the formation of chromium carbides at grain boundaries when a supersaturation state in austenite is reached, and diffusion is fast enough for the segregation of Cr and C to occur [39]. If the chromium is depleted below 12-13 wt%, the depleted zone becomes susceptible to corrosion. Furthermore, in Ni-containing alloys, Cr retards the γ to α martensite phase transformation, making it easier to retain austenite. Therefore, the Cr depleted zone becomes susceptible to martensitic phase transformation when chromium carbides are formed.

Molybdenum (Mo): Molybdenum also increases the toughness, hardenability, and tensile strength of stainless steel. It increases the hardenability by lowering the required quench rate during the heat-treating process to make solid and hard steel[33]. Molybdenum improves resistance to chloride-induced corrosion like pitting. It also stabilizes the ferrite microstructure and improves mechanical strength.

Copper (Cu): An austenite stabilizer that improves the corrosion resistance of stainless steel in certain acids. It is added in some grades of steel to reduce hardening work which improves machinability[33].

Nitrogen (N): is an austenite stabilizer that increases mechanical strength and corrosion resistance. Typically added as an alternative to carbon to increase the yield strength and reduce chromium carbide formation at grain boundaries [33, 34].

Silicon (Si): enhances the formation of ferrite and is used as a deoxidizer to manufacture steels. It also improves oxidation resistance at high temperatures and in oxidizing solutions at low temperatures. Silicon forms aluminum silicates inclusion in stainless steels [33].

Titanium (Ti): Also improves mechanical properties at high temperatures. Used in austenitic stainless steels with high carbon content to prevent the formation of chromium carbides. [33].

Sulphur (S)and Manganese (Mn): In some grades, S is added to improve the machining behavior of steels. It is also retained in stainless steel because of the inefficiency of melt processing, and it is often considered an undesired element. S has low solubility in steel, and in Mn-containing steel, S mainly exists as manganese sulfide inclusions (MnS). These MnS inclusions are soluble in water and increase the material's susceptibility to pitting and localized corrosion [40]. Manganese is added during steelmaking operation to segregate S in MnS inclusions, which are more thermodynamically stable than FeS inclusions. Ferrous sulfide (FeS) has a low melting point second phase, which forms at grain boundaries and would promote cracking during high-temperature hot-rolling [41]. Pitting can initiate at MnS inclusions because they are unstable in water and dissolve according to Equation 2 to Equation 5 [42]: MnS dissolution results in a change of the oxidation state of S rather than Mn. The Mn maintains the oxidation state, whereas the further reaction of the S can result in its oxidation state changing to different oxidation states (Equation 2 to Equation 5)

$MnS + 4H2O \rightarrow Mn\ 2+ + SO4\ 2- + 8H + 8e$ Equation 2

$MnS + 2H + \rightarrow Mn\ 2+ + H2S$ Equation 3

$H2S \rightarrow S + 2H + + 2e$ Equation 4

$MnS + \rightarrow Mn\ 2+ + S\ 2$ Equation 5

2.2.6 Solidification and the defects

The solidification of selectively melted powder is essential for developing grain structure and any defects or porosity in the manufactured components. Mostly the cellular grains will be seen in 316L processed by SLM process. However, grains can extend over two consecutive layers, which will cause epitaxial growth of the grains [43]. The orientation of grains during solidification is depended on the orientation of the surface of the previously applied layer, which is the energetically favored surface for crystallization [44]. The heat flux affects the direction of grain growth, resulting in grain growth normal to the previously deposited layers, and Isolated grains grow towards the melt pool center during solidification. Then after reaching a certain grain size, grain boundary developed. The development of smaller cells happens Within the individual grains, which are known as subdomains. In microstructure, Local accumulation of heavy elements such as molybdenum promotes the high solidification rate and the associated effects of constitutional undercooling. The element Mo especially accumulates in the residual melt during the solidification of 316L [45].

In addition to that, shell regions possess a high dislocation density [46]. Despite being widely reported, the interaction between solute atoms and dislocation in these areas are discussed controversially[47]. The cell size can also be controlled by the solidification rate, depending on the time-temperature history during printing. On this account, more significant subdomains present at the respective boundary surfaces on the individually applied layer. Due to the application of new layers upon solidified layers, additional heat will be induced into the solidified layers, representing an in situ heat treatment [48]. Furthermore, due to the temporally increased temperature, diffusion of atoms and dislocation movement can occur. Therefore, the temperature-induced due to the melting of subsequent layers plays a considerable role in the microstructure and the mechanical properties of SLM-built materials [47].

Defects such as entrapment, binding defects can be found in the SLM-built specimens. Binding defects can arise due to an insufficient amount of residual melt between two adjacent solidification fronts. Furthermore, an inadequate energy input due to incomplete removal of by-products from the laser-powder interaction zone can be the reason for the lack of fusion defects [49]. The powder bed density is a crucial influence on the specimen density due to void formation [50]. The variations in the powder layer thickness can be seen as a possible reason for the formation of cavities [51].

2.2.7 Porosity in 316L printed by SLM Technique

The pores and voids that can be seen specimens built using the SLM technique. The presence of these spherical and irregular pores arises due to the low solubility of s argon in the steel matrix and rapid solidification [52]. When rapid solidification happens, there will be a short time to escape the gas from the molten pool that creates porosity in the solidified components. The study shows that the porosity increased both in quantity and size by increasing scan speed from 100 mm/s to 300 mm/s [53]. These studies show that imparting too high energy density at low scan speed induces a lower degree of porosity. In contrast, a combination of moderate energy with relatively high scan speed significantly increases porosity formation. The size of hatch spacing is also an important parameter to be tuned to control pore formation. An increased pore formation with increased hatch spacing (0.15e0.8 mm) was reported [53] on SS316L parts. According to this report, the pores formed at 0.8 mm hatch spacing were huge and can critically affect the material's mechanical strength. Smaller hatch spacing ensures overlapped melt pools and, consequently, less pore formation than a larger hatch spacing, leading to weak overlapping and facilitating pore formation conditions [53]. On the other hand, Sander and co-workers [54] showed that porosity decreases with increasing laser power between 165 and 285Wby tuning other parameters. They have claimed as the lowest ever reported porosity for SLM-fabricated SS316L.References:

2.2.8 Mechanical properties

The mechanical properties of austenitic stainless steels are dependent on the alloying elements and degree of cold work. Information concerning the strength, ductility, and stiffness of a material can be gathered from a tensile test.

Yield Strength:

Yield strength gives information about a material that can withstand without permanent deformation. The Yield Strength is defined as is the stress at which a prescribed amount of plastic deformation (commonly 0.2%) is produced. In the stress-strain diagram, the point at which material exceeds the elastic limit and will not regain its original shape or length after releasing stress is the yield point. The yield strength of stainless steel can be determined from chemical composition using the empirical formula equation 6 [39]. It is believed that the value may not be exactly with the tested results.

$YS\ (MPa)$ = 15.4[4.4 + 23(%C) + 32(%N) + 0.24(%Cr) + 0.94(%Mo) + 1.3(%Si) + 1.2(%V) + 0.29(%W) + 2.6(%Nb) + +1.7(%Ti) + 0.82(%Al) + 0.16(%$Ferrite$) + 0.46(d −1 1 2⁄) Equation 6

Where d is the diameter of grain in millimeters, the empirical equation 6 shows that how the alloying elements affect the yield strength of Stainless steel.

Tensile Strength:

One of the essential properties we have to determine is tensile strength for designing parts, components, and structures. The tensile strength is the maximum axial stress that it can take before failure, for example, breaking. We can understand if the material is brittle, ductile, or exhibits both properties at a given temperature from the test result. Sometimes material may behave as ductile at room temperature when testing in a lab, but it can become brittle when exposed to an extremely cold environment. The tensile strength of stainless steel affected by alloying content can be calculated using the empirical equation 7 [39].

$TS\ (MPa)$ = 15.4[29 + 35(%C) + 55(%N) + 2.4(%Si) + 0.11(%Ni) + 1.2(%Mo) + 5.0(%Nb) + 3.0(%Ti) + 1.2(%Al) + 0.14(%$Ferrite$) + 0.82(d −1⁄2) Equation 7.

Where d is the grain diameter in millimeters,

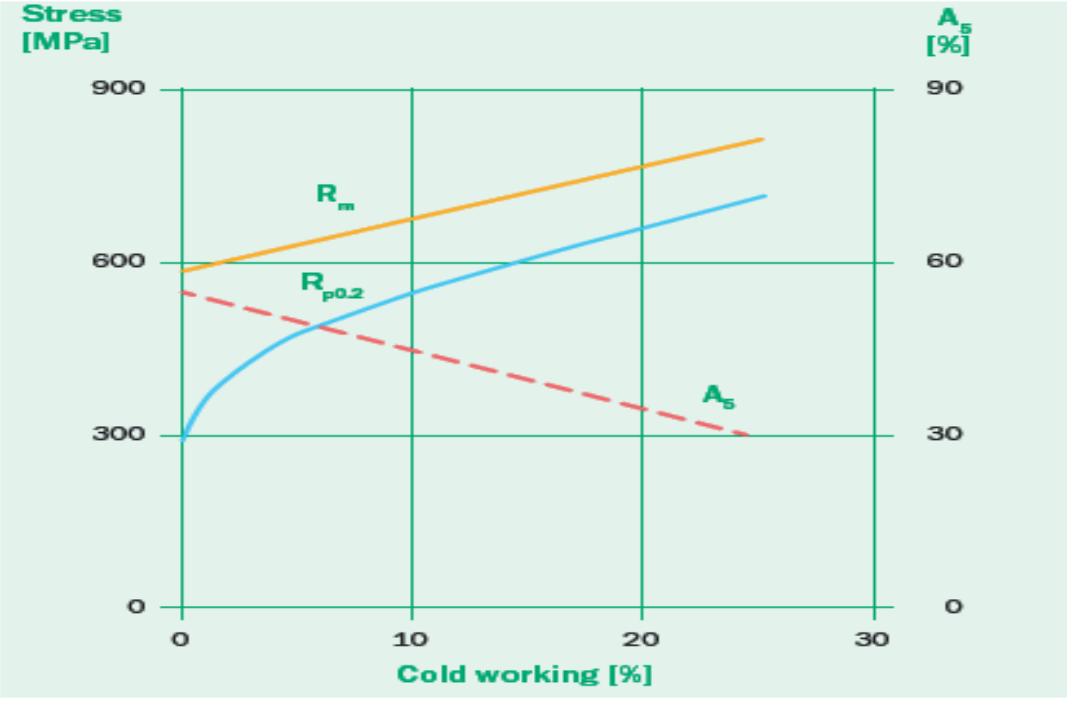

Figure 9. Effect of cold work on the mechanical strength of austenitic stainless steels [34].

Compared with other stainless steels, austenitic stainless steel does not have a very high TS or YS strength (figure 9). Their yield strength can be improved by alloying elements, as illustrated by Figure 9 or cold work. In general, cold work can increase austenitic stainless steel yield strength up to 2000 MPa [39]. This is because, in heavily cold worked steels, some of the austenite transforms into martensite. However, cold work decreases the elongation of austenitic stainless steel (Figure 9). The plastic deformation can begin at about 40 % of the yield strength. Macroscopically at stress below the yield strength, there is theoretically no plastic deformation. However, for those materials that do not display a sharp elastic/plastic transition, the yield strength is usually defined as RP0.2, which means the stress at which there is 0.2% plastic deformation.

Elongation:

The amount of extension of the specimen during tensile testing can be expressed as an absolute number called strain. Strain can be expressed in two different ways: engineering strain and true strain. Engineering strain is the ratio of the change in length to the original length. In contrast, the true strain is based on the instantaneous length of the specimen as the test progresses, the equations for engineering strain as shown in equations 8.

%Elongation = $\frac{\Delta L}{Lo}$*100 equation 8

Where e is engineering strain, Ɛ is true strain, Li is the instantaneous length, and L0 the original length.

Reduction in Area:

Reduction in the Area is comparing the original given cross-sectional area of the Sample before a test and the smallest cross-section area after fracture failure. About the actual cross-sectional area expressed as a percentage. The percentage reduction area of a test sample can be calculated using equation 9.

% Reduction area =$\frac{\Delta A}{Ao}$*100 equation 9.

ΔA= Original cross-sectional area (A_o)-cross-sectional area after fracture(A_f)

2.2.8 Mechanical properties of 316L Influenced by the built-up direction

The mechanical properties such as yield strength and the tensile strength of 316L manufactured using the SLM technique will differ concerning the building direction. The differences are the orientation of the layers, the effect of binding defects, and pressure travel within the components. In vertical buildup specimens, the force is transmitted perpendicularly to the layered structure so that binding defects significantly influence the force transmission. Pores and defects present in the material reduce the specimen's cross-section and develops internal stress concentrations, resulting in premature failure [55]. In contrast, binding defects neither drastically reduce the load-bearing cross-section of the specimen nor does force transmission happen via these structural defects within the case of specimens that have been built up horizontally. Although an equivalent material was processed with different SLM devices, there are large fluctuations within the resulting strength values. The ductility of metal is a function of used laser energy and building direction [56]

CHAPTER 3: SAMPLE MANUFACTURING

3.1 Powder Material

The samples were printed by Aidro and Hydraulics and 3D printing in which raw material 316L powders were fabricated using gas atomization with a particle size distribution of 20–65 µm.

Powder Material composition Element of 316L:

Elements	Cr	Ni	Mo	c	Mn	p	Cu	Si	N	Fe
% Min	17.00	13.00	2.25	-	-	0.025	-	-	-	-
% Max	19.00	15.00	3	0.03	2.000	0.01	0.05	0.07	0.010	Balance

Table 2: Metallic Powder composition for SLM

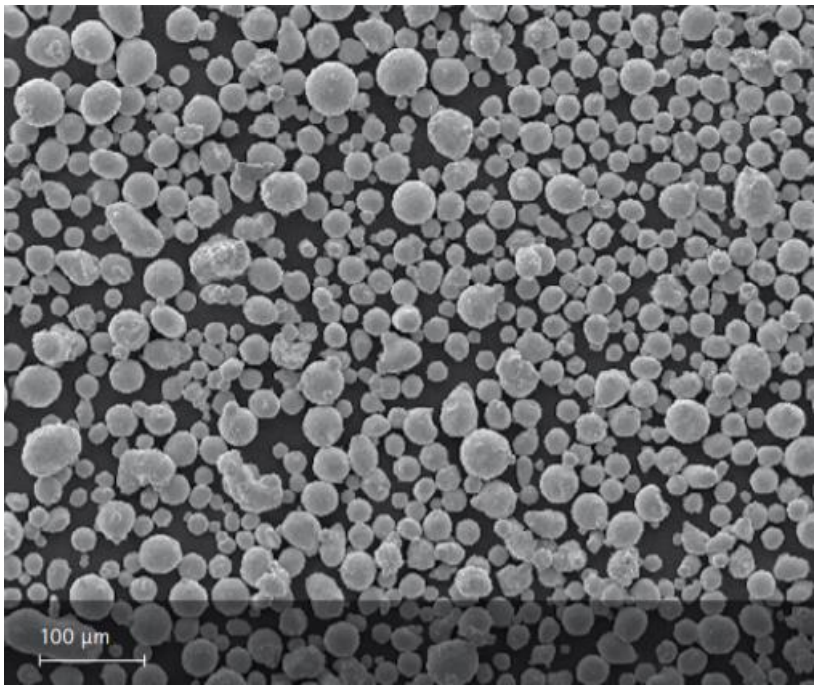

Figure 10: SEM image of 316L powder for SLM

3.2 Manufacturing Of 316L Samples

The samples were manufactured with an EOS M290 machine equipped with a construction chamber with a maximum build height of 325 mm with a 250 mm x 250 mm build area. It is equipped with a Yb-fibre laser with a maximum nominal power of 400 Watt. The minimum wall thickness of 0.1mm, build volume rate of 3.7 mm3 /s. The builds were conducted in an argon environment. Scan speed up to 7.00 m/s. The samples were fabricated with standard EOS M290 for 316L stainless steel for the layer thickness of 40 µm. The specimens used for the investigation are as-built, with No heat treatment in the post-processing. The manufactured Sample is shown in Figures 12 and 13.

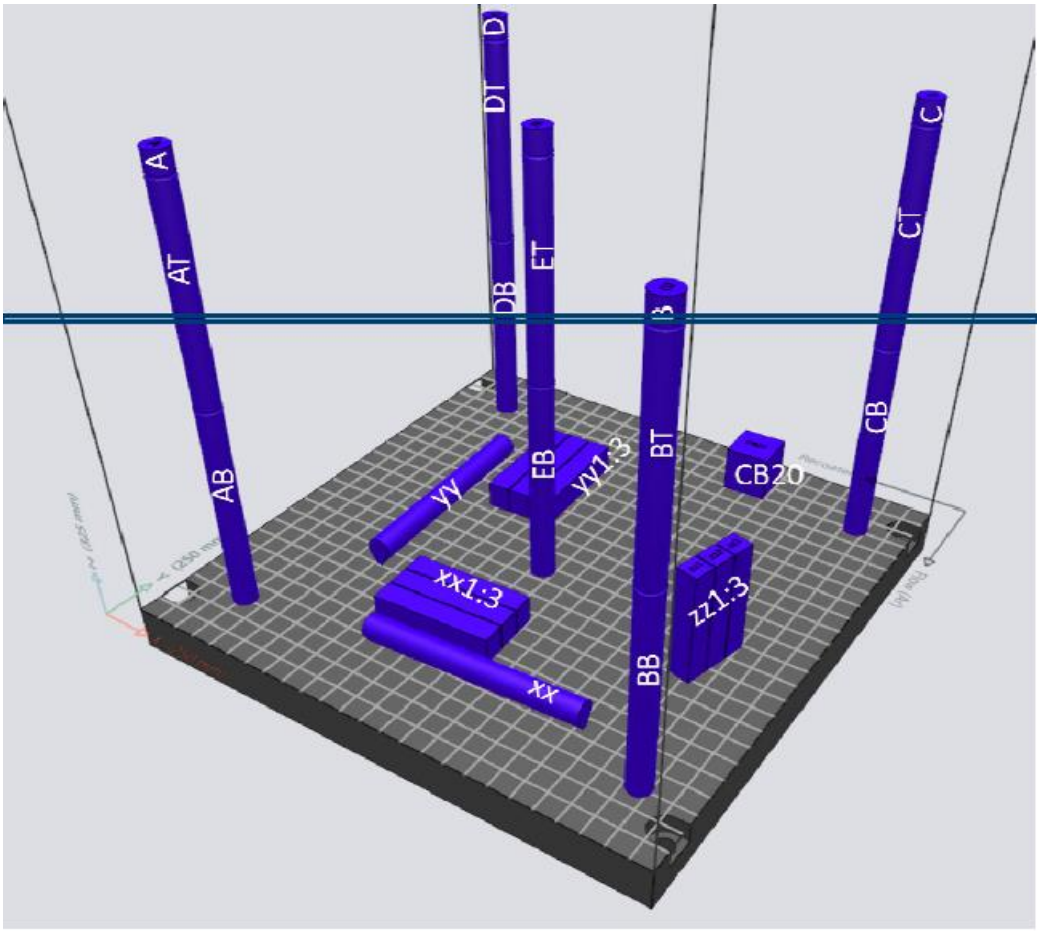

Figure 11: Building platform for different samples

As shown in figure 11, for tensile test horizontally built-in X-direction and Y-direction, and vertically at five positions manufactured. Similarly, for impact energy test was also built in all three directions. One cube named CB20 was made for hardness evaluation and microstructure study. The dimensions details of as printed samples are represented in table 3.

Dimension of samples build:

Samples	**Dimension in mm**
CB20	20*20*20 mm
A, B, C, D, AND E	12mm in diameter and 9-12 mm in length
AB, AT,BB, BT,CB, CT,DB,DT, EB, and ET	Length, 100mm and diameter, 12mm
XX1, XX2, XX3, YY1, YY2, YY3,ZZ1, ZZ2, and ZZ3	56*10*10 mm

Table 3: Dimension details of manufactured samples

Printed samples:

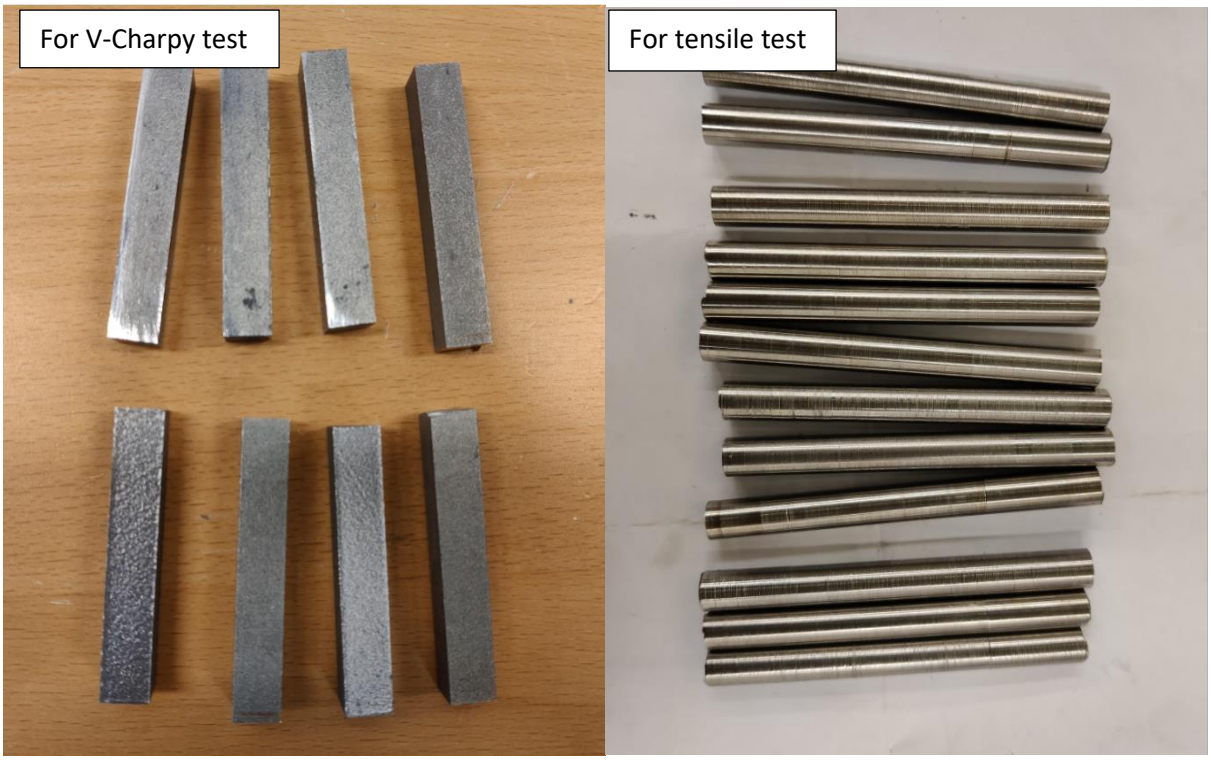

Figure 12: As-printed samples using SLM technique for V-Charpy and tensile test

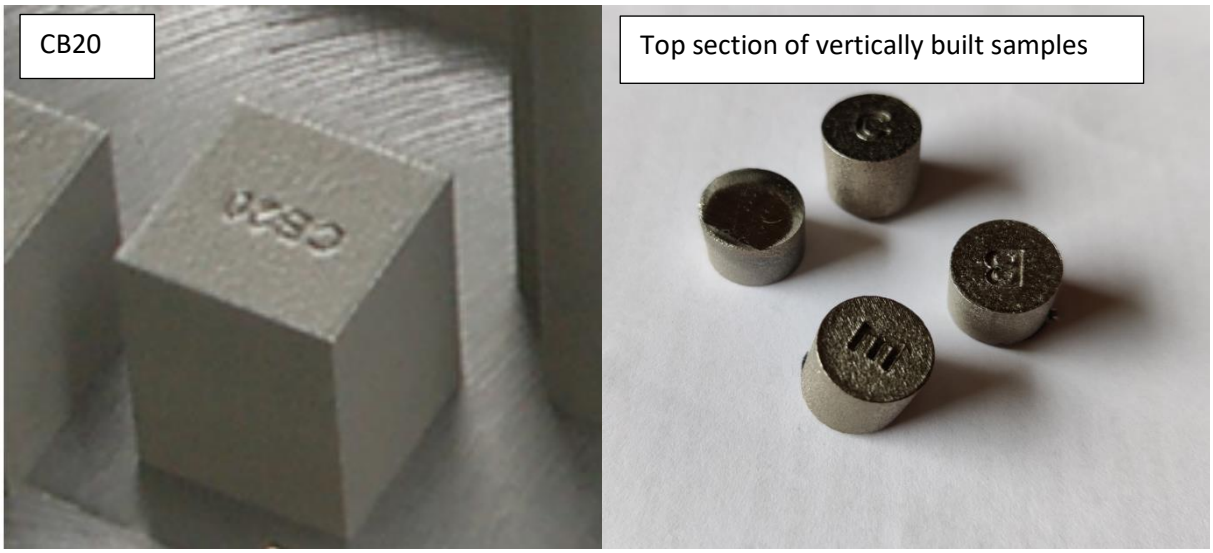

Figure 13: As-printed samples for hardness evaluation and microstructure study

CHAPTER 4: EQUIPMENT USED FOR ANALYSIS

4.1 Light Optical Microscope

An inverted microscope is used for conducting the optical analysis of 316L samples manufactured by the SLM process. Figure 7, shown below, is an inverted microscope by Olympus that observes the mineralogy and metallurgy specimens. An optical microscope has the following two primary functions. It is illuminating a Specimen and Creating a Magnified Image of a Specimen. The feature to create a specimen's magnified image includes obtaining a clear, sharp picture, changing a magnification, and focusing. The function to illuminate a sample has; supplying light, collecting light, and changing light intensity.

The optical illumination system effectively collects light emitted from the light source and leads the light to a specimen to illuminate it. An optical observation system projects a sample through an optical system projects an image to eyes or a pickup device such as Charge-coupled devices (CCD).

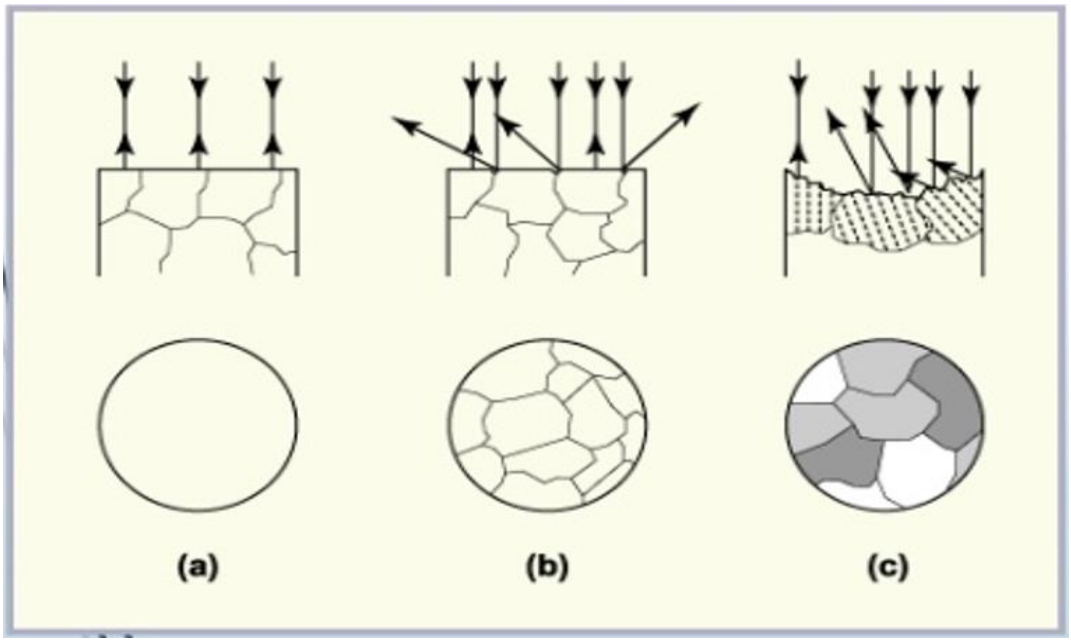

Figure 14: Sample surfaces for LOM; (a) polished (unetched) surface, (b) and (c) etched surface

Figure 14 depicts polished and etched sample surfaces and reflects light and resulting contrast in the micrograph. (a) polished (unetched) surface: from the polished and unetched surface, a clean image can be obtained, but details about the microstructure of a specimen can not be visualized. (b) The grain boundaries are visible when an etched surface with the same grains

with the same orientations is observed. (c) etched surface: when the specimen has grains oriented differently, each grain reacts differently to give varying colors, which means more microstructural details can be gained.

For the material to reflect as much light as possible, the surface must be ground and polished using successively finer abrasives until it reaches finish as much as possible(ASTM E3). Further preparation of Sample with a chemical reagent, an etching procedure that selectively attacks and corrodes material at different rates. The rate of corroding depends on crystallographic orientation, phase, and alloying elements. These areas help to contrast the images due to differences in how much light is reflected, thus revealing the shape and size of grain boundaries, phases, inclusions, segregations, cracks, and pores [57].

Limitations

The optical microscope is easy to use and takes a short time to conduct experimental analysis compare to SEM. On the other hand, it has limitations also; when an optical microscope with transmitted light is employed at very high magnifications, the image will be blur or distorted. There will be fuzzy discs that are surrounded by diffraction rings, referred to as Airy discs. This restricts the magnification and resolving power of the microscope due to the wavelengths of light being 400-700 nm and the numerical aperture of the objective lens [58]. It is broadly lower than the magnification that can be achieved with electron microscopy.

4.2 Scanning Electron Microscope

The scanning electron microscope (SEM) has a wide range of applications for the study of solid materials. SEM uses a beam of focused, high-energy electrons to generate surface signals on solid samples. The highly accelerated electrons have a wavelength of the order of 0.003 nm, enabling magnifying with far better resolution [57] than optical microscopy. The SEM consist of principal components: Source of electrons, electromagnetic lenses, Column through which electrons travel, Sample chamber, Electron detector, computer, and display to view the images. The basic construction of SEM is shown in figure 13.

4.2.1 Basic Working of SEM

When the Electron beam is emitted from the electron gun, accelerated and passed through a number of electromagnetic lenses to produce a focused beam of electrons, then finally strikes

the sample surface that is mounted on a stage. The scan coil situated above the objective lens controls the position of the beam on the sample surface. As the name of the microscope suggests, this beam rastering or scanning enables information about a defined area on the piece to be collected. As a result of the electron-sample interaction, several signals are produced. One or more detectors collect these signals to form images which are then displayed on the computer screen [59].

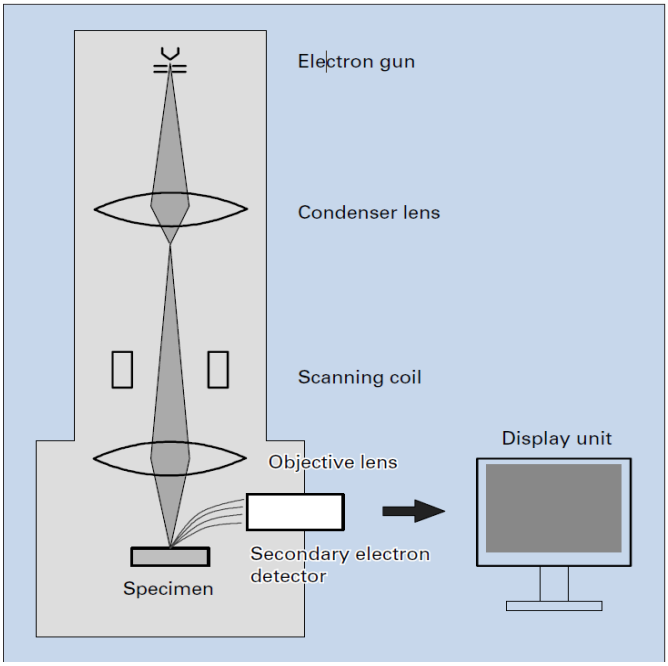

Figure 15: Basic construction of SEM [60]

4.2.2 Electron-Sample Interactions

When the incident accelerated electrons beam interacts with the Sample, it penetrates to a few microns. Depending on the accelerating voltage and the sample density, it generates a variety of signals, Such as; secondary electrons, backscattered electrons, and characteristic X-rays. Figure 1 illustrates the interaction between the electron beam and the Sample. The interaction can be divided into two major categories: elastic interactions and inelastic interactions[61].

Elastic scattering: Elastic scattering happens when incident electrons deflected by the outer shell electrons or by the atomic nucleus of the specimen cause elastic scattering. This interaction is characterized as no energy loss or negligible energy loss during the collision and a wide-angled scattered electron.

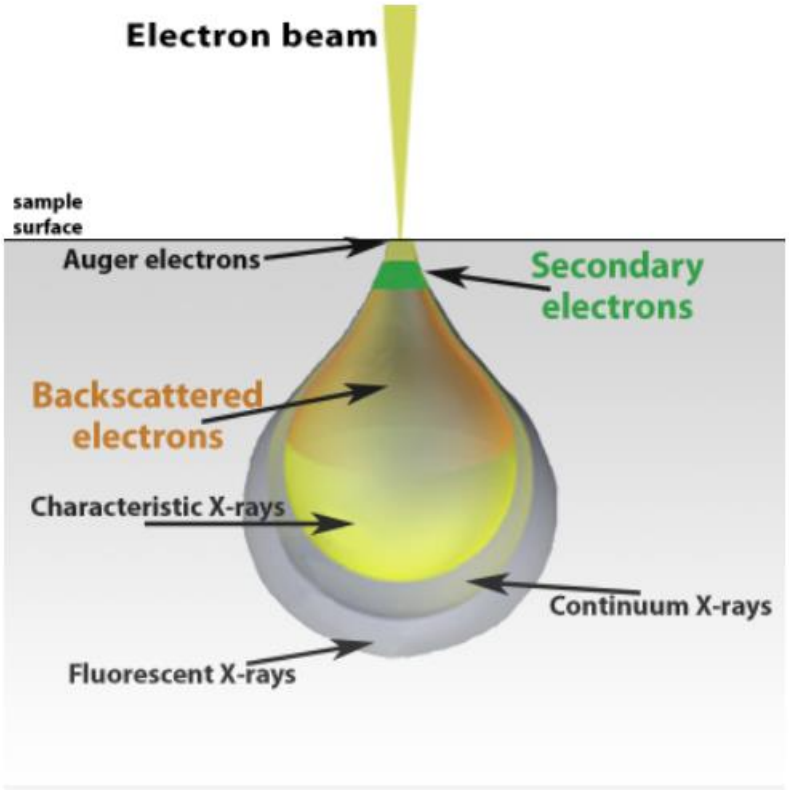

Figure 16: Electron Sample interactions[59]

Inelastic scattering: occurs when an accelerating electron beam hits the Sample's atoms; substantial energy is transferred to the atom, resulting in secondary electrons. SEs are conventionally defined as possessing less than 50 eV energy. Many other signals are produced when an electron beam strikes a sample, including the emission of Auger electrons, characteristic x-rays, and cathodoluminescence. The energy loss depends on the electron's separation energy and whether the specimen electrons are excited collectively or singly.

4.2.3 Types Of Electrons Detected And Information They Provide

In a scanning electron microscope (SEM), two types of electrons are mainly detected: backscattered electrons (BSEs) and secondary electrons (SEs). SE originates from surface regions, whereas BSEs come from deeper areas of the Sample. Thus, they carry different types of information for the material.

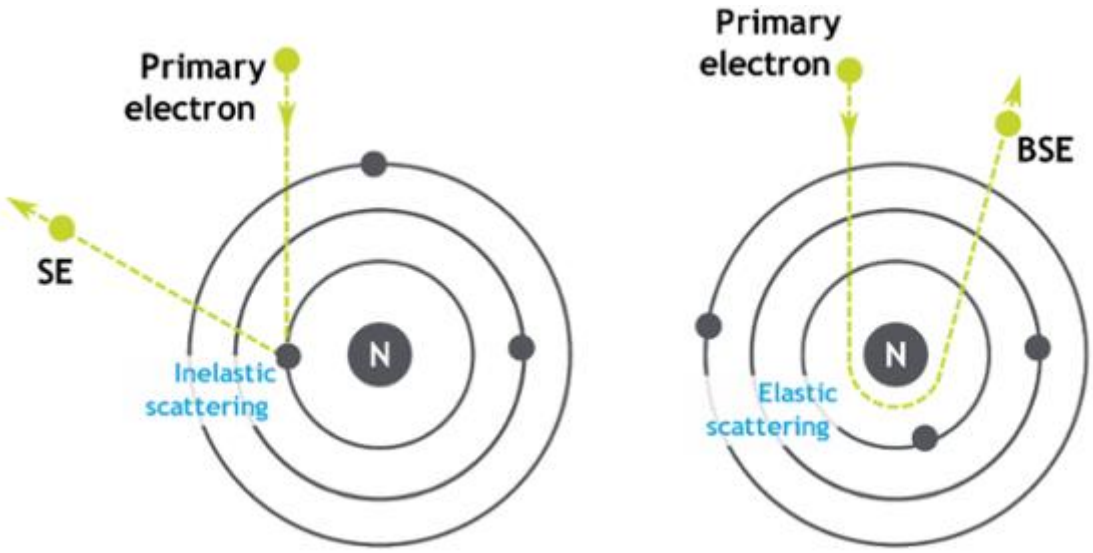

Figure 17: The generation of electrons (secondary electrons and Backscattered electrons)

4.2.3.1 Backscattered Electron Imaging

They result from elastic collisions of electrons with atoms, which result in a change in the electrons' trajectories. Accelerated electrons that are elastically scattered through an angle of more than 90˚ are called backscattered electrons (BSE) and yield a valuable signal for imaging the Sample. This happens because the electron interacts with positively charged fields in the material originating from the atom's nucleus. A BSE is defined as one that has undergone a single or multiple scattering events and comes out from the surface with an energy greater than 50 eV. Element with a higher atomic number is much stronger scatterers of electrons than of less atomic number, generating a higher signal. Result in the higher the atomic number, the brighter the material appears in the image. The backscattered electrons help illustrate the contrast between the different compositions in the multiphase Sample. The diffracted backscattered electrons generate important details about crystallographic orientations and the overall material structure.

4.2.3.2 Secondary Electrons

The inelastic interaction between incident electrons and the outer, which is not strongly bounded electron of the atom, is responsible for the generation of secondary electrons. These outer electrons can be ejected from the atom with energies lower than 50eV. If these "secondary" electrons are produced near the surface, and their energy is higher than the surface energy (~6eV), they can escape to the vacuum and reach the detector.

Secondary electrons are useful for the inspection of the topography of the Sample's surface. The signals contain information about sample surface morphology, crystalline structure, and orientation together with the chemical composition [62]. Different detectors collect the signal data over a preselected surface area; this generates a 2-dimensional, high-resolution image displaying the various and distinct discrepancies in the material. In general Everhart-Thornley detector is the most frequently used device for the detection of secondary electrons. The detector is situated at the side of the electron chamber at an angle to increase the efficiency of detecting secondary electrons.

4.3 Hardness Test Machine

The Vickers hardness test is used for a wide range of applications used for macro and microhardness testing. It has a broad load range and is suitable for a wide range of applications and materials. The rectangular indentation made by the indenter is measured to determine the hardness value. The diagonals are measured by an optical microscope attached to the machine. The hardness evaluation can be done using a universal or microhardness tester; for all materials, the same indenter (a pyramidal diamond) can be used irrespective of hardness.

4.3.1 Principle of Working

A pyramid-shaped diamond indenter with a square base and an angle of 1360 is forced onto the sample surface for a specified time. Then release the load measure the diagonal length of the indentation (ISO 6507-1). The indentor used in the Vickers test is shown in F figure 9.

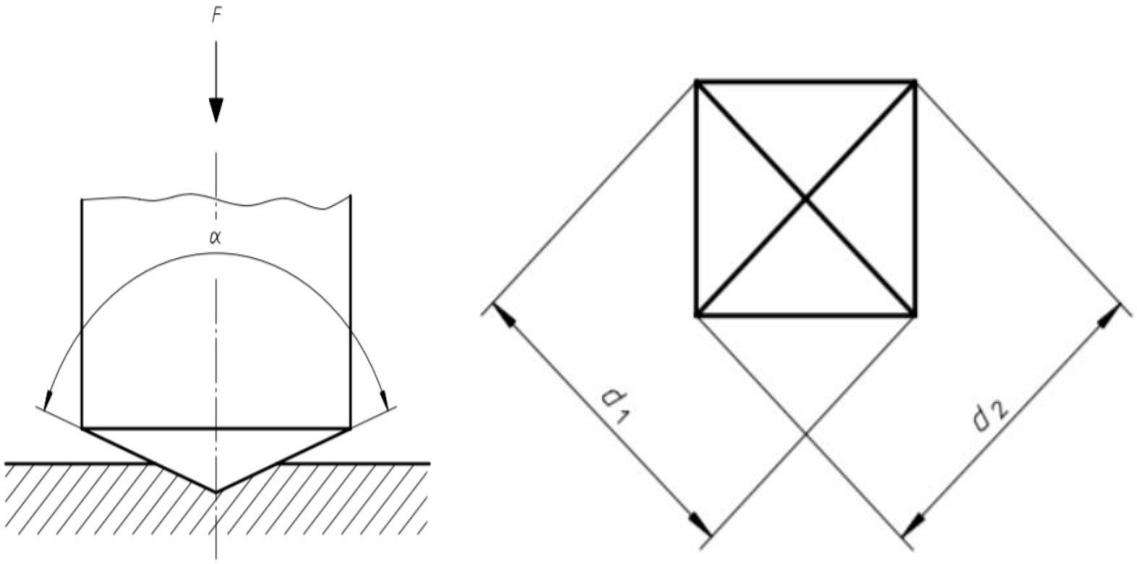

(a) Indentor(diamond pyramid) (b) Vickers indentation

Figure 18: Principal of hardness test

Calculation: The hardness value of a test sample is calculated using the formula given in equation 10. The unit for hardness number is represented by Vickers Pyramid Number (HV).

$$\text{Vickers Hardness (HV)} = 0.1891 \ \frac{F}{d2} \quad \text{equation 10}$$

Where;

F-Test force, in newtons

d-Arithmetic mean, in millimeters, of the two diagonals length d1 and d2 (see figure1)

The hardness evaluation must be carried out on an even and smooth surface, free from oxide scale, foreign material, and lubricants unless. The force used for indentation is standardized and can be found in ASTM- E-384. This also gives the information about the minimum distance between two successive indentations to be 2.5d, which is the same for the distance between indentation and any edge [63].

4.4 Tensile Test Machine

A Tensile is the most fundamental mechanical test performed to determine a material's mechanical properties: yield strengths, tensile strengths, elongation, and reduction in area at room temperature cylindrical rod. Instron 5985 dual column floor frames tensile test machine

was used to obtain the information about mechanical properties of 316L as printed using the SLM process. The test machine has a maximum capacity of 250KN and a vertical test space of 1430mm. Special fixtures and gripping for the threaded cylindrical rod for the Sample we had. A contacting gauge extensometer was attached to the specimen to measure the strain during the test, which shows the reading in computer Bluehill® software [64].

4.4.1 Principle of Operation

The system communicates primarily through the controller, which consists of sensor conditioning cards for the system transducers and transfers data between the transducers and the computer. The controller also communicates with the load frame via a frame interface [65]. The major components of an include a Load frame, with the integral controller, Load cell mounted to the crosshead, and Grips for tension testing or table-mounted anvils on a platen for compression testing. The software used for testing in Instron 5985 series is Bluehill® software [65]

4.4.2 Main Components of Instron 5985

The machine has hardware controls and software controls. The hardware controls consist of: Emergency stop button: it is used to prevent the crosshead immediately when an unsafe condition exists. Limit stops: these must be set before each test session to guard the operator against unexpected crosshead movement. Control panel: These include starting and stopping a test and using the jog controls to position the crosshead before installing a specimen. It is also used to perform certain functions at the frame instead of at the computer. The software control of the testing system is carried out via Instron Blue hill software. Blue hill software sets the parameters, operates the system, collects the data, and displays it on the screen [64].

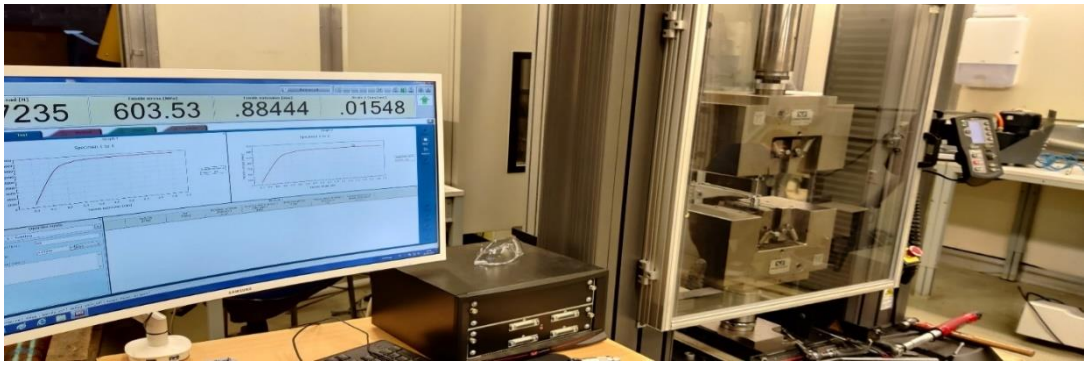

Figure 19: Tensile test machine(Instron) used for the experiment

Component	Description
Load Frame	The load frame comprises a base, one or two columns, a moving crosshead, and a top plate. It is a high stiffness support structure against which the test forces react. Each column comprises a guide column and a ballscrew. The crosshead is mounted on both the guide column and the ballscrew. Rotation of the ballscrew drives the crosshead up or down while the guide column provides stability.
Controller	The hardware that controls the frame and any ancillary equipment connected to the testing system. The controller panel contains all the connectors for load cells, extensometers and any other sensors that are required for testing.
Control Panel	The hardware panel, mounted on the side of the load frame, that lets you perform some of the software functions directly at the frame.
Load String	Comprises all of the components that you install between the moving crosshead and the load frame base (or fixed crosshead). Typically this involves a load cell, a set of grips, any adapters that are required to connect the components, and the specimen to be tested. Typically, you mount a load cell on the crosshead, then a pair of grips or fixtures on the load cell and frame base. The grips or fixtures secure the specimen and when you start a test the crosshead moves up or down applying a tensile or compressive load to the specimen. The load cell converts this load into an electrical signal that the software measures and displays.
Bluehill Software	Instron testing software that controls the testing system, running tests and analyzing test data to produce test results.
Specimen	A single piece of material to be tested.

Table 4: Testing system components of Instron[64]

4.5 V-Charpy Test Machine

The V-Charpy impact test is performed to determine the impact toughness or impact strength of a particular specimen. Zwick Roel Charpy testing machine and a V-notch specimen are used to experiment. The toughness of a metal is determined by measuring the energy absorbed in the fracture of the specimen when the pendulum from the Charpy impact test machine strikes the specimen placed between the anvils. A Charpy test for a particular metal must be done repeatedly, so this process produces a graph of impact toughness for a material.

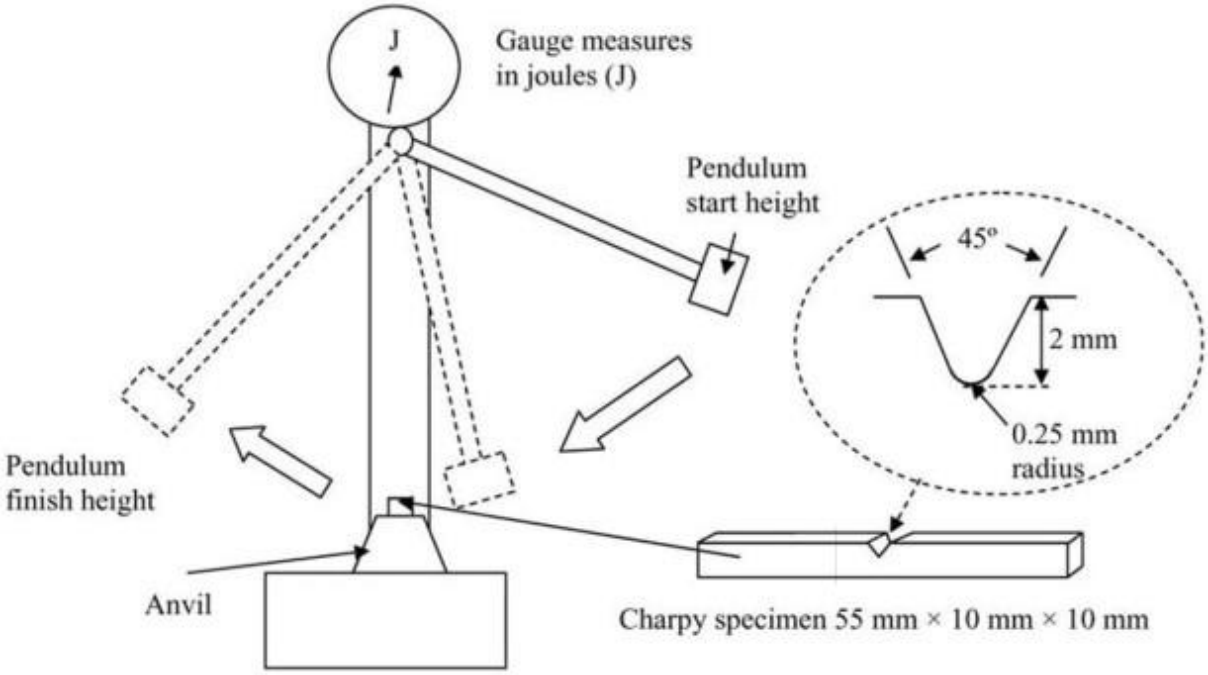

Figure 20: Schematic representation of V-notch impact test

Zwick Roel Charpy impact testing equipment was used to perform the impact energy evaluation of samples. This equipment helps us determine the amount of energy absorbed during fracture; the absorbed energy measures the material's notch toughness. This whole process is a high-strain test. A swinging pendulum from a certain height strikes a standard notched specimen with a specific weight [66]. The ASTME23 standard was followed to perform the experimental evaluation.

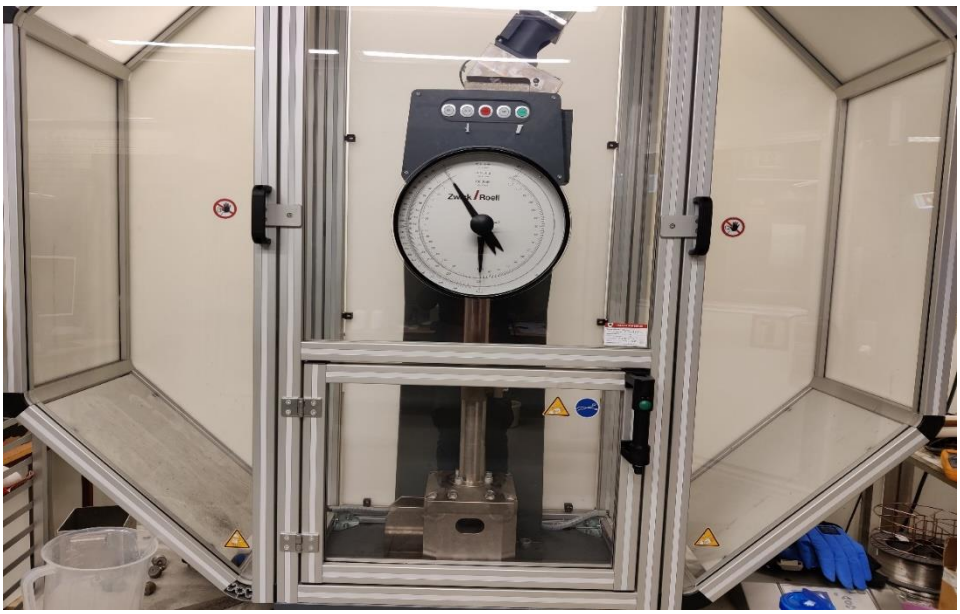

Figure 21: Zwick Roel Charpy testing machine

CHAPTER 5: METHODS

5.1 Micrographic Inspection

5.1.1 Sample preparation

The material (3D printed 316L) for mechanical and microstructural analysis was cut into three sections and marked to recognize them during their examination. Top surface marked as 1T, bottom surface as 2B and side surface as 3B, and section of position A and position D as top A and top D, respectively. Then, specimens were cast to make it easy to hold them during grinding and polishing, shown in figure 19.

Grinding and polishing:

The grinding and polishing aim to obtain a smooth, deformation-free, scratch-free, dust-free, and highly reflective sample surface. Grinding and polishing were done using Struers Pedemax-2 available in the University of Stavanger Lab. The procedure used for grinding and polishing followed the standard ASTM E03-11(2017) – Standard Guide for Preparation of Metallographic Samples. In the beginning, silicon carbide (SiC) paper with grit sizes of P220(68µm) for 3 minutes using Struers Pedemax-2 grinding and polishing machine, then the Sample and sample holder were cleaned with water for 1.5 minutes using automating washing machine. This procedure is repeated for grit sizes of P500(30 µm), P1200(15 µm), and P2400(8 µm); water was used as a lubricant. When the grinding with SiC paper was finished, samples were polished using a polish pad with 9, 3, 1 µm diamond suspension for 8 minutes using Struers DP Lubricant-Blue. Samples were cleaned at each step with distilled water. In the grinding and polishing at each stage, cleaning is essential to prevent the contamination of sample surfaces. Finally, a 0.04 µm, the op-s suspension was applied for 10 minutes. These samples were used for porosity Analysis, Hardness evaluation (1T, 2B,3B, and D top), where for sample top A, Etching was done with oxalic acid for 30 seconds.

5.1.2 Micrographic Inspection Using SEM

The specimen to be examined was cleaned using an ultrasound bath to remove any contaminants to reach the vacuum chamber. The bath was performed in a Struers Lavamin, an automated ultrasound bather before each session in the SEM. Then, the specimen was attached on pin stub specimen mount using double-sided carbon tape. Since it is necessary to conduct the electrons that reach the sample surface, and the samples were mounted in acrylic

resin, a conductive double-sided carbon tape was used to complete the circuit. To reduce the influence of unwanted effects such as astigmatism and the resulting wobble of the electron beam, chromatic- and spherical aberrations, and diffraction, the settings needed to be carefully adjusted depending on which type of detail was to be evaluated with respect to acceleration voltage, working distance, aperture, and detector.

The working distance (WD) of 10-15 mm, the accelerating voltage was applied for 15KV, and aperture size for 30 um used for secondary electron detection. Preceding the electron backscattered electron (EBSD) imaging, the casted samples needed an overall size reduction to fit the EBSD specimen holder. The working distance (WD) was used for around 10-15 mm, and the accelerating voltage was applied for 20KV. Aperature size for 60 um used for EBSD. The resulting signals generated when the scanning beam impinges on the surface of the specimen include both emission electrons and backscattered electrons.

These signals vary because of differences within the surface topography because the scanning beam is swept across the specimen surface. The emission of electrons from the specimen surface is typically confined to a neighborhood near the beam impact zone that allows images to be obtained at a comparatively high resolution. A typical SEM features a working magnification range of from 10 to 100,000 diameters. A resolution is often attainable of 100 Angstroms, and a depth of field (focus) 300 times that of an optical microscope and having reasonable working distances. The significant depth of field available with an SEM makes it possible to watch three-dimensional objects in Stereo. The three-dimensional images produced allow different morphological features to be correctly interrelated and analyzed.

The top surface of sample A was performed for microscopic inspection, which was printed at position A and in Z-build direction, represented in figure 22. Etching was done with oxalic acid for 30 seconds after grinding and polishing, as we discussed in sample preparation.

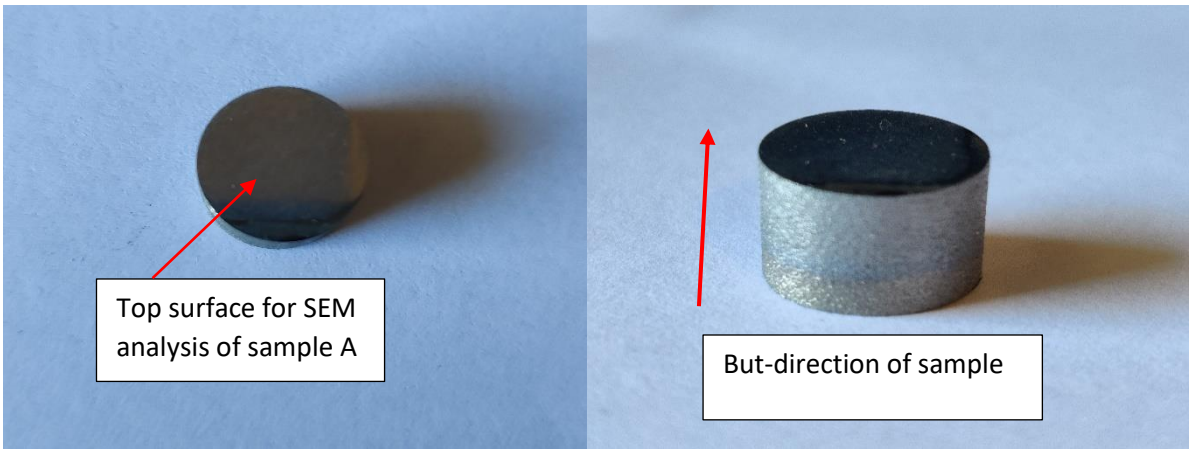

Figure 22: Prepared sample surfaces for microstructure study

5.2 Porosity Analysis

Porosity analysis is performed using ImageJ software after getting the image from a Scanning electron microscope or optical microscope. However, in this thesis, we used images from the Optical Microscope. The essential toolbar of ImageJ using for analysis is shown in the figure 23.

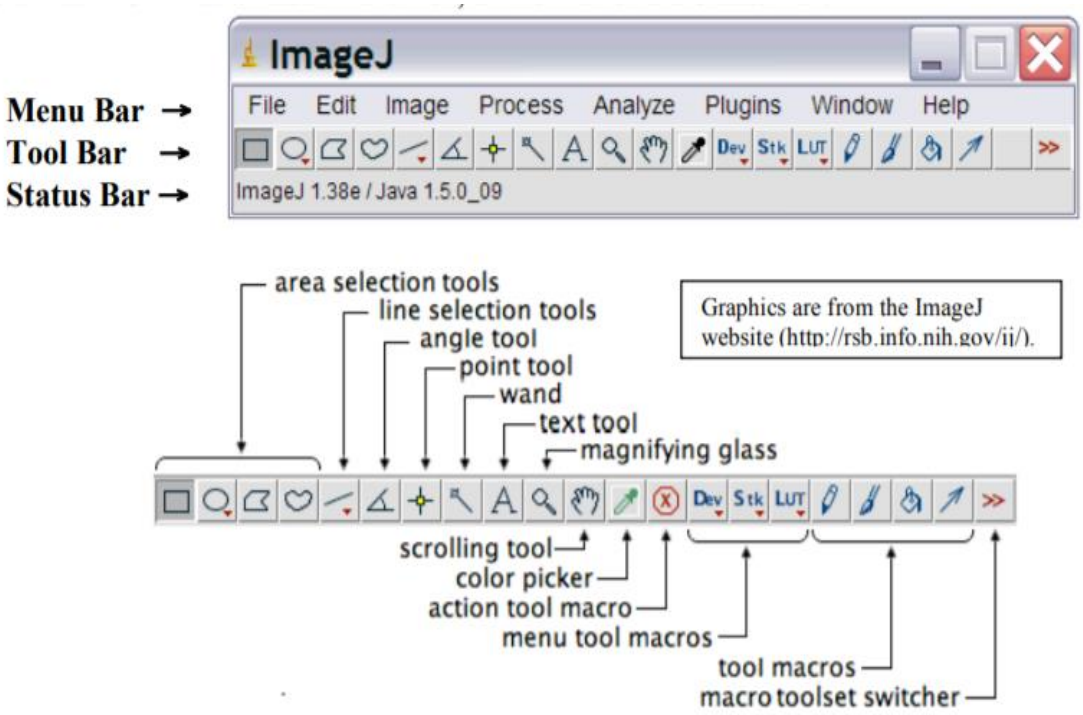

Figure 23: Image of the toolbar of ImageJ

Basic steps:

Removing Noise: go to process on the toolbar. Process → Noise → Click on Despeckle.

Convert to Grayscale: Image → Type → 8-bit converts the image to 256 shades (8-bit) of gray.

Create Thresehhold: click on image → go to Adjust → press Threshold; it will show some more features such as adjusting the slider to get optimized threshold. Then Click 'Apply' to complete the conversion. It has a Brightness adjustment slider also to get the required brightness of an image.

Set Scales: Go to analyze →click Set Scales. In the Set Scale window, the length of the line, in pixels, will be displayed. Type the measured distance by drawing the line on the image in the set scale window click OK global to apply to use this scale for other image frames.

Set Measurements: Go to Analyze→set measurements different parameters will be displayed on a window. Select the parameters to be measured.

Area measurement: select the area with an area selection tool, the wand (for high contrast images), or Analyze Particles.

Analysis: Go to Analyze → Analyze Particles, type the upper and lower limits for the particle size, toggle 'show outlines,' and check 'Display Results.

Histogram and profile plot: →Analyze → histogram or profile.

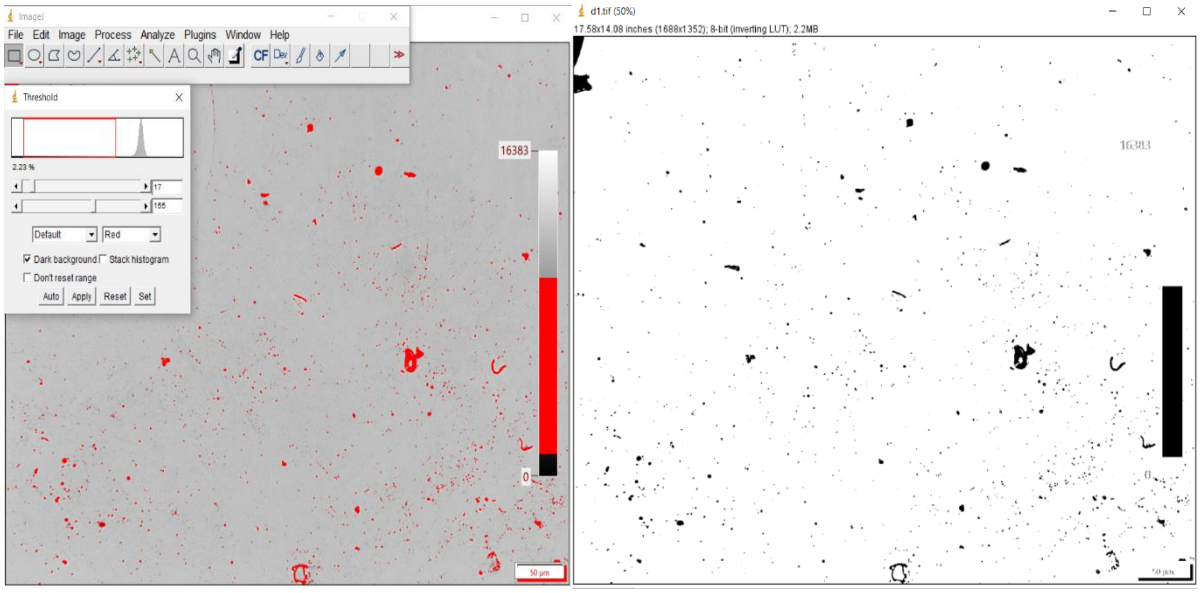

Figure24: Threshold creating; On the left before applying threshold and on the right After completing a threshold

Figure 24 shows that threshold created image, ten surfaces for different samples were investigated for porosity analysis; the results and graphs are discussed in the result and discussion chapter.

5.3 Hardness Evaluation

5.3.1 Sample Preparation

The surface for the hardness evaluation made smooth and even by grinding and polishing.

Sample Surfaces were prepared in such a way as to prevent surface damage or alteration of the surface hardness. And, sample surface was free from any oxide scale, dust particle, lubricant, or grease to get an accurate measurement of diagonal lengths. Grinding and polishing were done using Struers Pedemax-2 available in the University of Stavanger Lab. The procedure followed the standard ASTM E03-11(2017) – Standard Guide for sample Preparation of Metallographic. Four samples were prepared for hardness evaluation, as shown in figure 19.

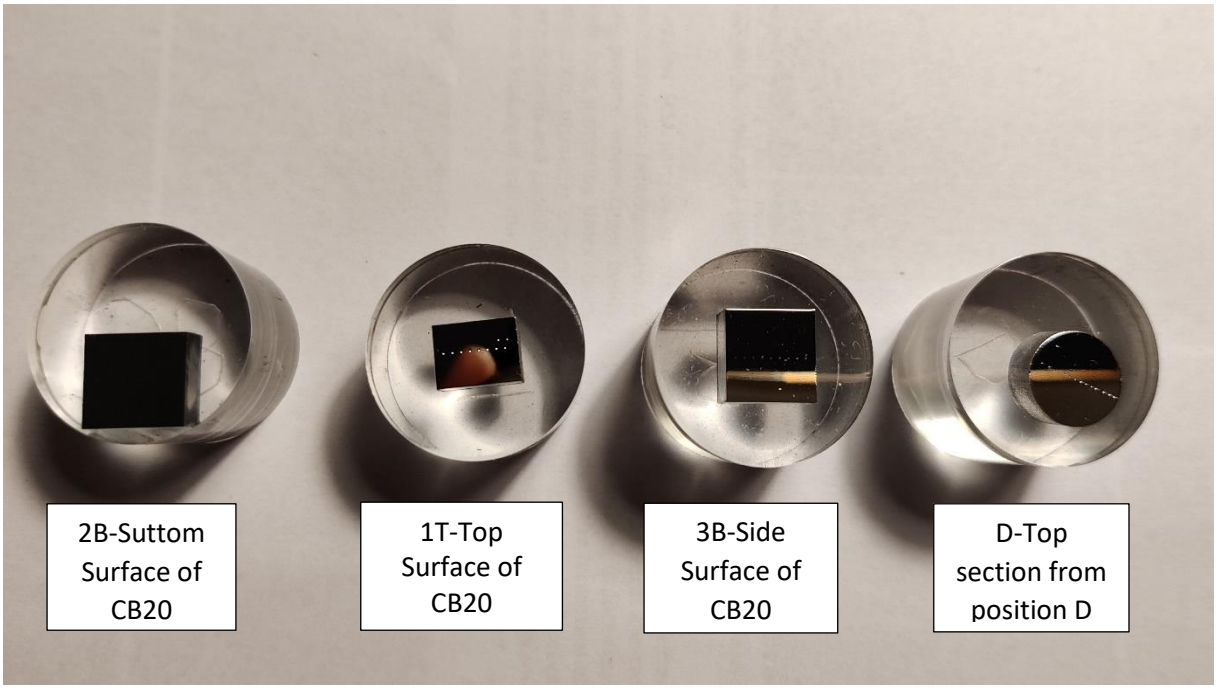

Figure 25: Samples from different surfaces and section

5.3.2 Hardness Evaluation Procedure

The hardness testing was conducted on a Struers DuraScan Testing machine is shown in the figure. The 5kg load was applied with a dwell time of 10 seconds for the indentation. The hardness test was conducted following the standard. Testing was started by turning on the Struers hardness testing machine, then Sample was Placed on the stage and made sure that the sample surface is perpendicular to the indenter axis. Then, the Sample was positioned using a mouse and focused on a low-power objective. Selected Vickers test method and load to 5 HV. Indenter used by using overview camera. Finally, the tester was activated so that the indenter is automatically lowered and makes contact with the specimen for 10 seconds, and force was released automatically.

Now tester was switched to the measuring mode and selected the proper objective lens. Focus the image, sometimes adjust the light intensity, and apertures to get better resolution. The diagonals of the indent are measured optically to determine the hardness, using a table or formula by testing machine. The same procedures are repeated for nine more indentations, leaving the 1 mm gap between each indentation to ensure that adjacent indentation is not overlapped and ruin the test.

Data collected from 10 indentations from each surface for four different samples were collected to get accurate results that would reveal any deviation in the hardness from different surfaces of the Sample provided by the Company. The result from the Vickers method is presented in the result and discussion chapter.

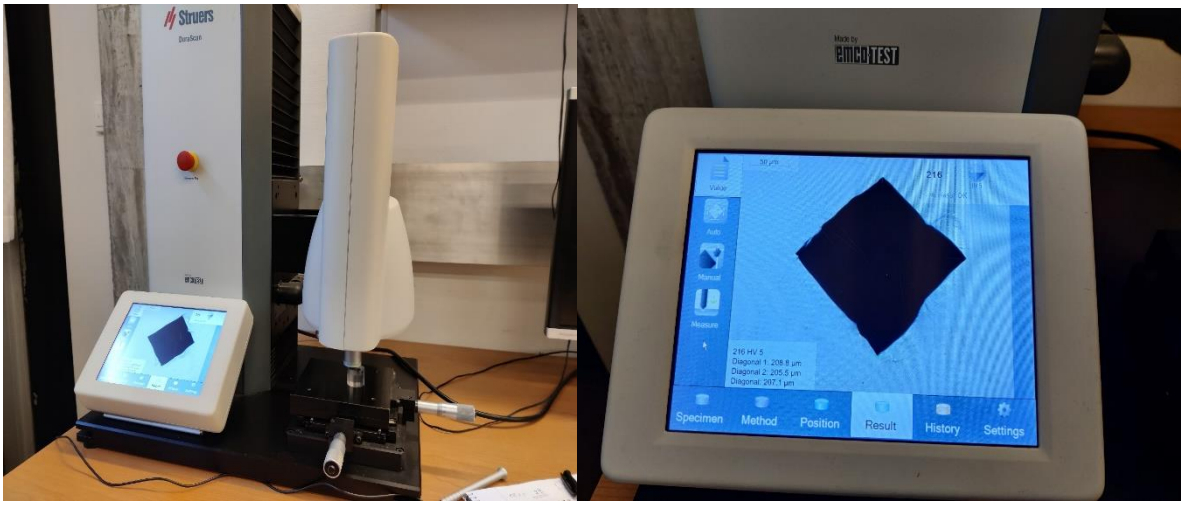

Figure 26: Vickers hardness test shows measurement mode after releasing the force(Struers DuraScan)

5.4 Tensile test experiment

5.4.1 Sample Preparation

3D printed using SLM process twelve cylindrical rods are sent from Aidro 3Dprinting and Hydraulics of dimensions are 100mm in length and diameter of 12mm were prepared following the ASTM E8/E8M-13a. Firstly, the diameters of rods were reduced to 10mm in diameter using a Lathe machine. Then, the threats were made using CNC Machine at both ends to provide sufficient grip so slip can be prevented during the test. Finally, the middle section was reduced using CNC again to get precession diameter. The specification of the Sample is shown in figure 27, and pictures of the prepared Sample are shown in figure 22.

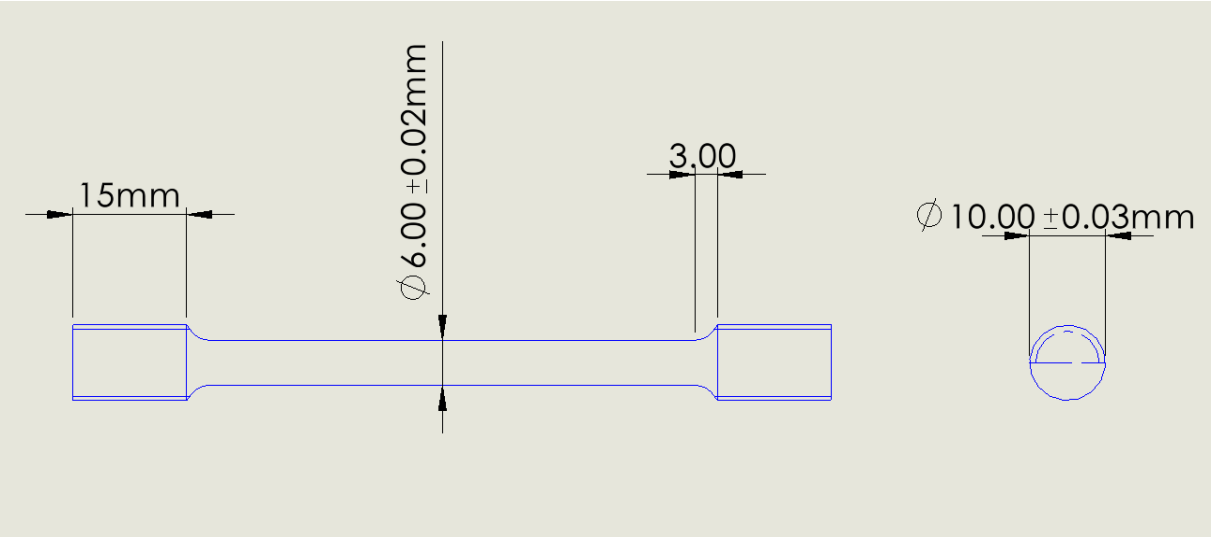

Figure 27: Sample specification for tensile test

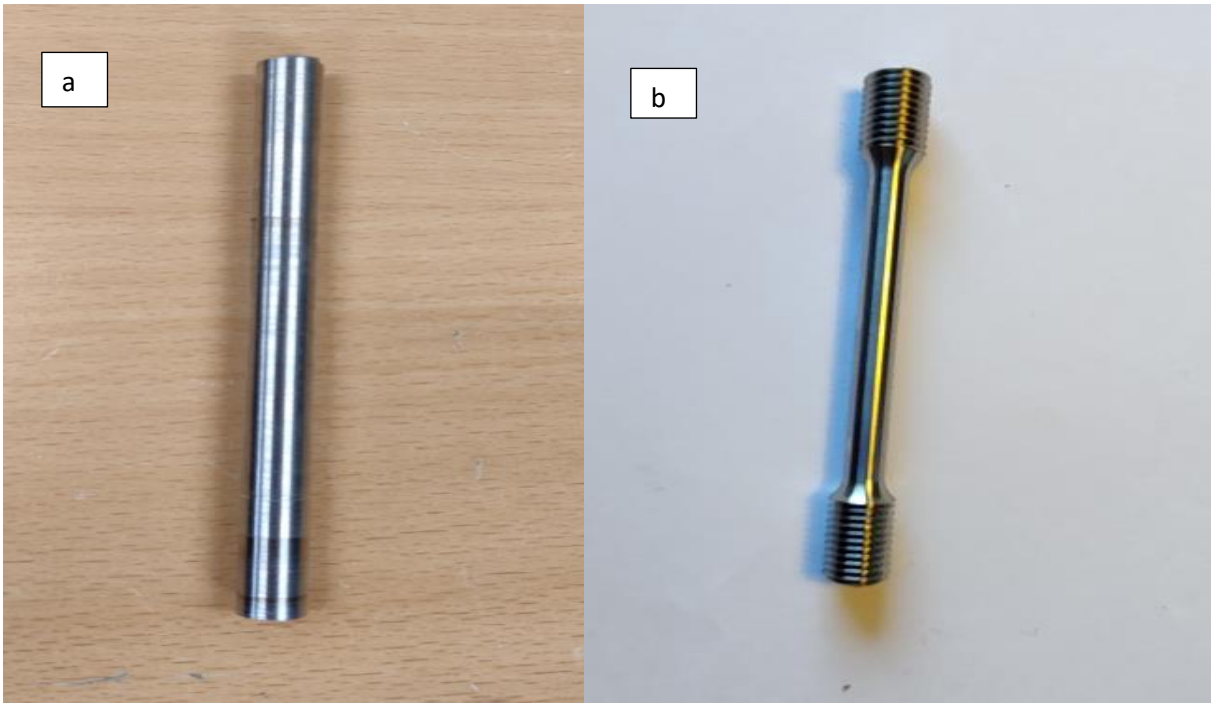

figure 28: Tensile specimen preparation (a)before preparation(b) after reduced cross-section making thread using CNC machine

5.4.2 Experimental Procedure

Tensile testing was carried out to evaluate the yield strengths, tensile strengths, elongation, and reduction in the Area of the Sample accurately following ASTM E8. However, we changed a little bit of extensometer space from the standard to allow it to fit in samples. The gauge length extensometer was used for 55mm. Specimens were checked carefully if any

presence of cracks or breaks on Sample surfaces before fit into the testing grips. Then the diameters were measured in the reduced section at three places using the micrometer. A minor diameter was used to put in Blue hill software for calculation. The straining rate was set to 0.015mm/mm/min until the yield point reached, then the rate was increased to 0.1mm/mm/min. Twelve 316L samples were tested at room temperature using the Instron 5985 Dual Column Floor Frames Tensile test machine available in the University of Stavanger lab.

Figure 29: Prepared 316L Samples for tensile testing

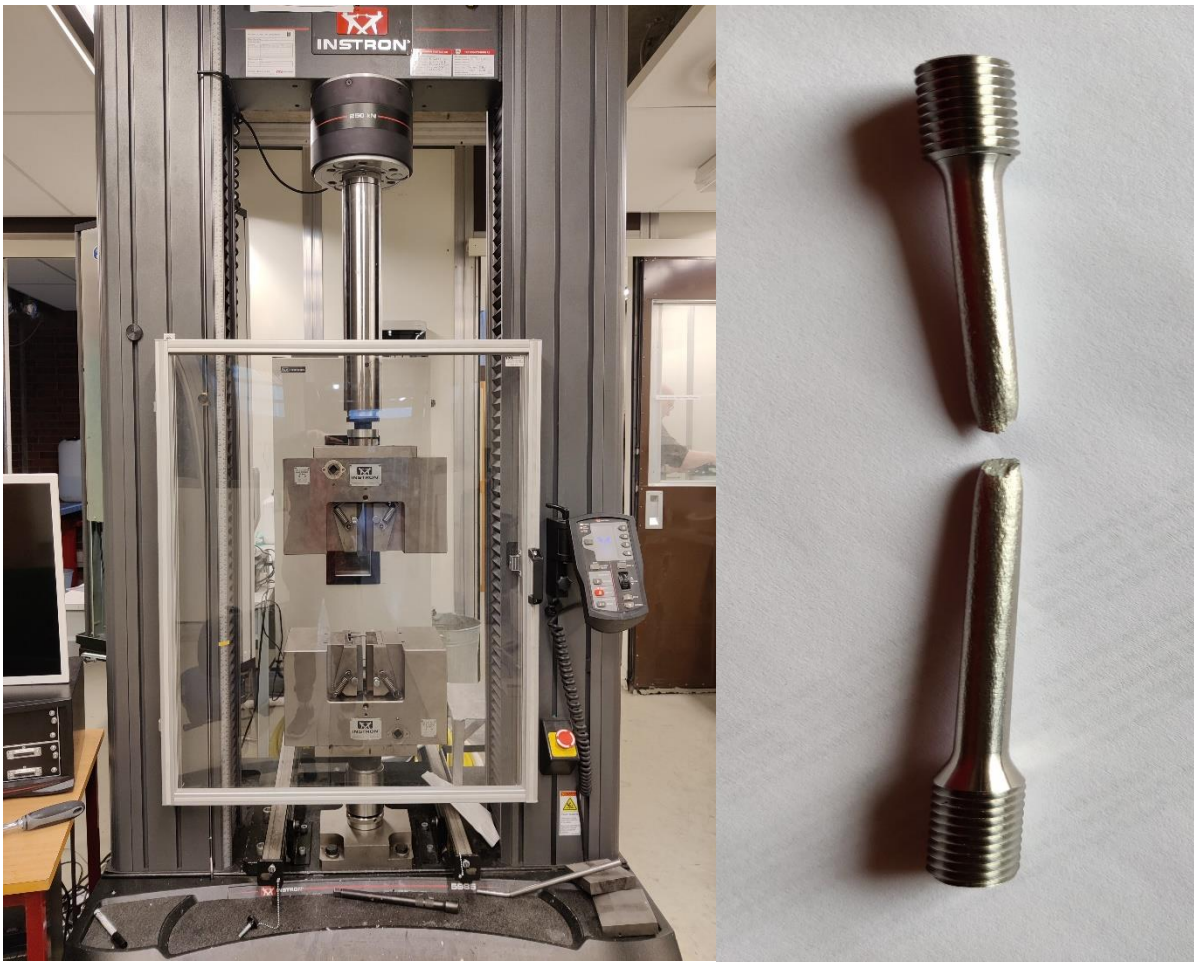

Figure 30. Instron tensile test machine on the left and broken specimen after test on the right.

5.4.3 Calculation Methods

Yield strength (σ_y), Tensile strength (σ_u) are calculated by the Blue hill software and shows on computer screen.

Percentage elongation: the extension at break is measure by extensometer were collected, then %elongation values calculated using given formula.

$$\% \text{ elongation} = \frac{L-Lo}{Lo} * 100 \ = \frac{\Delta L}{Lo} * 100 \quad \text{equation 7}$$

Where, L is the final length after break and length and L0 the original length of specimen.

Percentage Reduction in Area: least diameter every specimens were measured and recorde before experiment, and after break. Then, reduction was calculated using given formula.

$$\% \text{ Reduction in Area} = \frac{\Delta A}{A0} * 100 \quad \text{equation 11.}$$

Whre ΔA= Af-A0, Af is final cross-sectional Area and Ao is original cross-sectional area of specimen.

The results and graphs from the experiment are presented in the result and discussion chapter.

5.5 Impact Energy Test

5.5.1 Sample Preparation

3D printed 316L stainless steel bars, which were built in different directions using the SLM process, were received. The dimension of samples was 57mm long and cross-section of 10*12mm; those were prepared according to standard sample specification (ASTM E23-07a). To follow the standard for testing extra material was removed using a milling machine and reduced to a dimension of 55*10*10 mm. Then notch of Depth of notch is 2mm, angle of 45 degrees at the middle of the longitudinal face (27.5 mm from the end) was made CNC machine. Specification of the Sample is shown in figure 32 (a), and prepared samples are shown in figure 32 (b) and (c).

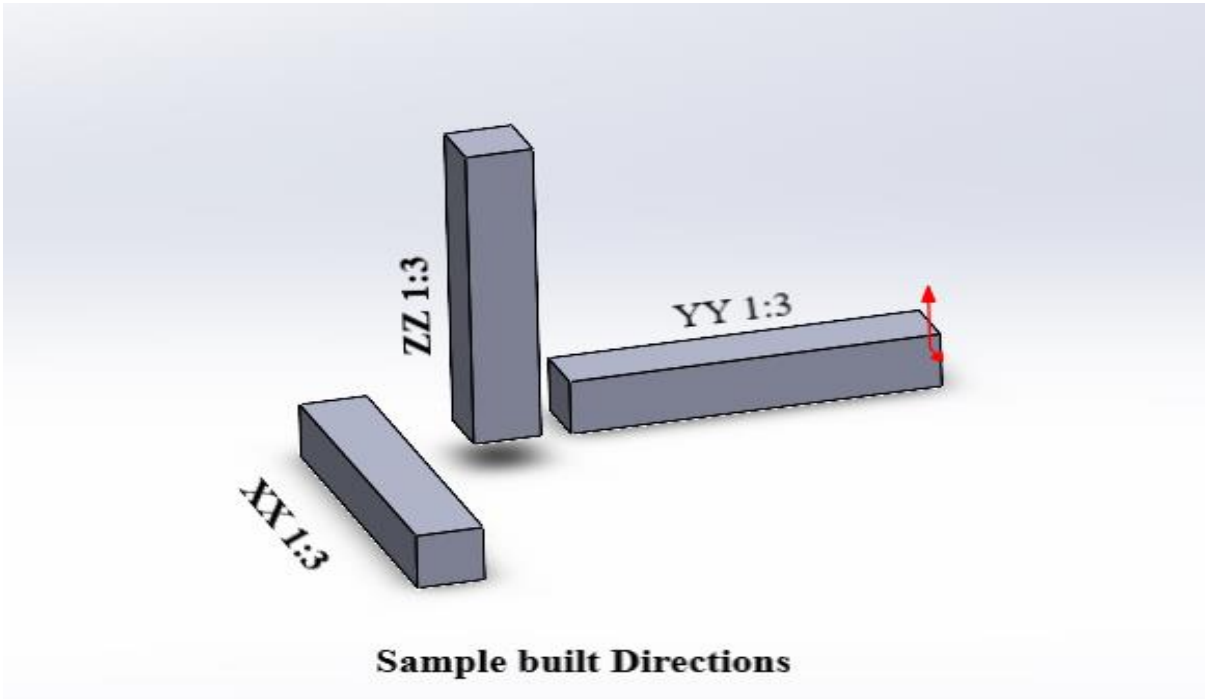

Figure 31: samples built up in 3 different directions

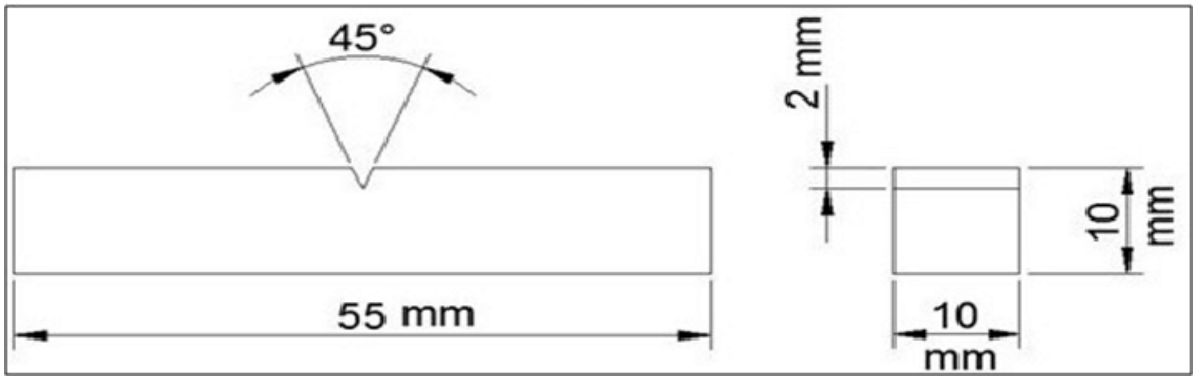

(a)

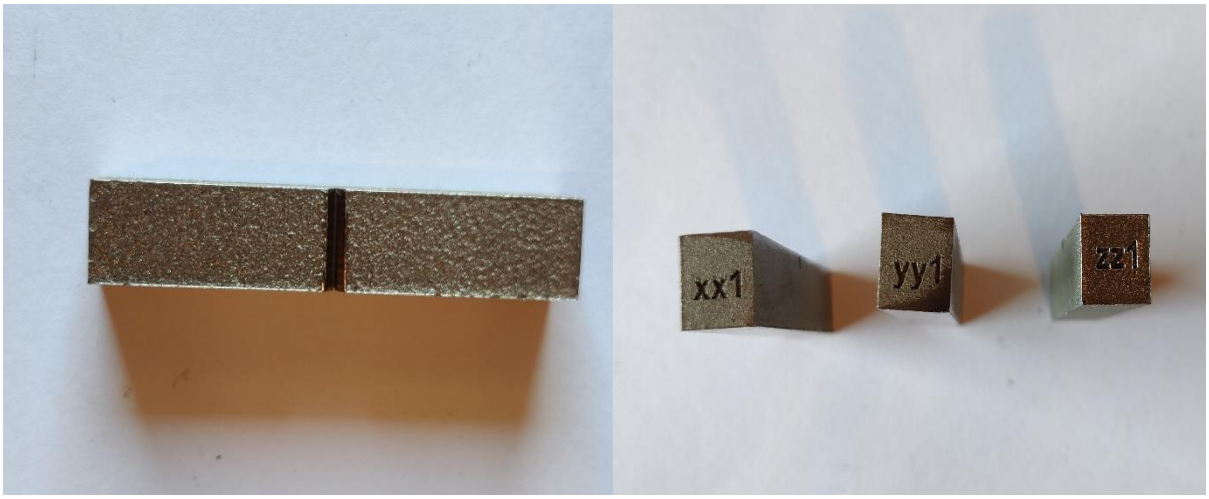

(b) (c)

Figure 32: V-Charpytest samples (a) sample Specification according to ASTM E23, (b) prepared Sample for test, (c) different samples printed in different directions.

5.5.2 V-Charpy Test Procedure

The Charpy test was conducted to get the energy required to break a 316L as printed under impact loading. Procedure for Impact energy test was followed ASTM E23 and done at room temperature. A test specimen having a V-shaped notch was placed on the holder in such a position that the notched section is in the center of the holder using a self-centering tong, as shown in the figure. Then the energy indicator was initialized as zero. Finally released the pendulum hammer, which stroke at the back of the notched section of the specimen and broken. Noted down the resulting value from the energy display. The Charpy impact value shows in the reading gauge. The procedure was repeated was for nine specimens those were build up in different direction and result was collected which are represented in the result and discussion section.

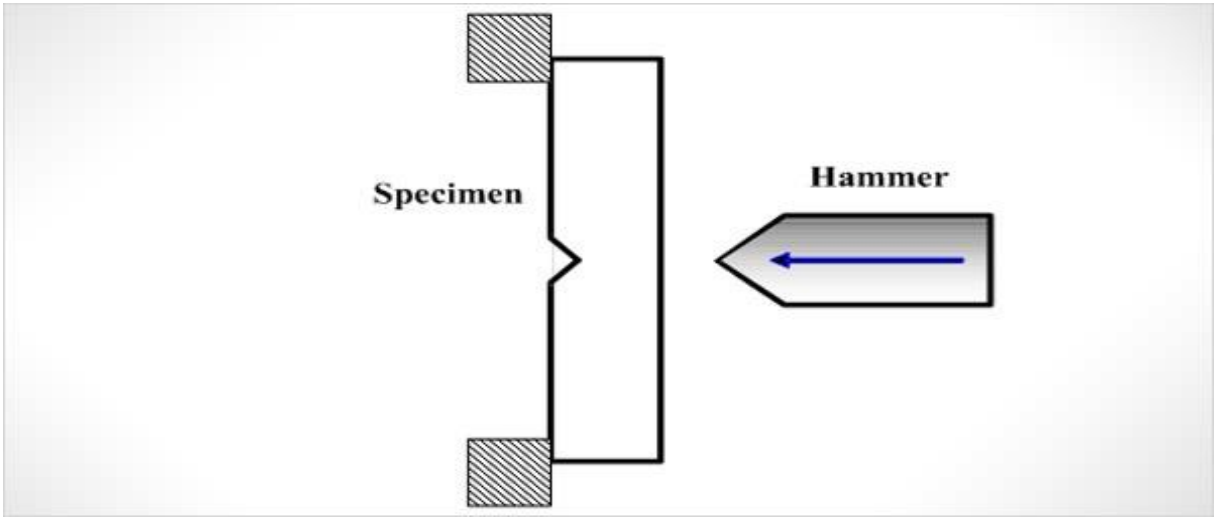

Figure 33: Sample position and direction of striking

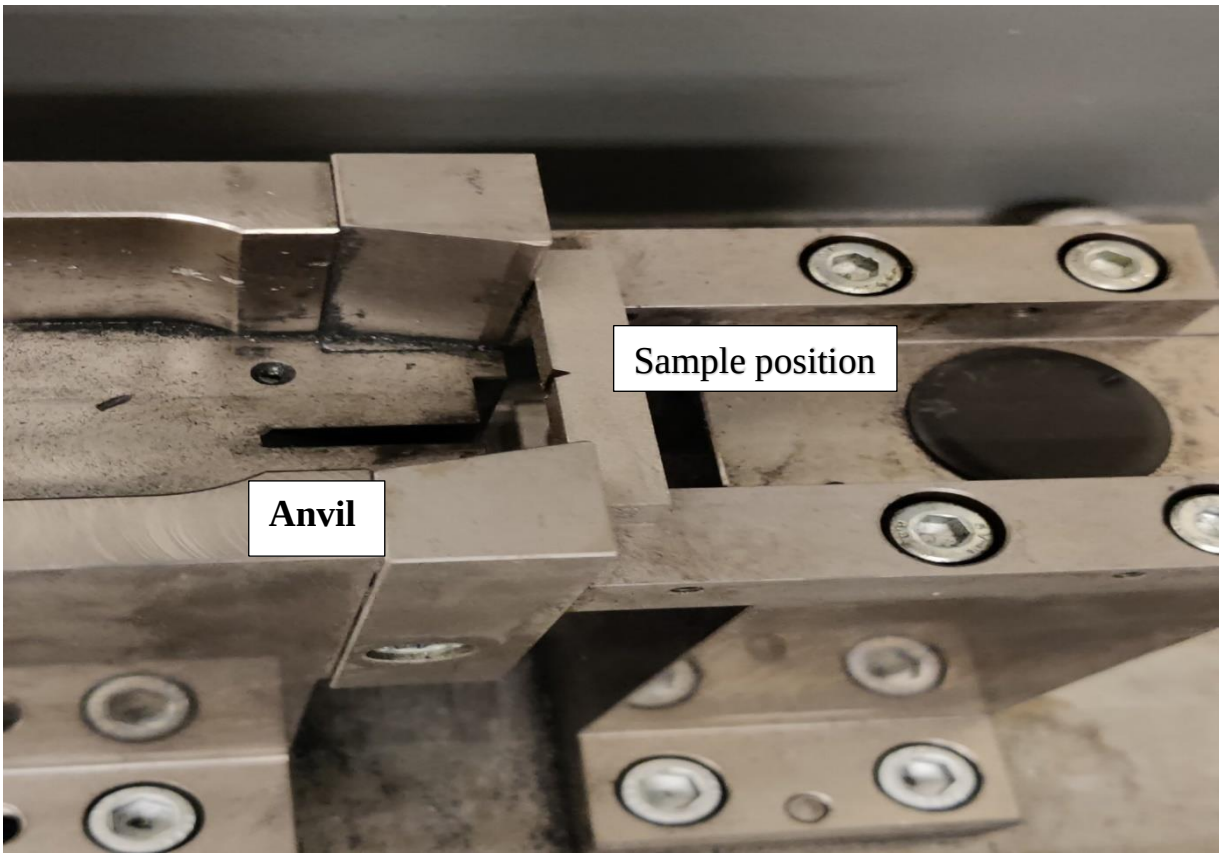

Figure 34: Image of V-Charpy testing using Zwick Roel

CHAPTER 6: RESULT AND DISCUSSION

6.1 Microstructural Study

The microstructure of the SLM-densified 316L built using the EOSM90 was analyzed using Optical microscopes and SEM. The layer thickness of 40µm, 316L as-printed not heat-treated Sample was performed macro and microstructure. The images from an optical microscope, in a parallel and normal direction to build direction, is shown in figure 35. A layer-wise morphology characterizes the microstructure.

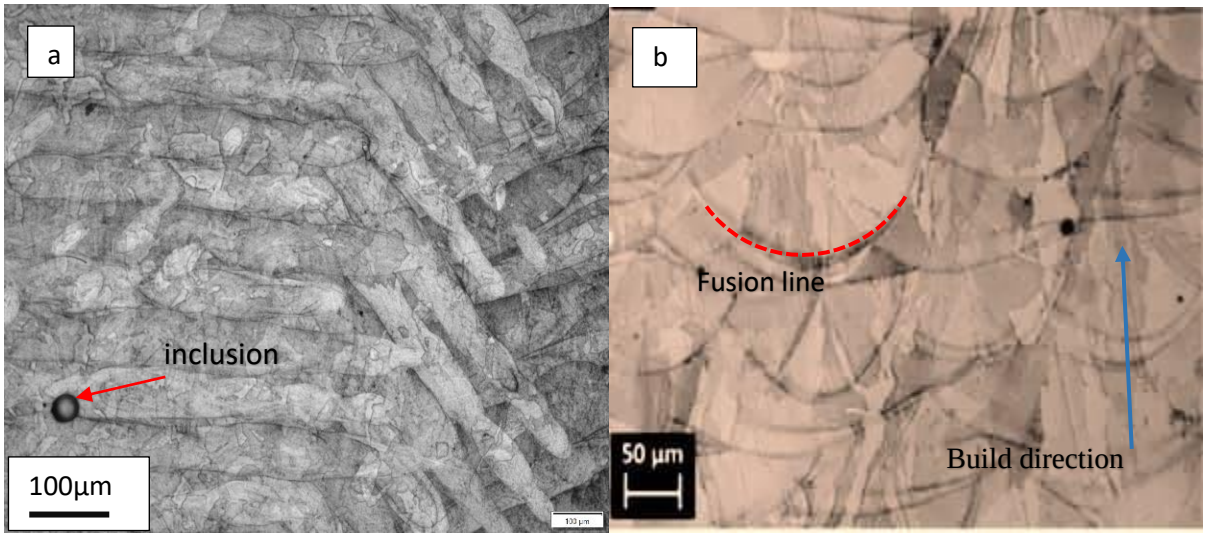

Figure 35: Characteristic optical micrographs of the top section and of the lateral section of built parts,

The as-printed 316L samples showed clear solidification tracks on the macro-scale and evidence of the solidification cell structure on the micro-scale. In characteristic optical micrographs, Figure 35 (a) shows the melting beads of powder material and (b) lateral sections of the samples we can see melt pool and fusion line clearly. The laser scanning directions are rotated with an angle less than 90 degrees after each layer, causing different orientations of melt pools, as seen in Figures 35 (a) and (b). The scanning laser beam developed periodic melt pools in each layer similar to many aligned welding beads. Their melt pool boundaries are clearly visible after etching. The size of the melt pool depend on process parameters, such as; the spot distance, input power, exposure time, and the beam size at the focal point. Laser tracks experienced partial remelting. Many grains include melt pool boundaries, suggesting epitaxial growth of new grains from remelted zones, following maximum temperature gradient directions.

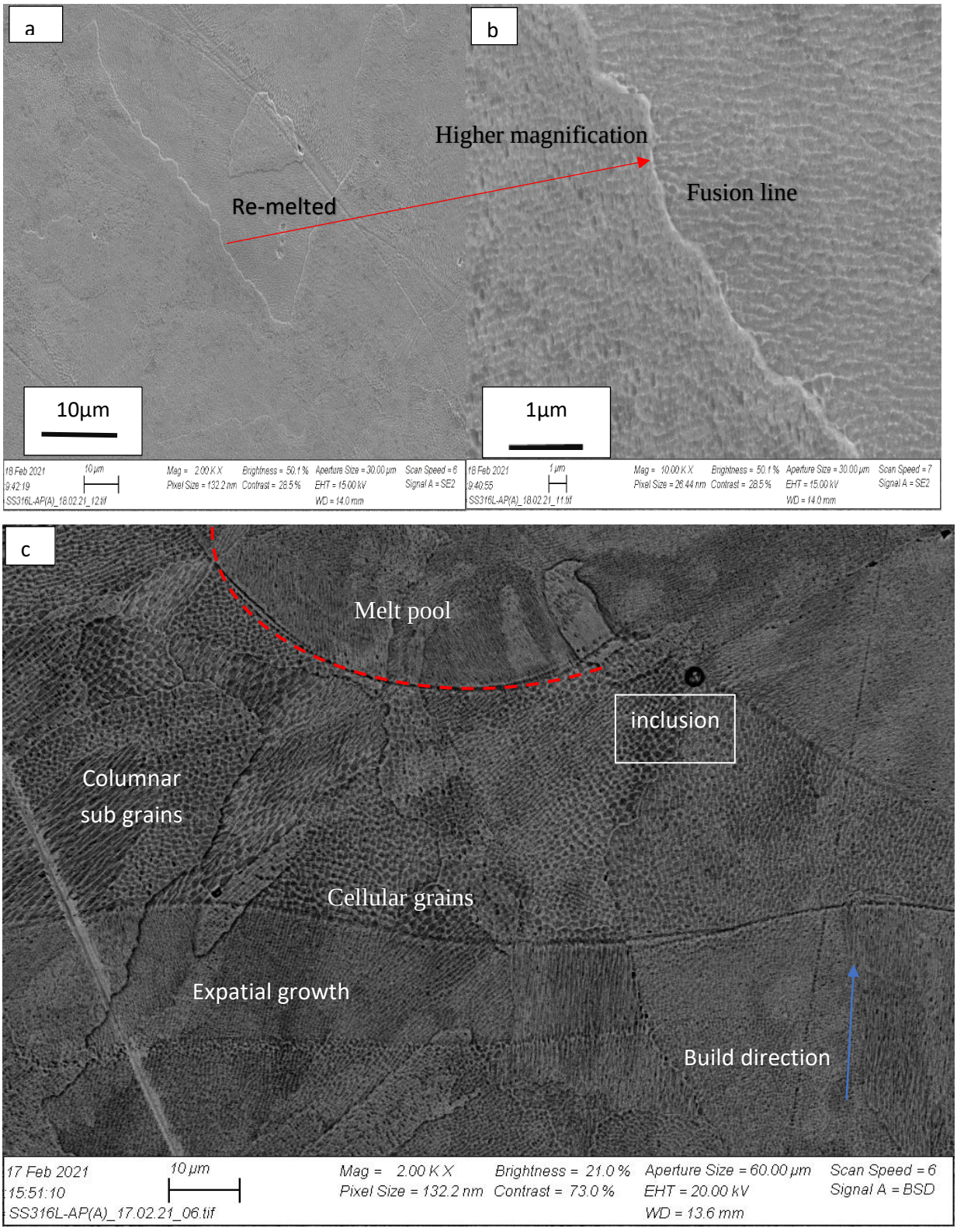

Figure 36: SEM images (a) and low magnification(b) high maginification secondary electron and, (c) BSD electron detection

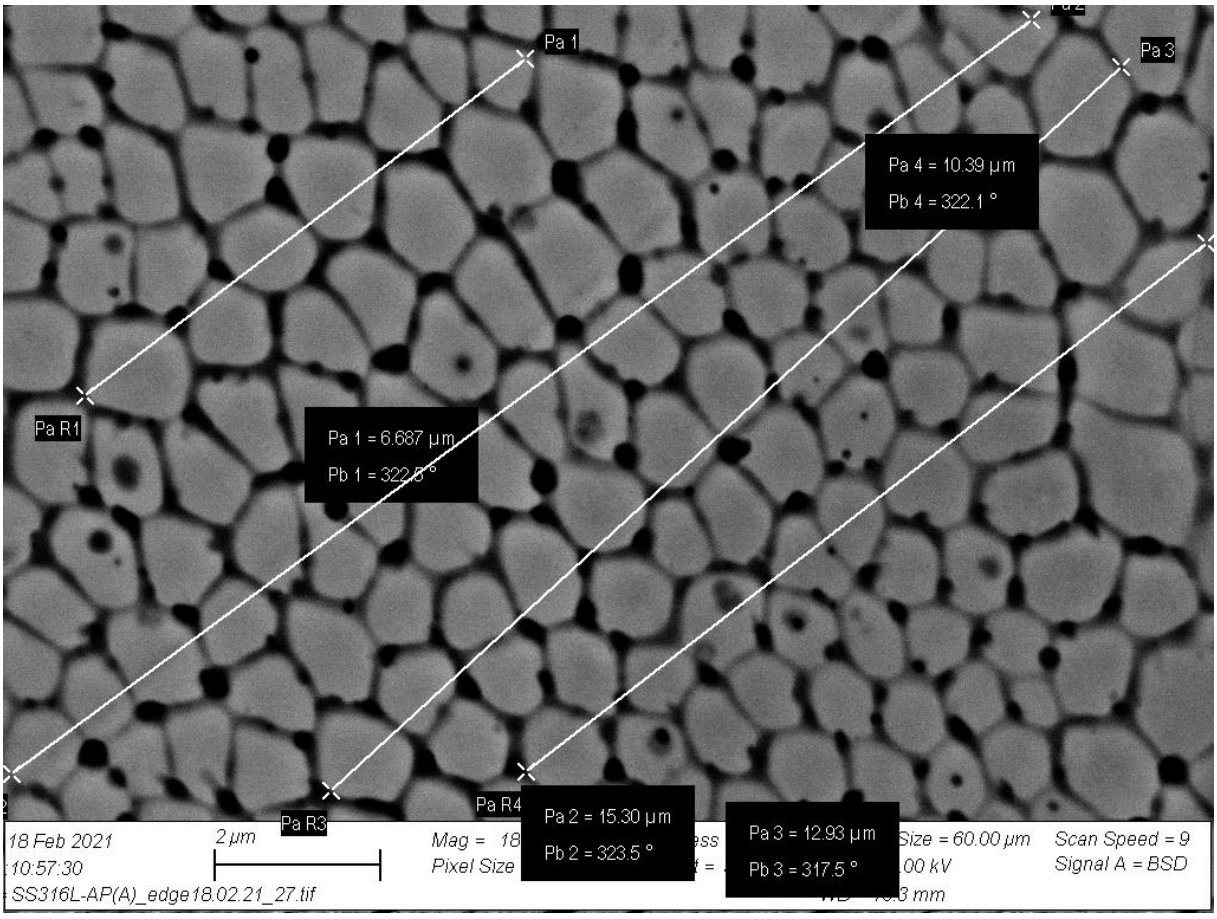

Figure 37: Measurement grain size of 316L using BSD in SEM

The secondary electrons and backscattered electrons were used for the characterization of microstructure in SEM. At higher magnification Figure 36. 2(a), (b), and (c) the fine cellular substructure is revealed and coarse columnar. Elongated intragranular cells are about one µm in and a few tens of microns in length. Similar but coarser microstructures are often produced in laser-welded beads and are favored in all those solidification processes characterized by rapid cooling rates and a large degree of undercooling. Indeed, cooling rates in the order of 103–108 K s−1 were proven to occur in SLM processes[67]. During SLM, materials experience fast local melting and solidification far from equilibrium conditions which is driven by severe temperature gradients, temperature gradients in SLM are remarkably high (order of 106 Km−1)[68]. The cellular-columnar grain microstructure reveals variable directional growth, where subsequent motel pool layers overlap, and sub-micro grains change growth direction, showing epitaxial columnar growth (Figure 36(c)).

The orientation of grains during the solidification of the new melt layer will be according to the orientation of the previously applied layer (nucleus surface), which is the energetically

favored surface for crystallization [44]. However, the heat flux affects the direction of grain growth, leading to grain growth normal to the previously solidified layers. During the solidification of the selectively melted layers, isolated grains grow towards the melt pool center. When the grains reach a particular size, their surfaces meet and form grain boundaries. If there is an inadequate amount of residual melt between the grains moving towards each other, pores and binding defects may be formed [52]. As a result, there are smaller cells within the individual grain; these present cells are considered subdomains and are characterized by a core/shell morphology.

Due to the application of new layers upon the nucleus surface, additional heat is induced into the solidified layers, representing an in situ heat treatment [47]. When the temperature is increased temporarily, diffusion of atoms and dislocation may occur. Therefore, the temperature-induced by the melting of subsequent layers is considered a significant impact on the microstructure and the mechanical properties of SLM-built materials [48]. To summarize, the microstructures of the respective specimens are similar concerning their grain size, layer thickness, substructure morphology, and grain orientation.

6.2 Porosity Analysis

Porosity is a common defect observed in the AM of metal parts, and it can be controlled by adjusting various processing parameters, e.g., hatching space, the scan speed, laser power, and layer thickness. The image from an optical microscope for different surfaces was analyzed for the porosity of as-printed 316L stainless steel using the SLM process. ImageJ software was used to analyze the %porosity by Area, Average size of pores, nature of pores, and the number of pores in the selected area which are represented in the graphs below.

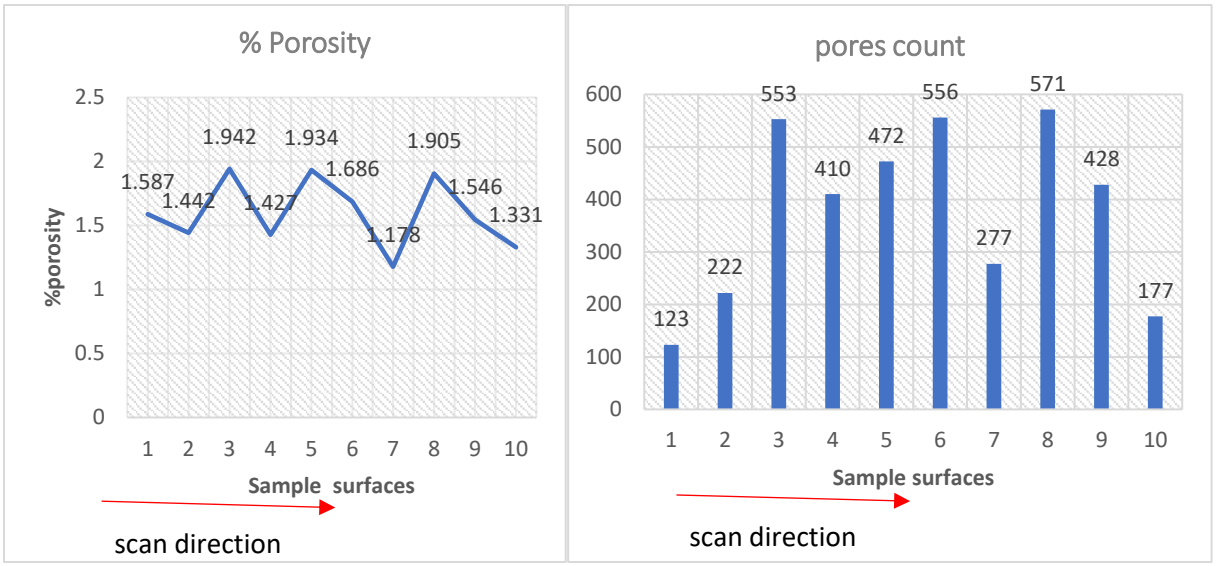

Figure 38: Porosity analysis (a) percentage porosity by area and (b)

Graph for % porosity(Figure 38(a))The average porosity of 1.59% was found from ten different surfaces; however, slight variation was observed and had a standard deviation of 0.26. Sample surfaces contain a maximum porosity of 1.905 % by area and a minimum of 1.128 %. Furthermore, the number of pores count at edges is less than the middle part of samples(figure b), with variation between 123 to 571 number of pores. The non-uniform pore distribution in this process could be caused by the variation of surface roughness or the layer-wise build manner of the SLM [69, 70].

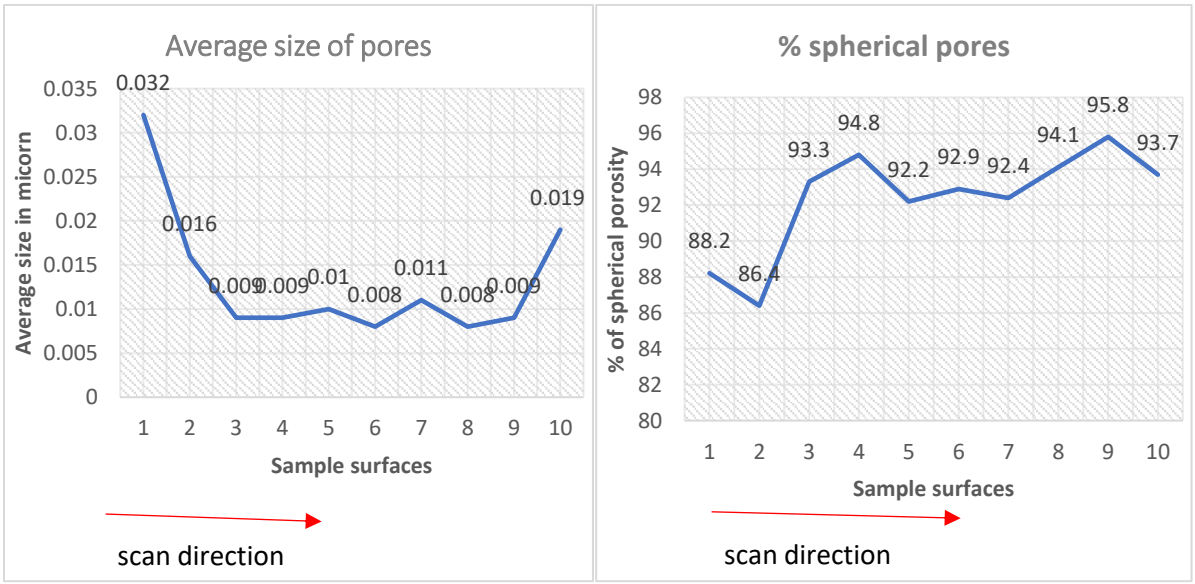

Figure 39: Size and shape of pores (a) Average size of pores, (b) spherical pores by percent.

From the graph (figure 39 (a) and (b))of the average size of pores, the size of the pores is not even in size, variation can be seen from 0.008 microns to 0.032 microns, and moreover, the size of the pores is larger at the edges compared to the mid of the samples. The nature of pores are dominated by spherical was highest 96.7% (figure b)of them and remaining were irregular shapes that we can see on the images.

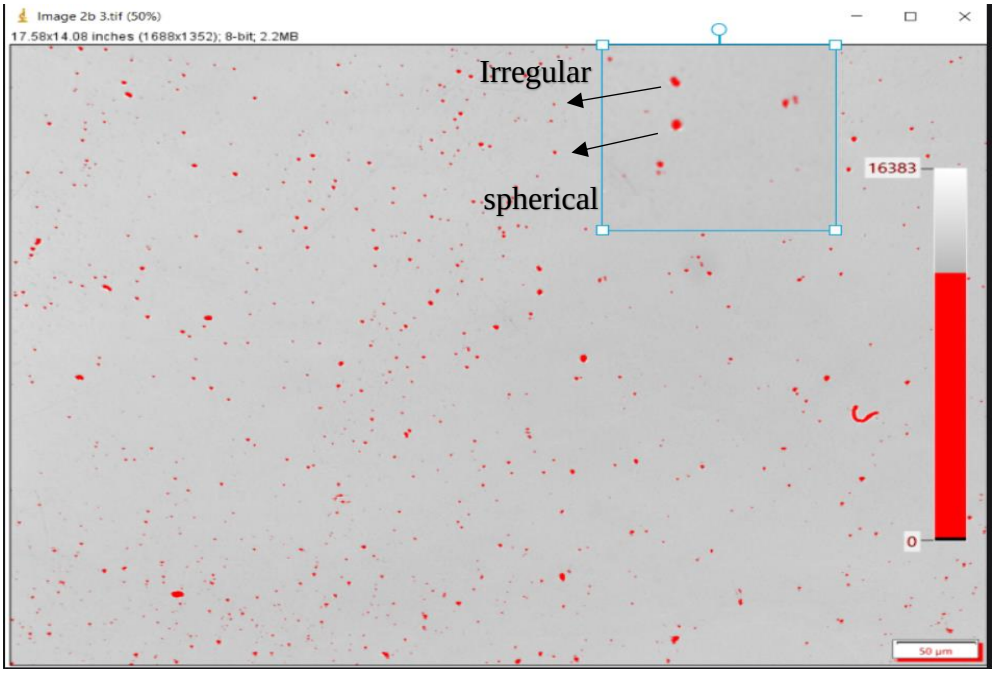

Figure 40: porosity distribution and nature of pores,

Figure 40, an image from the optical microscope of the parallel surface of 316L, shows porosity distribution and nature of pores. In general, porosity can be induced when during the gas-atomization of the powder process or during manufacturing [71]. Spherical-shaped gas pores could be developed during the gas atomization of the 316L SS feedstock material before SLM processing and continue to be present in the finished specimen. On the other hand, pores resulting from process-induced porosity are typically non-spherical. They are formed when either the energy applied is insufficient to completely melt the powder feedstock, causing a lack of fusion between each adjacent scan and between successive layers , or excessive energy is applied, resulting in spatter ejection [72].

In this study, spherical pores dominated the non-spherical ones. This indicates that most of the porosity defects in the SLM samples were due to gas pores during the gas atomization of the 316L SS powders. The gas pores could be produced due to moisture or contaminants on the

surface of the powder particles. These pores could also be formed by the reactions between O2 and C which are present in small amounts during SLM processing, causing CO or CO2 gas entrapment in the SLM-built parts [71, 72]. Nevertheless, these pores and voids are detrimental to the quality of AM-fabricated metal parts, especially as they reduce mechanical properties such as yield and tensile strength.

The method to measure porosity is x-ray computed microtomography could better and accurate result of percentage porosity, size, and distribution in AM-fabricated samples.

6.3 Hardness Result and Discussion

Vickers hardness evaluation was performed on the polished of different sections using a micro Vicker's hardness tester. The pyramid-shaped diamond indenter was used at a constant load of 5Kg. The Vickers Hardness (HV) is calculated by optically measuring the diagonal lengths of the impression left by the indenter, as shown in figure 41. Three sections from the CB20 Sample, parallel at the height of 20mmn (1T), at the height of 20 mm (2B), and normal to the built direction 3B, and the top section of position D, which is at the height of 110mm and parallel to the support plate. Each sample was subjected to ten indentations for 10 seconds. It started from one mm distant from the edge and progressed the indentation to the opposite edge leaving a 1 mm distance in each indentation.

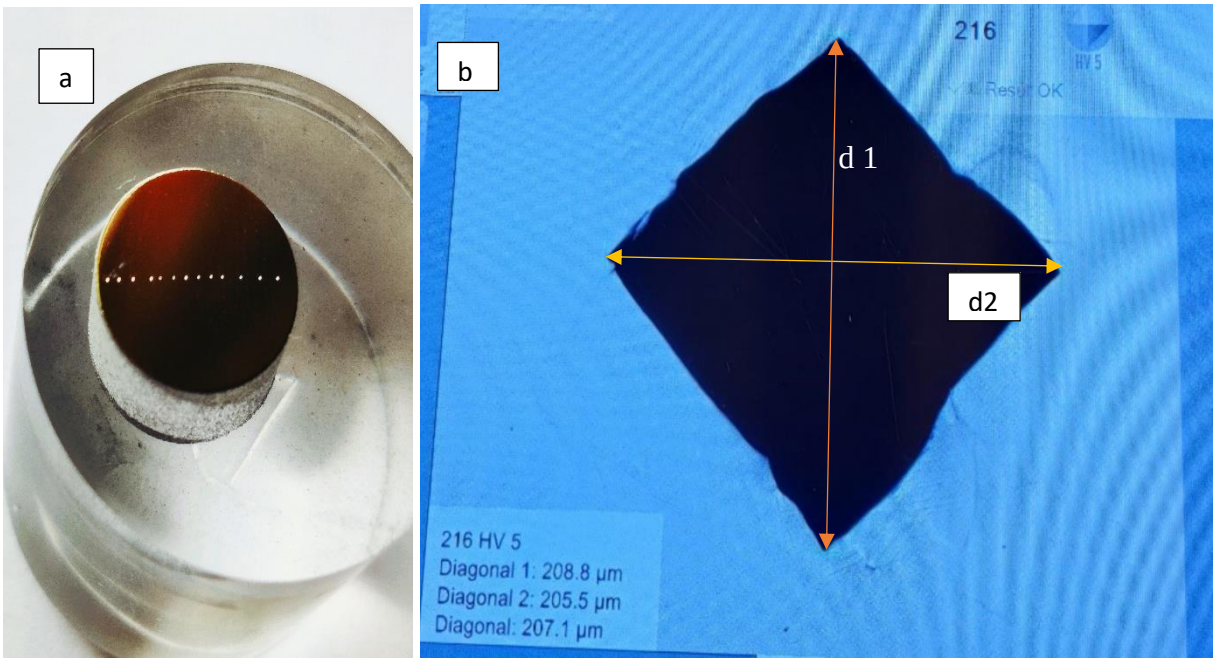

Figure 41: Indentation after load applied, (a) indentations on the surface after test, and (b) indentation on-screen on measuring mode.

Figure 41(b) shows the measurement of diagonals of indentation optically, then provides the hardness value. d1 and d2 are the diagonal indentation length measured optically. The hardness values for several indentations were collected and presented in table 5.

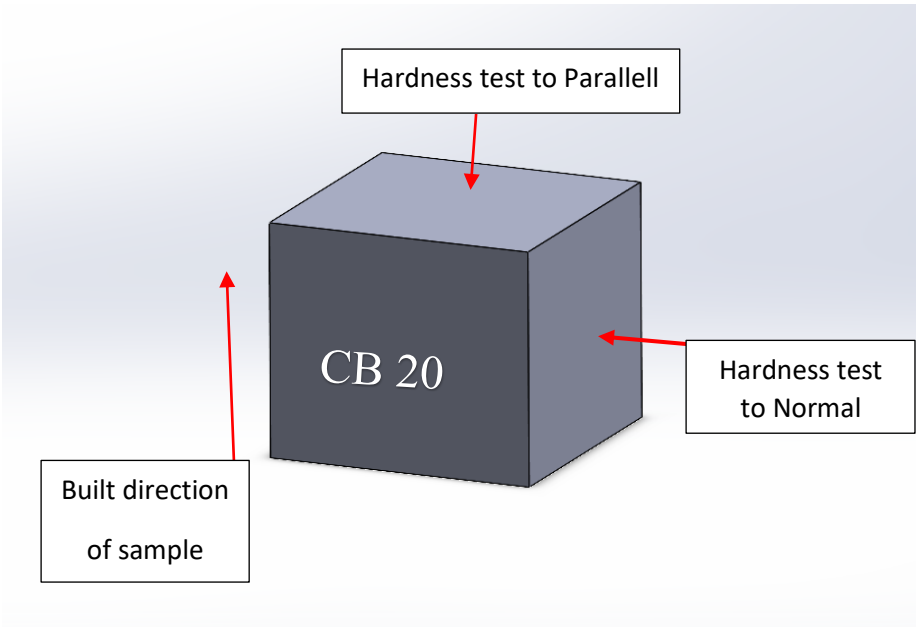

Figure 42: Representation of hardness indentation from different direction build direction

Indentation Number	Parallel to the building direction At height 20 mm	Parallel to the built direction At height 10 mm	Normal to the build direction	Parallel to the direction at height 110 mm
1	216	218	230	208
2	222	223	226	215
3	213	226	233	216
4	214	231	224	215
5	214	226	223	203
6	211	234	231	211
7	212	223	238	207
8	210	222	232	210
9	208	223	227	220
10	206	218	231	220
Average	212.6	224.4	229.5	212.5
St. deviation	4.45	5.10	4.31	5.64

Table 5: Hardness test(V-Charpy) result of 316L stainless steel

The results revealed variations in hardness values for the same Sample from direction and height. The standard deviation in all samples was found 4.31 to 5.64. Average hardness values in parallel at the height of 10mm, 20mm, and 110mm from supporting plate were found 224.4HV, 212.6 HV, and 212.5 respectively. In contrast, the Hardness value from normal to build direction is more significant than parallel that is 229.5HV at room temperature.

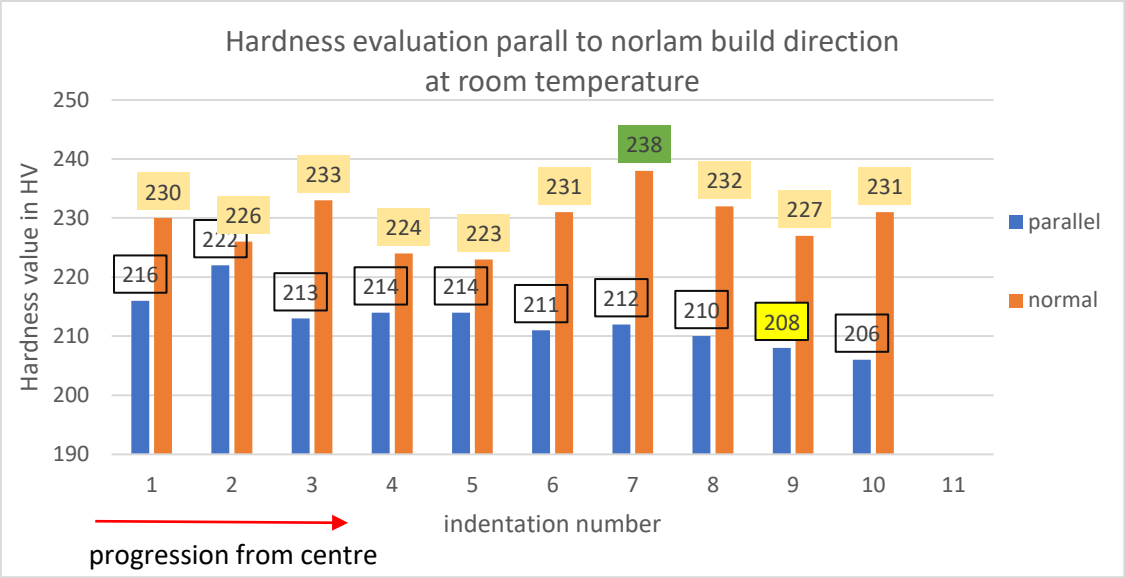

Figure 43: Hardness evaluation for parallel vs. normal to the built direction

Building direction has a vital role in the microstructure of the 316L printed by the SLM process, which determines the mechanical properties. From graph (figure 43), It is observed that the hardness values from the side of the Sample that is normal to the build direction are more significant compared to the parallel. The highest maximum hardness value (238 HV) was found in the normal direction whereas, the minimum (208 HV) hardness in parallel. Surface-normal and surface-parallel are supposed to have different anisotropy, and grain morphology from the optical microscope in figure 35 displays the difference of grain morphology of the two surfaces for the specimens.

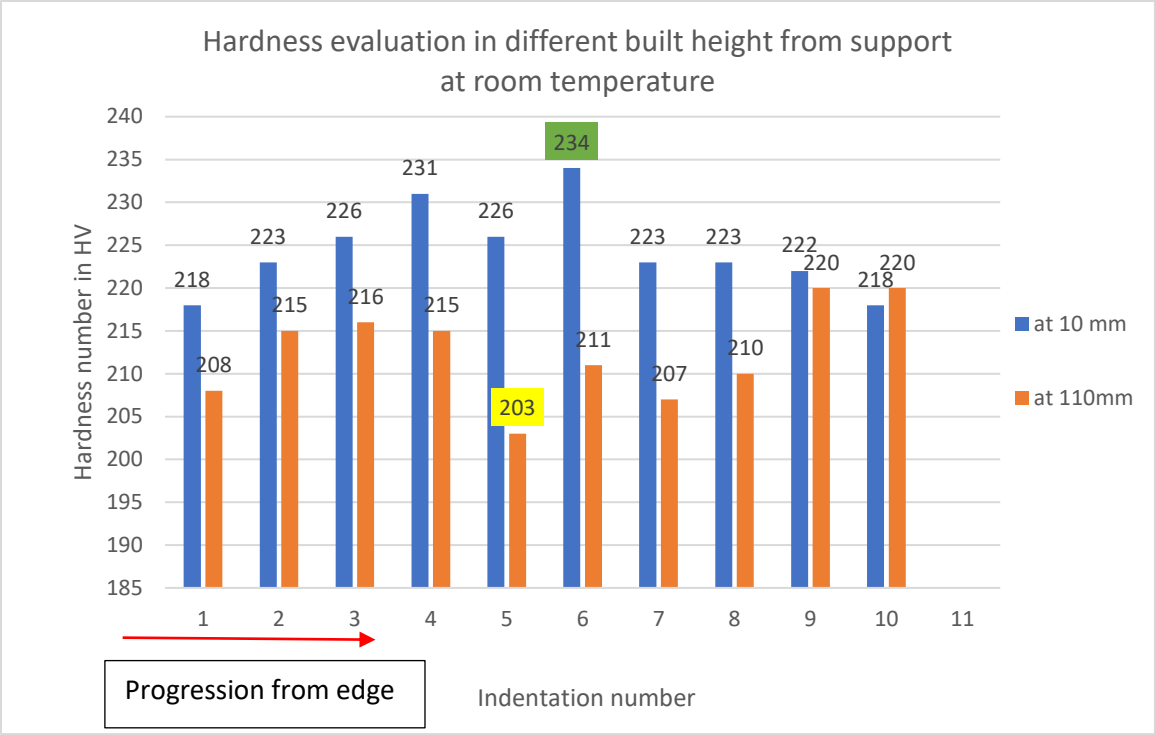

Figure 44: Hardness evaluation based on built height at 10mm vs. 110mm

Besides other process parameters, the building height was also an essential factor in the SLM processing of 316L(figure 44). Where the effects over the building height are observed in this study, therefore, it is not surprising to get results pointing out similar grain sizes for 316 L [73] and similar melt pool geometries over the entire build height. This is undoubtedly true, for the objects of the chosen geometry do not consist of enough layers to show any effect or long enough for sufficient cooling down between subsequent layers. The heat accumulation overbuild height plays an important role in defect formation, melt pool geometry, and hardness. However, its effect can be easily overlooked or under-estimated, but underestimation might be harmful in the case of large real part applications. Specific temperature regions are prone to onset precipitations, depletions by element segregation, or phase separation without build height effect.

6.4 Tensile Test Results And Discussion

The tensile tests for twelve samples were performed in accordance with ASTM E8, Standard at room temperature. 3D printed 316L specimens were prepared according to the standard Sample is placed in the testing machine, and load is applied. Extensometer was used to measure the elongation. Information about the strength, stiffness, and ductility of a material

can be obtained from a tensile test. The representative load/extension curves of the produced tensile specimens in the horizontal and vertical buildup directions are represented in figures, and the corresponding values are listed in the Tables below.

Specimens	**Yield strength 0.2% (MPa)**	**Tensile strength (MPa)**	**Extension at break (mm)**
Top A	481.9	579.5	22.005
Buttom A	482.6	589.5	17.554
Top B	487.2	579.5	25.503
Buttom B	485.1	590.1	23.068
Top C	480.4	561.8	25.056
Buttom C	488.1	574.2	25.648
Top D	485.4	558.7	25.811
Buttom D	493.4	575	18.75
Top E	480.7	567.6	25.401
Buttom E	491.6	580.7	19.048
XX(X-direction)	558.9	663	19.458
YY(Y-direction)	582.2	674.7	20.118

Z-direction

Table 6: Yield strength, Tensile strength, and extension at break of tested samples

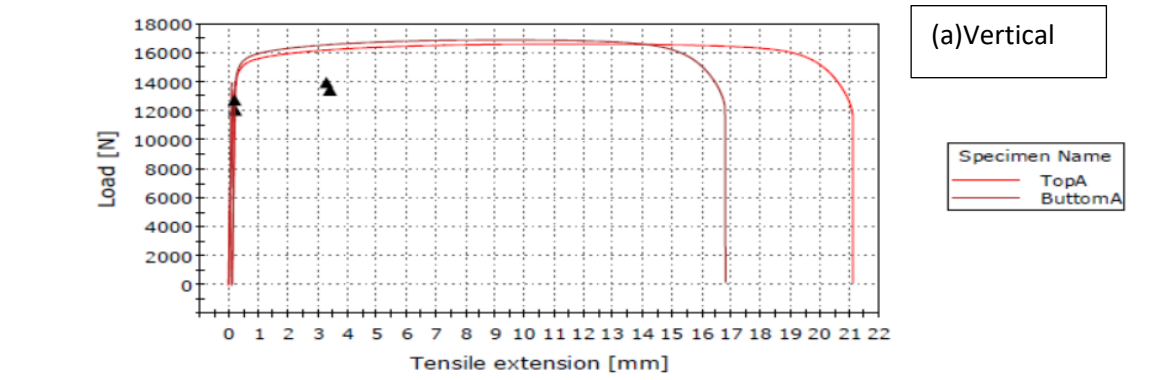

	Rp0.2% [MPa]	Rm [MPa]	Extension at Break (Standard) [mm]
1	481.9	579.5	22.00541
2	482.6	589.5	17.55498

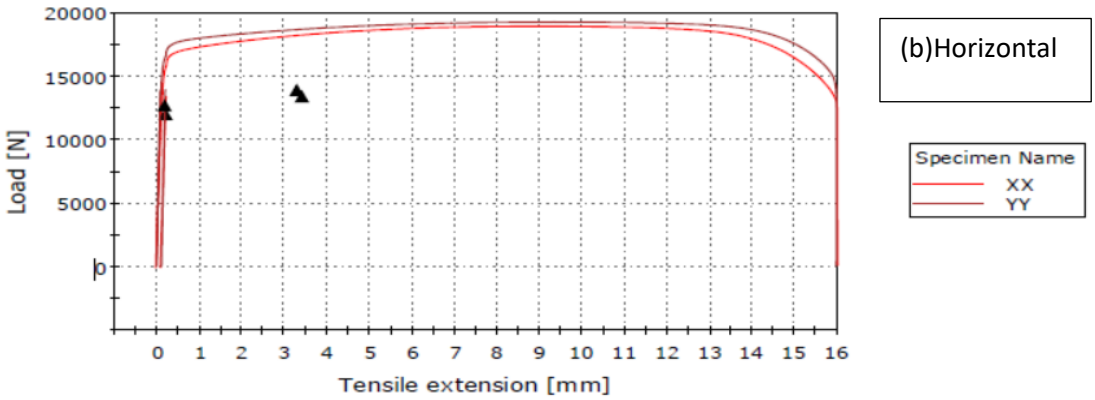

	Rp0.2% [MPa]	Rm [MPa]	Extension at Break (Standard) [mm]
1	558.9	663.0	19.45859
2	582.2	674.7	20.11825

Figure 45: Load vs. extension curve(a) built in vertical direction, (b) built in horizontal direction

Figure 45 shows the load versus extension curve of the sample built-in horizontal direction and vertical direction. From the curve, it is noticed that the plastic deformation starts from nearly at stress 481 MPa in the vertical direction built, whereas in the horizontal direction, it is 558Mpa above. This value determines that Yield strength in horizontal direction samples have more. Similarly, tensile strength in X and Y- directions built possess higher value (above 663 MPa), in contrast in a vertical direction they have (nearly 580MPa)

Yield Strength (σ_{YS}):

Yield strength is the stress that causes permanent deformation of 0.2% of the original dimension; this is not a sharply defined point. The point in the stress strain curve at which

material exceeds the elastic limit will not return to its original shape or size even when the load is removed. This can be determined by evaluating a stress-strain diagram produced during a tensile test.

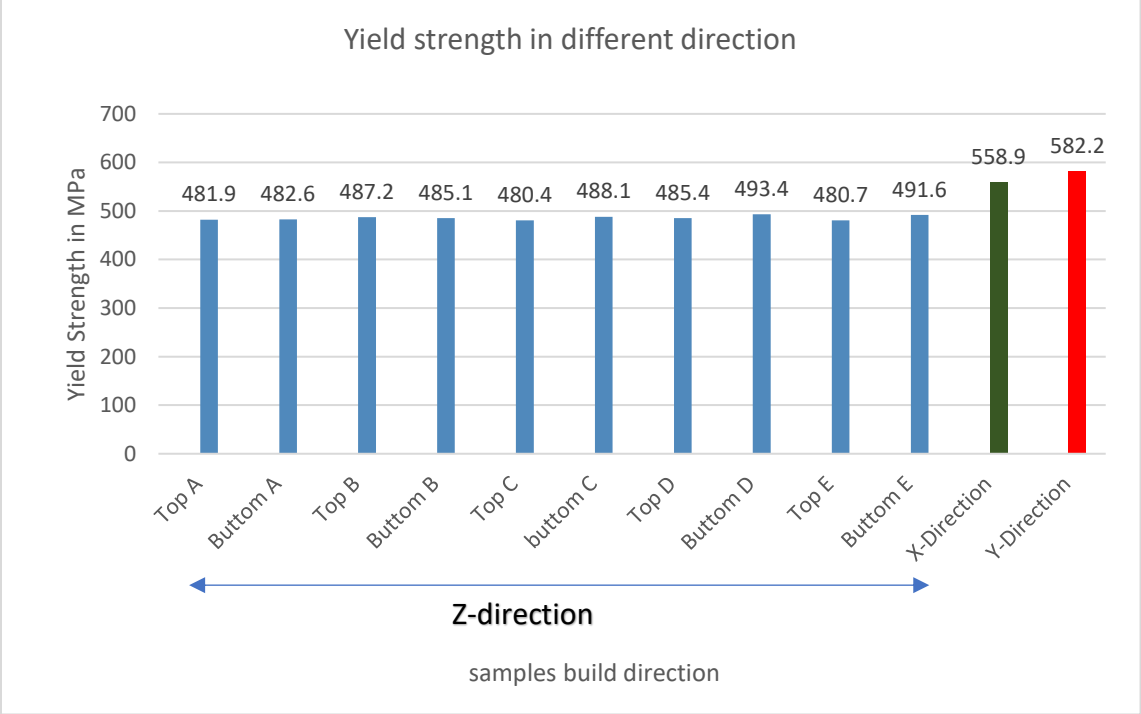

Figure 46: Yield strength of 316L processed in a different direction

There is a difference in yield strength for the samples printed in different directions, as shown in the graph (Figure 46). The yield strength in Sample built-in vertical direction possesses a superior value of 582.2 MPa in the Y direction and 558.9 MPa in the X-direction. In contrast, the Sample's built-in Z-directions (vertically) have minimum values. The least value of Yield strength was found 480.4 MPa for sample top C, which is even greater than the given criteria 205 Mpa.

Ultimate Tensile Strength, (σ_{TS}):

Beyond yielding, continuous loading leads to an increase in the stress required to permanently deform the specimen, as we can in the stress-strain curve. At this stage, the specimen is strain hardened or work hardened. If the load is continuously applied, the stress-strain curve will reach the maximum point, which is the ultimate tensile strength (UTS, σTS). At this point, the specimen can withstand the highest stress before necking takes place.

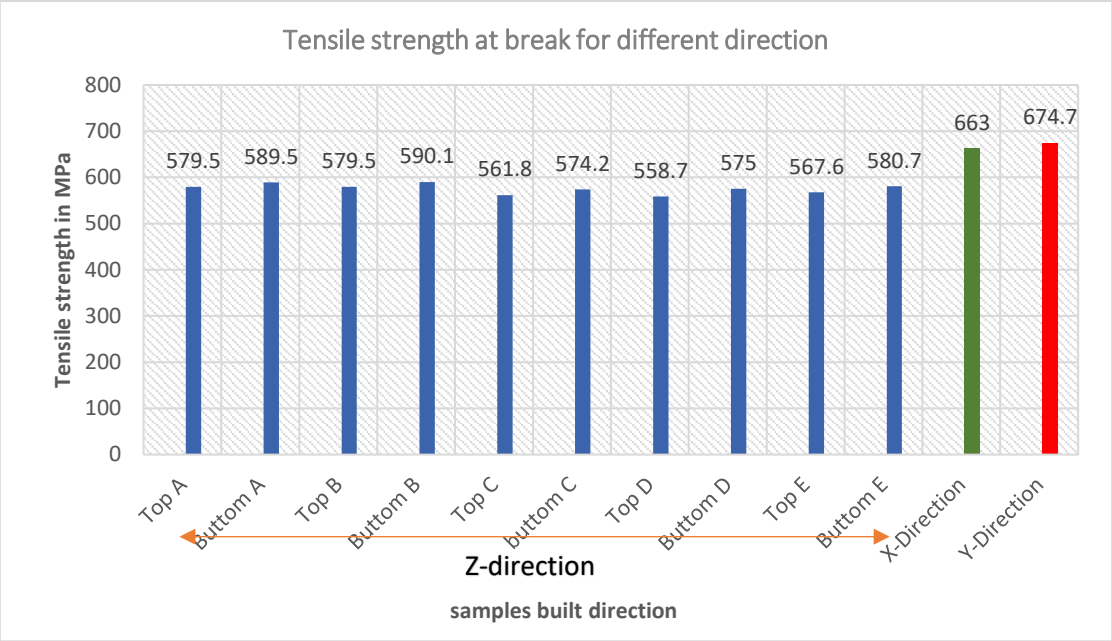

Figure 47: Tensile strength of samples built in different directions

Similar to the yield strength of as printed 316L sample has a greater tensile strength in horizontal built direction than the printed in the vertical direction(figure 47). The minimum value of 558.7 MPa was found in the constructed Sample (top D) vertically; in contrast, the maximum value was found in the Sample made in the Y direction. As per, the criteria given was a minimum of 515 MPa, which is satisfied as the minimum result value is relatively more significant than the acceptance criteria. The tensile test result shows that the samples built in the X, Y direction recorded the highest values of UTS, meaning that there is a larger area under the stress-strain curve, i.e., the material absorbs more energy before failure.

Elongation:

Elongation is the stretch from the original length of the specimen to the point of failure. The % elongation of a specimen undergoes during tensile testing can be calculated using the equation.

$$\% \text{ elongation } \frac{\Delta L}{Lo} * 100 \quad \text{equation 7.}$$

Where ΔL extension at the break.

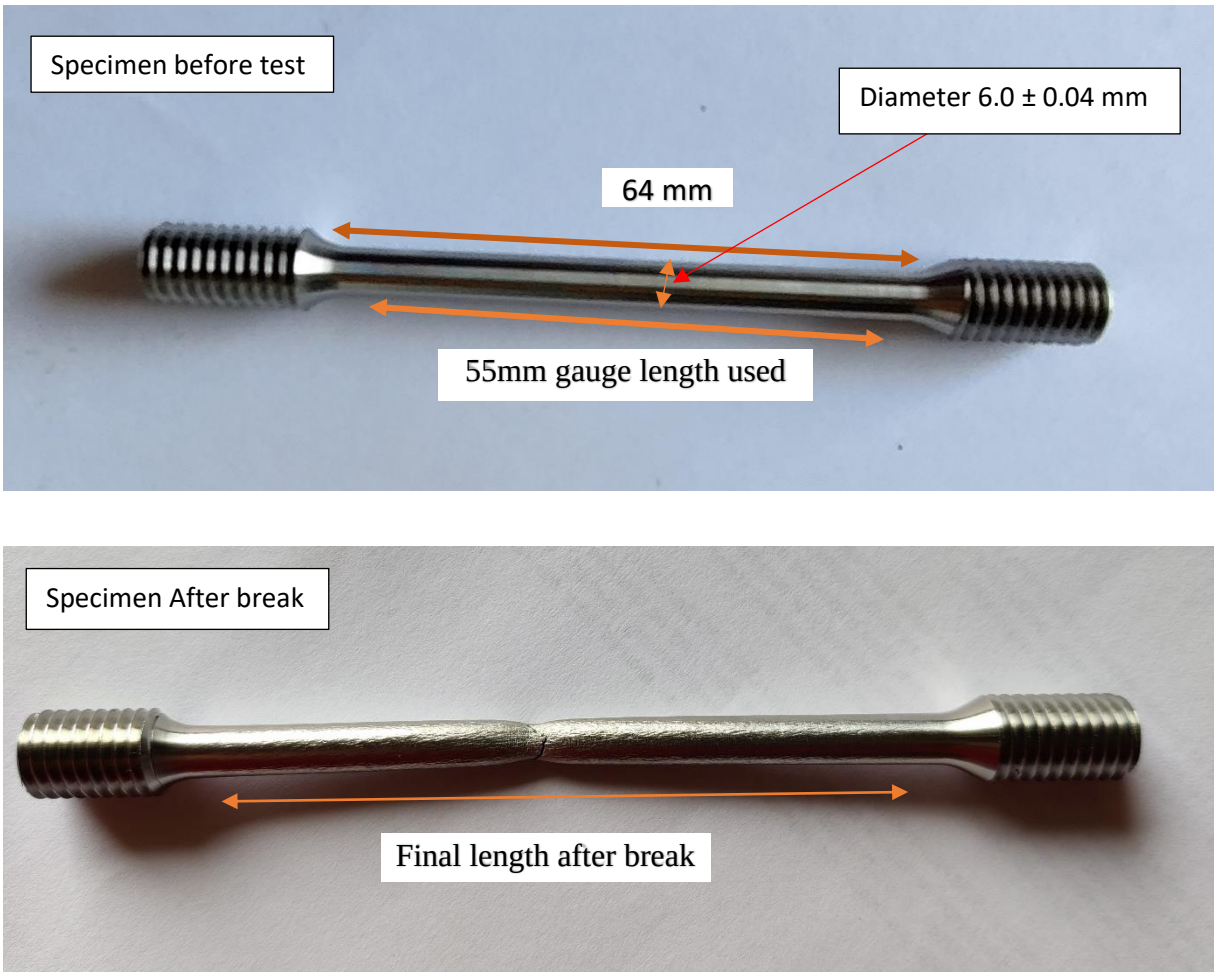

Figure 48: tensile specimen before and after the test

The extension measured by extensometer and calculated %elongation of specimens using formula (equation) is presented in table 7.

Specimens	Elongation (mm)	% elongation
Top A	22.005	40.01
Bottom A	17.554	31.91
Top B	25.503	46.36
Bottom B	23.068	41.94
Top C	25.056	45.55
Bottom C	25.648	46.63
Top D	25.811	46.92
Bottom D	18.75	34.09
Top E	25.401	46.18
Bottom E	19.048	34.63
XX	19.458	35.37
YY	20.118	36.57

Table 7: Extension and calculated % elongation of samples

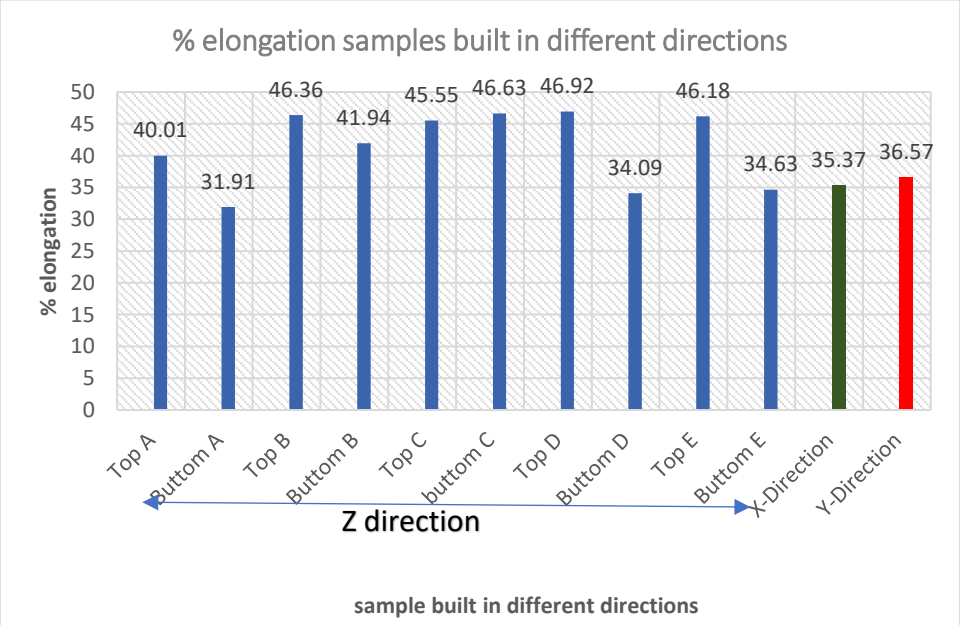

Figure 49: graph of elongation vs. Sample built directions

In general, the elongation of sample build in Z direction has more compare to build in horizontal(X and Y directions), is noticed in figure 49. The minimum elongation was found at 31.91% for the sample bottom that was built vertically. The acceptance criteria were given a

minimum of 30%. The result minimum value is more significant than the given criteria; therefore, it seems acceptable. However, the most outstanding value was found for the Sample for top D, which was also built vertically at a different position.

% Reduction in Area :

Reduction in the Area is a ductility measurement, Which is the difference between an original given cross-sectional area of a test specimen before being subjected to tension and the given area of its smallest cross-section after rupturing. % Reduction in Area $=\frac{\Delta A}{A0} * 100$ equation

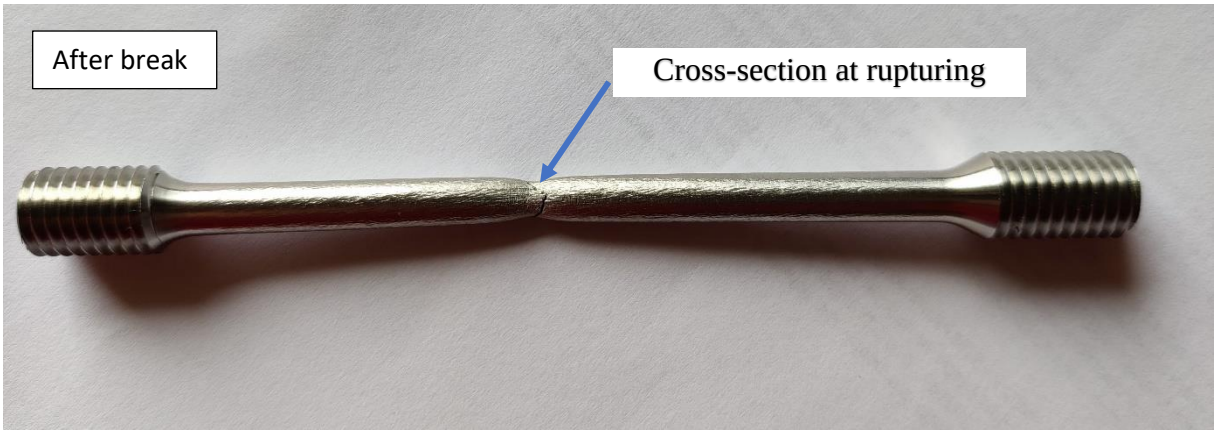

Figure 50. Sample after break showing cross-section at rupturing

Specimens	Original diameter (mm)	Diameter after break (mm)	% Reduction in area
Top A	6.04	3.72	48.728
Bottom A	6.04	3.63	50.152
Top B	6.04	3.51	51.996
Bottom B	6.04	3.30	55.073
Top C	6.03	3.52	51.752
Bottom C	6.04	3.58	50.928
Top D	6.02	3.51	56.576
Bottom D	6.03	3.65	49.740
Top E	6.03	3.55	51.294
Bottom E	6.04	3.51	51.996
XX	6.03	3.39	53.518
YY	6.04	3.46	52.746

Table 8: Original, final diameter, and calculated % reduction in area

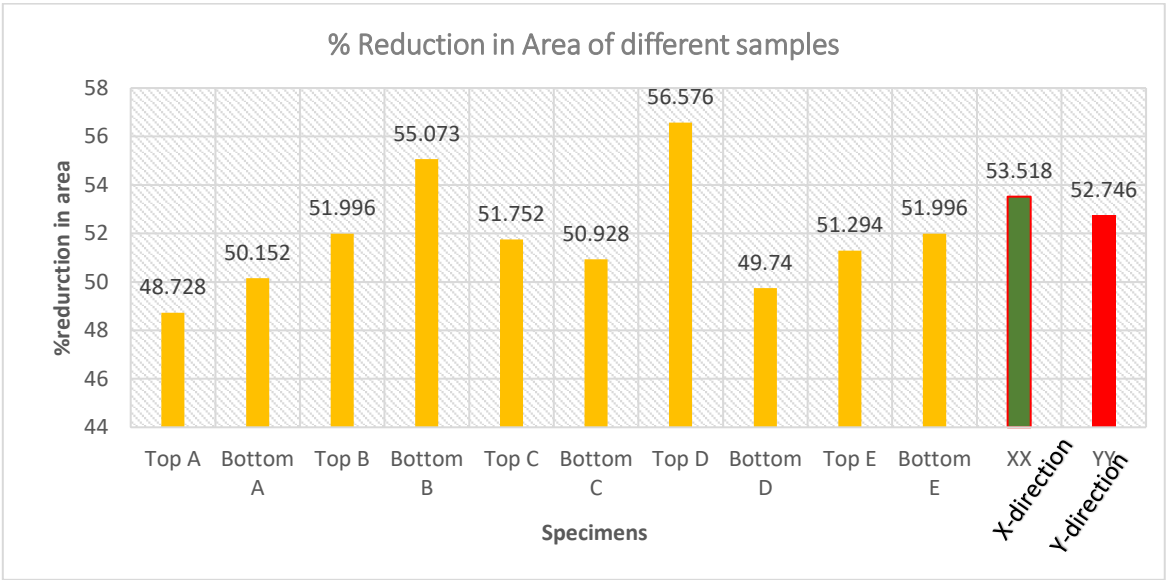

Figure 51: Diagram plot for %reduction area for Sample in different directions.

Figure 51 shows that variation in % reduction area is not a clear difference in respect of building direction. The least % reduction was found 48.72 for the Sample build vertically built(top A), whereas the most significant value was found in sample top D, which was also built vertically. The material is acceptable because the least value is greater than the given criteria (minimum of 30%).

The SLM samples were not heat-treated to evaluate the influence of the orientation and consequently the anisotropic behavior. The overall result for yield strength and the tensile strength of as printed 316L by SLM process specimens is higher in the horizontal buildup direction than in the vertical buildup direction. This is due to the orientation of the layers, the effect of binding defects, and force transmission within the specimen during tensile testing. In the case of vertical buildup, the force is transmitted normally to the layered material; therefore, binding defects influence the force transmission. Pores or defects generate internal stress concentrations and arise premature failure. In contrast, binding defects neither drastically reduce the load-bearing cross-section of the specimen nor does force transmission occur via these structural defects in the case of specimens built up horizontally[48].

6.5 V-Charpy test result and Discussion

Impact property is considered one of the fundamental properties for investing the 3D printed stainless steel quality. The selection and optimization of the processing parameters play an important role in getting a better impact property of the 3D printed 316L. The Charpy impact toughness test was carried out at room temperature for all nine specimens received. Figure 22 represents the fracture surface of specimen ZZ1, and other images are available in appendix 1 after the V-Charpy impact test. All the impact energy test result from the test using the Zwick Roel Charpy test machine following ASTM E23 is illustrated in table 9.

Table:

specimens	XX1	XX2	XX3	YY1	YY2	YY3	ZZ1	ZZ2	ZZ3	St.d
Impact Energy J	128.3	128.4	127.7	118.6	120	113.6 min	144.8	124.3	147.3 max	11.76

Table 9: Impact energy (V-Charpy) test results of 316L samples

The collected data has a variation in impact energy value form on each other; therefore, standard deviation from mean value was calculated and found 11.76, and the average is 130.388J from readings for all the samples were tested. Kongsberg had given the acceptance criteria a minimum of 103J, and the experimental value is relatively better than the requirement that is 113.6 J, from sample YY3. In contrast, the maximum impact was obtained from sample ZZ3.

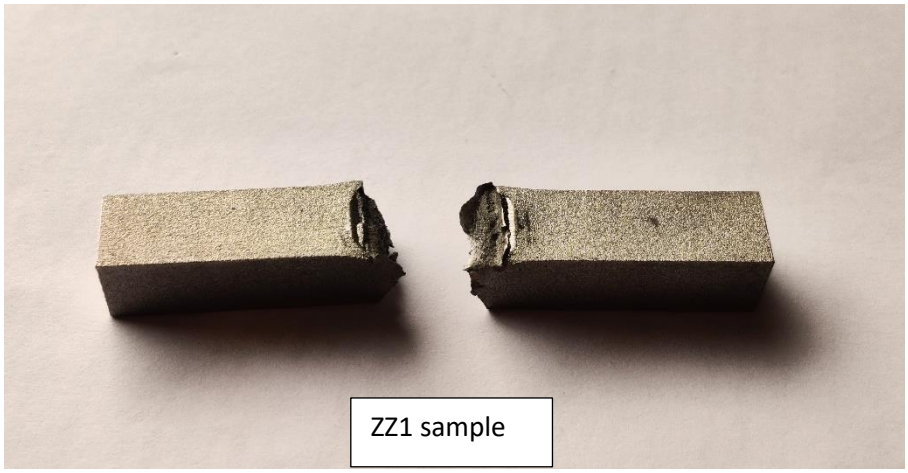

Figure 52: 3D printed 316L Sample after a fracture

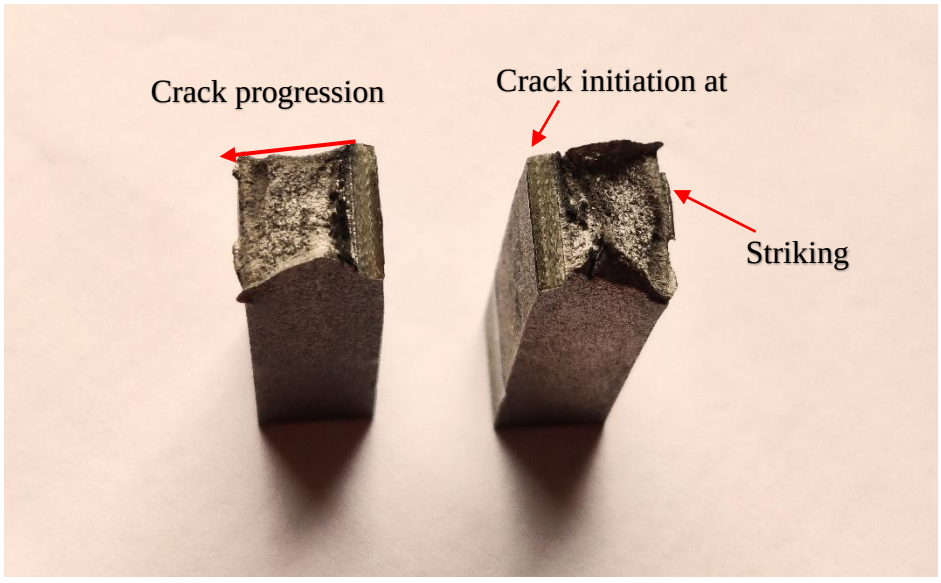

Figure 53: the face of the fractured Sample after rupturing of Sample ZZ1

As we can see(figure 53), the smooth fracture surface morphology where the crack starts from the tip of the notch and propagates down properly to the striking face. This type of fracture resembles the characteristics of the ductile fracture of steel.

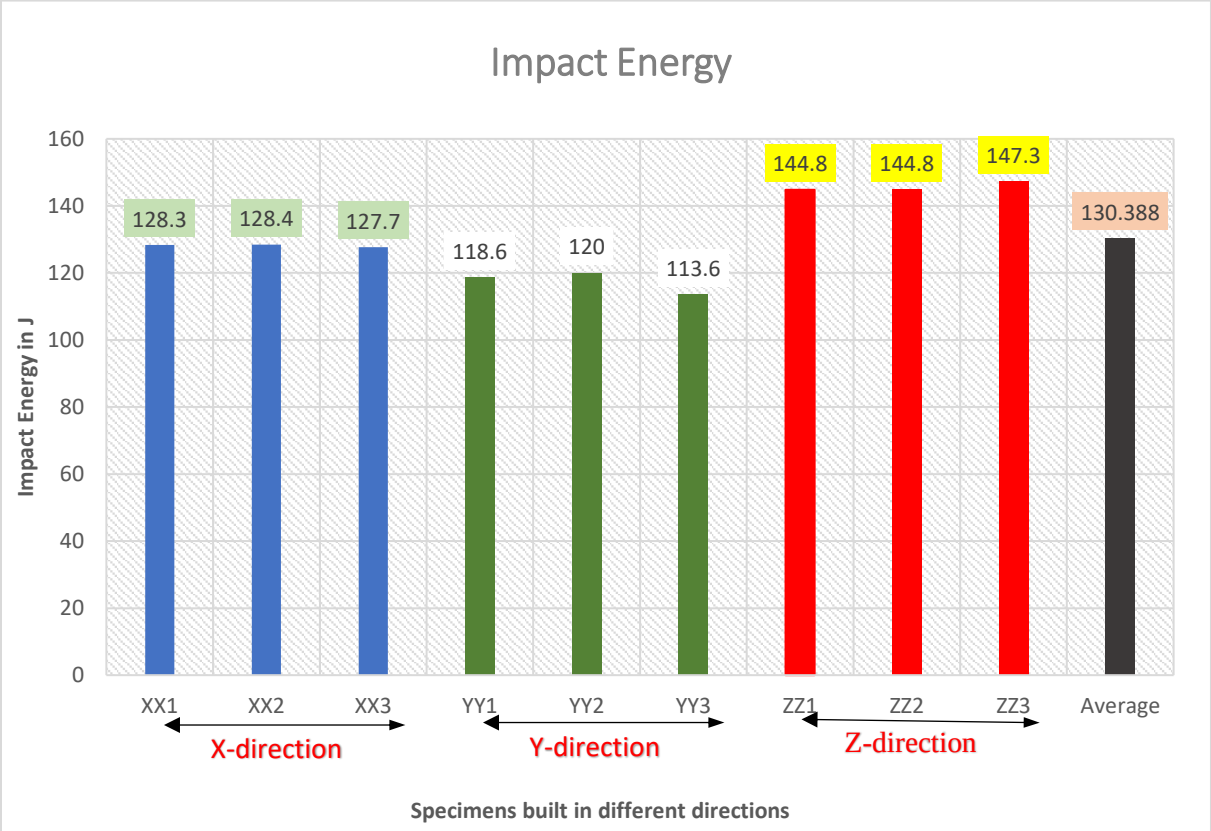

Figure 54: 2d graph plot for the result of different samples

The mechanical properties of as-printed materials are mainly due to the stresses generated in crystal defects, including grain boundaries and dislocation networks. From the graph, the specimens built up in z-direction have a superior impact energy value. It signifies that they have more toughness value than the other direction. The differences in the fracture toughness values obtained in this study with different build directions were anticipated by the previous investigation of the microstructure analysis. These tested values enhance the fracture toughness of parts built in the Z-direction because of the fast cooling rate and the resulting dendritic grain structure. On the other hand, parts built in the X and Y directions show lower fracture toughness values(figure 54) than those made in the z-direction because of the larger pores and defects, especially in the samples built in the x-direction were subjected to loading perpendicular to the build direction. The results graph reveals that the build orientation has a strong effect upon properties. For example, fracture toughness was smallest in the samples built in the Y direction; it is maybe because of the pores, voids, and cracks present at the edge of the parts. In summary, toughness is the ability of a metal to deform plastically and absorb energy before rupture. And the acceptable impact energy value was given a minimum of 103

J. From the results of the table, the minimum value was obtained, 113.6J. Therefore it can be concluded that the obtained results are acceptable.

6.6 Further Investigation

- Since the specimens under experiments are as-printed, not heat treated, the improvement in a 316L can be made by heat treatment using optimized standard procedure.
- The behavior of metal under the impact load at different temperatures and the fractured surface can be studied using an SEM machine. Moreover, fracture studies can be done using U-notch, also following ASTM E23standard.
- Analysis of the SLM 316L Stainless Steel parts' corrosion resistance as it is exposed to a corrosive environment.

CHAPTER 7: CONCLUSION

Experimental analyses have been carried out to investigate the microstructure and relation between laser building orientation and mechanical properties of SLM 316L. The powder metal was manufactured using gas atomization and manufactured with standard parameters of EOS M290, using layer thickness of 40µm. For the investigation, samples were printed in three different directions so we could compare the results. To sum up, from the micrographic inspection and results from the Mechanical experiments, the properties of SLM 316L can be concluded.

- The variation of microstructures observed; Cellular structure is predominantly present. In this study, samples printed in different directions vary due to the orientation of grains; however, the process parameters predominantly affect the microstructure and material properties. The thermal energy induced by the melting of subsequent layers is significant because the microstructure and properties of SLM-built materials depend on the solidification rate. And, the heat flux influences the growth direction of the grains, resulting in grain growth perpendicular to the previously applied layers.
- Porosity: spherical porosity is predominantly seen so that it can be considered the most of the porosity due to entrapped gas while manufacturing the metallic powder. However, a minority of the pore have irregular in nature; therefore, entrapment of porosity during manufacturing also occurred but very little. Thus, the selective laser melting technique could produce solid components fully dense greater than 98%.
- Hardness evaluation concluded that the toughness of the sample surface is higher in normal to the scan direction than the parallel, Relationship between building height and hardness. As the height is increased from the building platform, the hardness value is decreased.
- The mechanical behavior of SLM samples was comparable or superior to that of the reference material and was mainly influenced by the building orientation. It is concluded that the mechanical properties of 316L stainless steel are dependent on building direction. The sample printed in X and Y(horizontally) directions possesses superior tensile and Yield strength than printed in Z-direction(vertically).
- The sample built horizontally has more impact energy value, representing more ductile compared to constructed vertically. The tensile and V-Charpy fracture was ductile in nature, however few some location shows brittle rupturing.

CHAPTER 8: REFERENCES

[1] LOPES, Gonçalo Teixeira Ferreira. Exploração das possibilidades da impressão 2D na construção. 2015-2016. 92 f. Dissertação (Mestrado em Engenharia Civil) – Faculdade de Engenharia, Universidade do Porto, Porto, 2016.

[2] ABREU, Sofia Alexandra Chaves. Impressão 3D Baixo Custo Versus Impressão em Equipamentos de Elevado Custo. 2015. 235 p. 2015. Dissertação (Mestrado Integrado em Engenharia Mecânica), Faculdade de Engenharia, Universidade do Porto, 2015.

[3] B. Song, S. Dong, B. Zhang, H. Liao, C. Coddet, Mater. Des. 35 (2012) 120–125.

[4] K. Guan, Z.Wang, M. Gao, X. Li, X. Zeng, Mater. Des. 50 (2013) 581–586.

[5] Li, H., Liu, Y., Liu, Y. et al. Effect of sintering temperature in argon atmosphere on microstructure and properties of 3D printed alumina ceramic cores. J Adv Ceram 9, 220–231 (2020). https://doi.org/10.1007/s40145-020-0362-0

[6] ASM Metals Handbook, vol. 1, Selection of Irons, Steels and High Performance

Alloys, ASM International, 2005.

[7] Wohlers Report 2014, 3D Printing and Additive Manufacturing State of the

Industry AnnualWorldwide Progress Report, ISBN 978-0-9913332-0-2.

[8] N. Read,W.Wang, K. Essa, M.M. Attallah, Mater. Des. 65 (2015) 417–424.

[9] ASTM, "Standard Terminology for Additive Manufacturing - General Principles - Terminology," in ISO/ASTM 52900, ed. West Conshohocken, PA, 2015.

[10] B. Song, S. Dong, B. Zhang, H. Liao, C. Coddet, Mater. Des. 35 (2012) 120–125.

[11] Y.M. Arısoy, L.E. Criales, T. Özel, B. Lane, S. Moylan, A. Donmez, Influence of

scan strategy and process parameters on microstructure and its optimization in additively manufactured nickel alloy 625 via laser powder bed fusion, Int. J. Adv. Manuf. Technol. (2017),

[12] T. DebRoy, H.L. Wei, J.S. Zuback, T. Mukherjee, J.W. Elmer, J.O. Milewski, A.M.

Beese, A. Wilson-Heid, A. De, W. Zhang, Additive manufacturing of metallic components – process, structure and properties, Prog. Mater. Sci. (2018),

[13] W. King, A.T. Anderson, R.M. Ferencz, N.E. Hodge, C. Kamath, S.A. Khairallah,

Overview of modelling and simulation of metal powder bed fusion process at Lawrence Livermore National Laboratory, Mater. Sci. Technol. (United Kingdom). (2015),

[14] Melia, M.A., Duran, J.G., Koepke, J.R. et al. How build angle and post-processing impact roughness and corrosion of additively manufactured 316L stainless steel. npj Mater Degrad 4, 21 (2020). https://doi.org/10.1038/s41529-020-00126-5

[15] X.Y. Cheng, S.J. Li, L.E. Murr, Z.B. Zhang, Y.L. Hao, R. Yang, F. Medina, R.B. Wicker, Compression deformation behavior of Ti–6Al–4V alloy with cellular structures fabricated by electron beam melting, Journal of the Mechanical Behavior of Biomedical Materials, volume 16, 2012, Pages 153-162, ISSN 1751-6161,

[16] Atsushi akaichi, Yuka Kajima, Nuttaphon Kittikundecha, Hein Linn Htat, Hla Htoot Wai Cho, Takao Hanawa, Takayuki Yoneyama, Noriyuki Wakabayashi, Effect of heat treatment on the anisotropic microstructural and mechanical properties of Co–Cr–Mo alloys produced by selective laser melting, Journal of the Mechanical Behavior of Biomedical Materials, Volume 102, 2020, 103496, ISSN 1751-6161,

[17] M. Yakout, A. Cadamuro, M. A. Elbestawi, and S. C. Veldhuis, "The selection of process parameters in additive manufacturing for aerospace alloys," International Journal of Advanced Manufacturing Technology, vol. 92, pp. 2081-2098, September 01 2017.

[18] M. Yakout, M. A. Elbestawi, and S. C. Veldhuis, "On the characterization of stainless steel 316L parts produced by selective laser melting," International Journal of Advanced

Manufacturing Technology, vol. Online First, pp. 1-22, 2017.

[19] Liu, Y.J., Li, S.J., Wang, H.L., et al., 2016b. Microstructure, defects and mechanical behavior of beta-type titanium porous structures manufactured by electron beam melting and selective laser melting. Acta Mater. 113, 56–67. Copyright (2016), Elsevier.

[20] Michaela Fousová, Dalibor Vojtěch, Jiří Kubásek, Eva Jablonská, Jaroslav Fojt,

Promising characteristics of gradient porosity Ti-6Al-4V alloy prepared by SLM process,

Journal of the Mechanical Behavior of Biomedical Materials, Volume 69, 2017, Pages 368-376, ISSN 1751-6161,

[21] Li, Ruidi, et al. “Densification Behavior of Gas and Water Atomized 316L Stainless Steel Powder during Selective Laser Melting.” Applied Surface Science, vol. 256, no. 13, 2010, pp. 4350–4356., doi:10.1016/j.apsusc.2010.02.030.

[22] Kamath, Chandrika, et al. “Density of Additively-Manufactured, 316L SS Parts Using LaserPowder-Bed Fusion at Powers Up to 400W.” Metallurgical and Materials Transactions A,vol. 45A, Dec. 2014, pp. 6260–6270., doi:10.2172/1116929.

[23] H. Attar, M. Calin, L.C. Zhang, S. Scudino, J. Eckert, Manufacture by selective laser melting and mechanical behavior of commercially pure titanium, Materials Science and Engineering: A, Volume 593, 2014, Pages 170-177, ISSN 0921-5093,

[24] Pan Wang, Pengfei Huang, Fern Lan Ng, Wai Jack Sin, Shenglu Lu, Mui Ling Sharon Nai, ZhiLi Dong, Jun Wei, dditively manufactured CoCrFeNiMn high-entropy alloy via pre-alloyed powder, Materials & Design, Volume 168, 2019, 107576, ISSN 0264-1275,

[25] J.-P. Kruth, M. Badrossamay, E. Yasa, J. Deckers, L. Thijs, J. Van Humbeeck, “Part

and Material Properties in Selective Laser Melting of Metals”, 16th International Symposium on Electromachining, Shanghai Jiao Tong University Press, 2010, Shanghai, China.

[26] S. Das, Adv. Eng. Mater. 5 (2003) 701–711.

[27] S.A. Khairallah, A.T. Anderson, A. Rubenchik,W.E. King, Acta Mater. 108 (2016) 36–45.

[28] M. Yakout, M. A. Elbestawi, and S. C. Veldhuis, "On the characterization of stainless steel 316L parts produced by selective laser melting," International Journal of Advanced

Manufacturing Technology, vol. Online First, pp. 1-22, 2017.

[29] J. A. Cherry, H. M. Davies, S. Mehmood, N. P. Lavery, S. G. R. Brown, and J. Sienz,

"Investigation into the Effect of Process Parameters on Microstructural and Physical Properties

of 316L Stainless Steel Parts by Selective Laser Melting.," International Journal of Advanced

Manufacturing Technology, vol. 76, pp. 869-879, 2015.

[30] J. Delgado, J. Ciurana, and C. A. Rodríguez, "Influence of Process Parameters on Part Quality and Mechanical Properties for DMLS and SLM with Iron-Based Materials," International Journal of Advanced Manufacturing Technology, vol. 60, pp. 601-610, 2012.

[31] F. Miller, "Schneller Zahn aus Titan (Fast Tooth made of Titanium)," Fraunhofer Magazin, vol.4, 2002.

[32] C. Over, W. Meiners, K. Wissenbach, M. Lindemann, and G. Hammann, "Selective LasernMelting: A New Approach for the Direct Manufacturing of Metal Parts and Tools," in

International Conference on Laser Assisted Net Shape Engineering, Furth, Germany, 2001.

[33] A. B. Spierings and G. Levy, "Comparison of Density of Stainless Steel 316L Parts Produced with Selective Laser Melting using Different Powder Grades," in International Solid Freeform Fabrication Symposium, USA, 2009, pp. 342-353.

[34] A. B. Spierings, N. Herres, and G. Levy, "Influence of the Particle Size Distribution on Surface Quality and Mechanical Properties in Additive Manufactured Stainless Steel Parts," in International Solid Freeform Fabrication Symposium, USA, 2010, pp. 397-406.

[35] Outokumpu, Handbook of Stainless Steel, 2013. [33] M.McGuire, Stainless Steels For Design Engineers, n.d. doi:10.1361/ssde2008p090.

[36] H.K.D.H. Bhadeshia, S.R. Honeycombe, Stainless Steel, in: Steels, Elsevier, 2006: pp. 259– 286. doi:10.1016/B978-075068084-4/50014-5.

[37] H. K. D. H. Bhadeshia and R. W. K. Honeycombe, Steels : microstructure and properties, 3rd ed. ed. Amsterdam: Elsevier, 2006.

[38] D. D. Gu, W. Meiners, K. Wissenbach, and R. Poprawe, "Laser additive manufacturing of metallic components: materials, processes and mechanisms," International Materials Reviews, vol. 57, pp. 133-164, 2012/05/01 2012.

[39] N. A. Kistler, "Characterization of Inconel 718 Fabricated through Powder Bed Fusion

Additive Manufacturing," B.Sc. Thesis, Materials Science and Engineering, Pennsylvania State University, USA, 2015.

[40] W. E. Frazier, "Metal Additive Manufacturing: A Review," Journal of Materials Engineering and Performance, vol. 23, pp. 1917-1928, 2014.

[41] X. Gong and K. Chou, "Microstructures of Inconel 718 by Slective Laser Melting," in TMS 2015 Annual Meeting Supplemental Proceedings, Orlando, Florida, USA, 2015, pp. 461-468.

[42] H. Y. Song, "Multi-Scale Microstructure Characterization for Improved Understanding of Microstructure-Property Relationship in Additive Manufacturing " PhD, Welding Engineering, Ohio State University, Ohio, USA, 2016.

[43] Wang D, Song C, Yang Y, Bai Y (2016) Investigation of crystal growth mechanism during selective laser melting and mechanical property characterization of 316L stainless steel parts. Mater Des 100:291–299

[44] Henning jgsbach F., Koppa P., Holzweissig M. J., et al.: Inline additively manufactured functionally graded multi-materials. Microstructure and mechanical characterization of 316L parts with H13 layers, Progress in Additive Manufacturing, (2018), pp. 1–9

[45] Zhong Y, Liu L, Wikman S, Cui D, Shen Z (2016) Intergranular cellular segregation network structure strengthening 316L stainless steel prepared by selective laser melting. J Nucl Mater 470:170–178

[46] Birnbaum AJ, Steuben JC, Barrick EJ, Iliopoulus AP, Michopoulos JG (2019) Intrinsic strain aging, Σ3 boundaries, and origins of cellular substructure in additively manufactured 316L. Additive Manufacturing 29:100784

[47] Boes J, Röttger A, Mutke C, Escher C, Theisen W (2018) Microstructure and mechanical properties of X65MoCrWV3-2 cold-work tool steel produced by selective laser melting. Additive Manufacturing 23:170–180

[48] . Ning J, Sievers DE, Garmestani H, Liang SY (2019) Analytical modeling of in-process temperature in powder bed additive manufacturing considering laser power absorption, latent heat, scanning strategy, and powder packing. Materials 12:808

[49] Ferrar B, Mullen L, Jones E, Stamp R, Sutcliffe CJ (2012) Gas flow effects on selective laser melting (SLM) manufacturing performance. J Mater Process Technol 212:355–364

[50] Ali U, Mahmoodkhani Y, Imani Shahabad S, Esmaeilizadeh R, Liravi F, Sheydaeian E, Huang KY, Marzbanrad E, Vlasea M, Toyserkani E (2018) On the measurement of relative powder-bed compaction density in powder-bed additive manufacturing processes. Mater Des 155:495–501

[51] Mahmoodkhani Y, Ali U, Imani Shahabad S, Rani Kasinathan A, Esmaeilizadeh R, Keshavarzkermani A, Marzbanrad E, Toyserkani E (2019) On the measurement of effective powder layer thickness in laser powder-bed fusion additive manufacturing of metals. Prog Addit Manuf 4:109–116

[52] Liverani E, Toschi S, Ceschni I, Fortnunato A (2017) Effect of selective laser melting (SLM) process parameters on microstructure and mechanical properties of 316L austenitic stainless steel. J Mater Process Technol 249:255–263

[53] R. Li, Y. Shi, Z. Wang, L. Wang, J. Liu, W. Jiang, Densification behavior of gas and

water atomized 316L stainless steel powder during selective laser melting, Appl. Surf. Sci. 256 (2010) 4350e4356.

[54] G. Sander, S. Thomas, V. Cruz, M. Jurg, N. Birbilis, X. Gao, M. Brameld, C.R. Hutchinson, On the corrosion and metastable pitting characteristics of 316L stainless steel produced by selective laser melting, J. Electrochem. Soc. 164 (6) (2017) 250e257.

[55] A. Röttger, J. Boes1 & W. Theisen-Microstructure and mechanical properties of 316L austenitic stainless steel processed by different SLM devices

[56] Niendorf A, Leuders S, Riemer A, Richard HA, Tröster T, Schwarze D (2013) Highly anisotropic steel processed by selective laser melting. Metall Mater Trans B 44B:794–796

[57] W. D. Callister and D. G. Rethwisch, Materials science and engineering, 9th ed., SI Version. ed. Hoboken, N.J: Wiley, 2015.

[58] Y. Smith. (2017, 25.01). Limitations of Optical Microscopy. Available: https://www.news-medical.net/life-sciences/Limitations-of-Optical-Microscopy.aspx

[59] Nano science Available at: https://www.nanoscience.com/techniques/scanning-electron-microscopy/#:~:text=by%20appropriate%20detectors. ,Sample%2DElectron%20Interaction,%2C%20and%20characteristic%20X%2Drays

[60] David Mainprice Scanning Electron Microscopy (SEM) & Electron Back Scattered Diffraction (EBSD) available at: http://crystal2plate.gm.univmontp2.fr/Crystal2Plate_Texture_course/SEM_EBSD_10

[61] Weilie Zhou, Robert P. Apkarian, Zhong Lin Wang, and David Joy10131Fundamentals of Scanning Electron Microscopy (SEM).pdf available at:

[62] S. Swapp. (2017, 26.01). Scanning Electron Microscopy (SEM). Available: https://serc.carleton.edu/research_education/geochemsheets/techniques/SEM.html

[63] ASTM E384-17 Standard Test Method for Microindentation Hardness of Materials, 2017.

ISO 6507-1:2018 Metallic materials — Vickers hardness test — Part 1: Test method

[64] Instron 5985 System Support, Available at: https://www.manualslib.com/manual/1899616/Instron-5980-Series.html?page=18#manual

[65] 5980 Series Dual Column Floor Frames Operator's guide - M10-16249-EN Revision E available at: https://www.instron.us/-/media/literature-library/manuals/5980-dual-column-floor-frames-operator-guide.pdf

[66] CSWIP, 2015.TWI. [Online]Available at: http://www.twi-global.com[Accessed 31 March 2020].

[67] D.D. Gu, Y.C. Hagedorn, W. Meiners, G. Meng, R.J. Santos Batista, K. Wissenbach, R. Poprawe, Acta Mater. 60 (2012) 3849–3860.

[68] F. Verhaeghe, T. Craeghs, J. Heulens, L. Pandelaers, Acta Mater. 57 (2009) 6006–6012.

[69] Maskery, I.; Aboulkhair, N.T.; Corfield, M.R.; Tuck, C.; Clare, A.T.; Leach, R.K.; Wildman, R.D.; Ashcroft, I.A.; Hague, R.J.M. Quantification and characterisation of porosity in selectively laser melted Al-Si10-Mg using X-ray computed tomography. Mater. Charact. 2016, 111, 193–204. [CrossRef]

[70] Kang, N.; Coddet, P.; Liu, Q.; Liao, H.; Coddet, C. In-situ TiB/near α Ti matrix composites manufactured by selective laser melting. Addit. Manuf. 2016, 11, 1–6. [CrossRef]

[71]] Y.F. Shen, D.D. Gu, P. Wu, Development of porous 316L stainless steel with controllable microcellular features using selective laser melting, Mater. Sci. Technol. 24 (12) (2008) 1501e1505.

[72] S.M. Yusuf, Y. Chen, R. Boardman, S. Yang, N. Gao, Investigation on porosity and microhardness of 316L stainless steel fabricated by selective laser melting, Metals 7 (2) (2017) 64, 1e12.

[73] A. Leicht, U. Klement, E.J.M.C. Hryha, Effect of build geometry on the microstructural development of 316L parts produced by additive manufacturing, Mater. Charact. 143 (2018) 137–143.